



K A U N O
TECHNOLOGIJOS
UNIVERSITETAS

ISSN 1822-5721

2006

MEDICAL PHYSICS in the BALTIC STATES

PROCEEDINGS OF THE 4th INTERNATIONAL
CONFERENCE ON *MEDICAL PHYSICS*

Kaunas, Lithuania
17-18 November, 2006

ISSN 1822-5721

KAUNAS UNIVERSITY OF TECHNOLOGY

MEDICAL PHYSICS IN THE BALTIC STATES

**Proceedings of the 4th International Conference on Medical
Physics**

**Kaunas, Lithuania
17 – 18 November, 2006**

Kaunas

Executive editor: **D.Adlienė**

CONFERENCE IS ORGANIZED BY:

Kaunas University of Technology
Malmö University Hospital, Lund University
Lithuanian Radiation Protection Centre
Kaunas Medical University Hospital

PROGRAM COMMITTEE

Diana ADLIENĖ - Kaunas University of Technology, *chairwoman*
Sören MATTSSON - Lund University, Malmö University Hospital, *chairman*
Ričardas ROTOMSKIS – Vilnius University
Albinas MASTAUSKAS – Lithuanian Radiation Protection Centre
Elona JUOZAITYTĖ – Medical University of Kaunas

ORGANIZING COMMITTEE

Lena ANCEVIČIENĖ – Kaunas University of Technology
Jurgita LAURIKAITIENĖ – Kaunas University of Technology
Gediminas ADLYS, Jr. – Kaunas University of Technology

CONFERENCE IS SUPPORTED BY:

Lithuanian State Science and Studies Foundation
Kaunas University of Technology
Malmö University Hospital
Lithuanian Radiation Protection Centre

Papers included in the Proceedings were referred by independent peer referees

© Kaunas University of Technology

PROGRAM

Friday, November 17, 2006

- 9.00-10.00** Registration of participants at **Kaunas University of Technology, Studentų St..50–325 F. Kaunas**
- 10.00–10.10** Opening (*D. Adlienė and S. Mattsson*)
- 10.10-10.25** *J. Venius, R. Rotomskis.* Analysis of different fluorescence excitation-emission systems for optical biopsy
- 10.25-10.40** *V. Žalgevičienė, J. M. Burkanas, J. Zukienė, J. Lapenė, A. Sukackaitė, G. Graželienė, J. Didžiapetrienė.* The influence of photosensitized treatment on development of rat embryo
- 10.40-10.55** *J. Lapenė, V. Žalgevičienė, E. Zakarevičius, E. Žurauskas, A. Sukackaitė, G. Graželienė, J. Didžiapetrienė, R. Rotomskis.* Spectroscopic evidence of placenta as a natural barrier for a photodrug
- 10.55-11.10** *J. Žerebcova, J. Valančiūnaitė, S. Bagdonas, G. Streckytė, R. Rotomskis.* Influence of pH and environment on photostability of second generation sensitizer TPPS₄ : spectroscopic study
- 11.10-11.35** *A. Weibull, H. Hall, K. Abul-Kasim, P. Maly, G. Lundborg and J. Svensson.* A pneumatically driven stimuli system for spatial mapping of primary somatosensory finger areas (Sweden)
- 11.35-12.00** *M. Warda, M. Nilsson.* Investigation of the Gafchromic film for use in radiotherapy quality assurance with the aid of the RisøScan software (Sweden)

Time for the lunch 12:00 – 13:00

- 12.15** **Opening ceremony of Radiation dosimetry laboratory** (Studentų St.50-251)
- 13.00-13.15** Welcome address to the conference, **prof. R.Bansevičius, Rector of Kaunas University of Technology**
- 13.15-14.00** *R. Rotomskis.* Nanoparticles in diagnostics and therapy: towards nanomedicine (invited speaker)
- 14.00-14.15** *J. Puišo, A. Šileikaitė, A. Guobienė, S. Tamulevičius, I. Prosyčevas, A. Juraitis.* Silver nanoparticles
- 14.15-15.00** *S. Mattsson.* New lines of development for radiation therapy of cancer (invited speaker) (Sweden)
- 15.00-15.15** *S. Måansson, A. Karlsson, H. Gustavsson, J. Christensson and S. Å. J. Bäck.* Dosimetric verification of breathing adapted radiotherapy using polymer gel (Sweden)

Coffee break 15.15-15.45

- 15.45-16.00** *S. Popov, G. Boka, A. Miller, Yu. Dekhtyar.* Implementation of portal dosimetry for patient related quality control in intensity modulated radiotherapy (Latvia)
- 16.00-16.15** *A. Miler, D. Norkus, I. Simutytė, R. Griškevičius, S. Popov.* Practical aspects of linear accelerator X-ray beam commissioning

- 16.15-16.30** *R. Plukienė.* Numerical modeling of ionizing radiation interaction processes in separate cell
- 16.30-16.45** *R. Purlys, Z. Norgėla, A. Poškus, R. Rinkūnas, A. Baltušnikas, V. Atkočius, B. Gricienė, A. Urbonienė, V. Leščiauskas, J. Žiliukas.* Relationship between intensity of continuous spectrum soft X-ray radiation and measured dose
- 16.45 -17.00** *S. Mockevičienė, D. Adlienė.* Patient's dose assessment in computed tomography.
- 17.00-17.15** *V. Minialga.* Application X-ray apparatus for biophysical investigations
- 17.15-17.30** *V.Zemite.* Time depended electron emission properties of bone (Latvia)
- 17.30-17.45** *R. Wiśniewski, T. Wilczynska.* Does high-pressure castor oil phase transition change its medical properties. (Poland)

19:00-22.00 Get - together party
“Perkūnas house”, Aleksoto St.. 6, Kaunas

Saturday, November 18, 2006

- 9.00-10.00** Registration at **Kaunas University of Technology, Studentų St.50-325 F.**
- 10.00-10.30** *S. Mattsson.* Safe use of ionising radiation in medicine. ICRP's current recommendations and ongoing work (Sweden and ICRP)
- 10.30-11.00** *K. Kepler, A. Vladimirov.* Optimisation of patient doses in digital radiology and the SENTINEL project (Estonia)
- 11.00-11.30** *J. Žiliukas.* Diagnostic reference levels and patient dose measurements in Lithuania
- 11.30-11.45** *Cibulskaite, R. Plaipaitė, E. Garnytė, E. Skripkaitė, S. Mockevičienė, D. Adlienė, V. Burinskienė, A. Andrijaitienė, G. Šetikienė, A. Urbonienė.*
Dose evaluation using *in vivo* TLD dosimetry in mammography

Coffee break 11.45-12.15

- 12.15-12.30** *Cibulskaite, J. Laurikaitienė, M. Šniurevičiūtė, E. Jonaitienė, B. Gricienė, G. Adly, R. Kabaila, S. Raila, S. Mattsson, D. Adlienė.* Towards optimization of the patient's doses in mammography in Lithuania
- 12.30-12.40** *V.Burinskienė, D. Adlienė.* Entrance surface dose measurements with thermoluminescence dosimeters and transmission ionization chamber
- 12.40-12.50** *J. Siaurys, G. Adly.* The use of digital methods in medical X-ray diagnostics
- 12.50-13.00** *L. Kryne* Image quality improvements using program package MatLab
- 13.00-13.10** *D. Šerėnaitė.* The ionization chamber's volume dependence on partial irradiation
- 13.10-13.30** Final remarks. Moderator *Sören Mattsson*

ANALYSIS OF DIFFERENT FLUORESCENCE EXCITATION-EMISSION SYSTEMS FOR OPTICAL BIOPSY

J. Venius, R. Rotomskis

Vilnius University Laser Research Center, Saulėtekio 9, c.3, LT-10222 Vilnius, Lithuania
e-mail: Jonas.Venius@ff.vu.lt, Ricardas.Rotomskis@ff.vu.lt

Abstract

Optical techniques nowadays are widely employed in many areas of biology and medicine; however, the detection of the signal from the particular layers of the tissue is still problematic. It was shown, that different geometry of the excitation-detection system enables to collect the fluorescence signal from the different depths of scattering media. The results indicate that the conventional bifurcated fiber (BF) system is exclusively sensitive to the fluorescence coming from the superficial layers, while both multidistance fiber (MF) and enhanced sensitivity MF (ESMF) systems appeared to be effective for detecting fluorescence signals from the deeper layers.

Key words: depth resolved fluorescence, excitation-emission system, optical biopsy

Introduction

Fluorescence spectroscopy nowadays is widely employed in many areas of biology and medicine. Due to non-invasiveness and instant approach of such methods they could be used in various diagnostic cases and are more convenient than conventional investigation methods, such as biopsy [1-3]. However measurements from deeper layers of the tissue are problematic due to light scattering and weakness of the signal.

In conventional optical biopsy the detected signal is a mixture of fluorescence signals originated in various

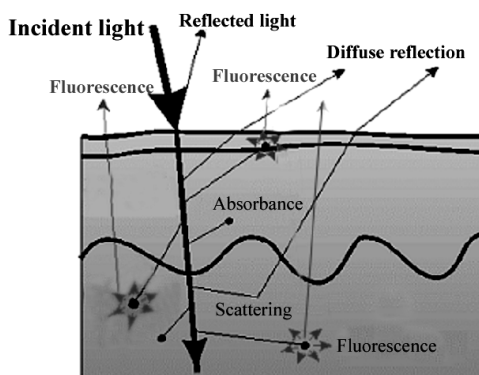


Fig. 1. Light paths in the tissue.

depths. Most of the signal is composed from the upper layer's fluorescence and sometimes it drowns the useful information coming from the tissue inside. The signal from the (turbid medium) deeper layers of the tissue is weak due to light scattering, but scattering also allows photons, originated deep in the tissue, leave the medium at high distances from the illumination source, whereas photons, originated in the superficial layers, will escape the medium at smaller distances (Fig.1) [4-6]. Therefore the design of fluorescence excitation-emission system is an important component of the optical biopsy. Depending on the geometry of the excitation-emission system it could be possible to detect photons selectively from various depths or to visualize the changes in the tissue, such as accumulation of the sensitizer or thickening/ diminution of the inner layers of the skin, which sometimes can indicate

the evolving of the tumour [4,6].

The aim of this research was to compare three excitation-emission geometries and to define the conditions were the use of each system would be the most expedient.

Materials and methods

The simplest system for optical biopsy consists of an *illumination source* (for fluorescence excitation), an *excitation-emission system* (to transmit excitation light to the tissue and to collect the emitted fluorescence) and a *detection unit* (usually a fluorimeter connected to a computer) for fluorescence spectra registration. The excitation source needs to be chosen in consideration of the investigated object. In our case it was a layered system simulated by means of a special multi-compartment cuvette (Fig. 2.). To simulate a biological object first two compartments were filled with scattering medium, 3rd and 4th – with fluorescing material (Quantum dots 1 (QD1), $\lambda_{em}=540\text{nm}$) and 5th – with QD2 ($\lambda_{em}=620\text{nm}$). In this way a layered turbid medium was constructed. Fluorescence of QD was excited by the light emitting diode ($470\pm10\text{ nm}$). Optical fibers were applied to realize the excitation-emission system.

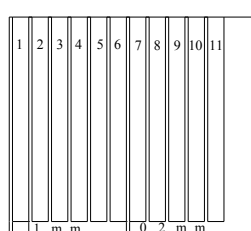


Fig. 2. A special cuvette for simulation of multilayered structures.

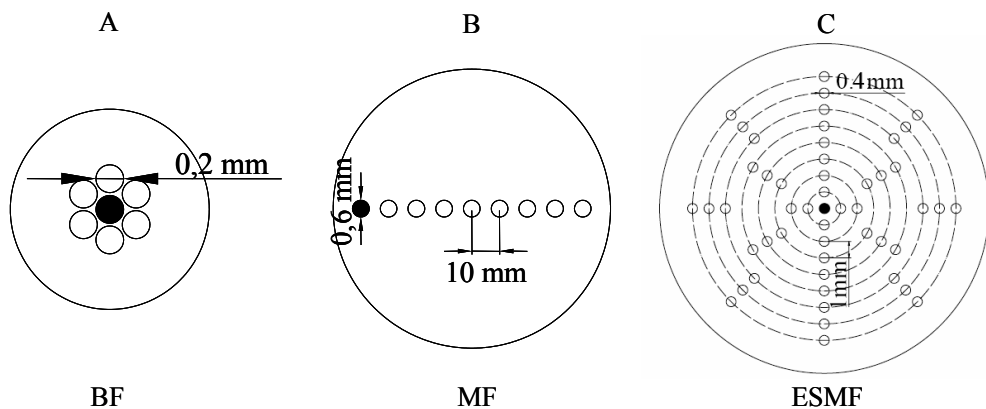


Fig. 3. Different geometries of excitation-emission system. A – Bifurcated fiber, B – multidistance fiber and C – enhanced sensitivity multidistance fiber.

Three different geometries of fluorescence excitation-emission system were investigated: a conventional bifurcated fiber (BF), a multidistance fiber (MF) and an enhanced sensitivity multidistance fiber (ESMF). All geometries are represented in Fig. 3. BF consists of one 200 μm thick fiber for excitation and six 200 μm fibers for the fluorescence collection. Emission fibers are situated around the excitation fiber at the same distance. The second – MF system consists of 8 collection fibers (600 μm thick) located at increasing distances (1 to 8 mm) from the single 600 μm thick excitation fiber. The last system – ESMF consists of a single 400 μm thick excitation fiber and 8 groups of collection fibers (each fiber is 400 μm thick) situated around at increasing distances from 1 to 8 mm. 1st and 2nd groups (distance from the excitation fiber – 1 mm and 2 mm) consist of 4 collection fibers. 3rd – 5th groups (distance 3–5 mm, respectively) consist of 6 fibers and 6th – 8th groups (distance 6–8 mm, respectively) consist of 8 fibers.

Because of scattering fluorescence photons emitted deep in the tissue will escape from the medium at higher distances from the illumination fiber, however intensities at higher radii are rather weak. Therefore, an increased number of collection fibers at higher distances should enhance sensitivity of the system to fluorescence originated in the deeper layers.

Fluorescence spectra were registered with a special four-channel spectrofluorimeter Avantes *AvaSpec-2048-3-RM*.

Results

The spatially resolved fluorescence was recorded to define three different excitation-emission systems. In reference to our previous results (results not shown), it was decided that for comparison between three different geometries it is sufficient to measure fluorescence intensities only at four different distances (1, 3, 6 and 8 mm from the excitation fiber) rather than at all eight radii.

Fluorescence spectra registered with BF, MF and ESMF systems are depicted in Fig. 4. Calculated coefficient S_1 reflects sensitivity of each system and represents the ratio of intensities registered with fibers closest to the excitation fiber at 540 nm and 620 nm. The bigger value represents higher sensitivity to the superficial layer in respect of the deeper layer. For the BF system $S_1 = 2.33$, for the MF $S_1 = 2.03$ and for the ESMF $S_1 = 1.89$. Consequently, BF system has the highest S_1 value thus being the most sensitive system for measurements of fluorescence from superficial layers.

MF and ESMF systems demonstrated higher sensitivity to deeper layers. When registering fluorescence at higher distances from the excitation fiber (MF and ESMF systems) the intensity of fluorescence from the deeper layer becomes higher, therefore, both systems are suitable for the depth-resolved fluorescence measurements.

The second coefficient S_2 was calculated to test ESMF sensitivity versus MF. S_2 represents the ratio of fluorescence intensities registered at 1 and 8 mm from the excitation fiber for 540 nm and for 620 nm. For the MF system: $S_2(\text{at } 540\text{nm}) = 148.8$, $S_2(\text{at } 620\text{nm}) = 26.1$ and for the ESMF system: $S_2(\text{at } 540\text{nm}) = 40.2$, $S_2(\text{at } 620\text{nm}) = 9.9$.

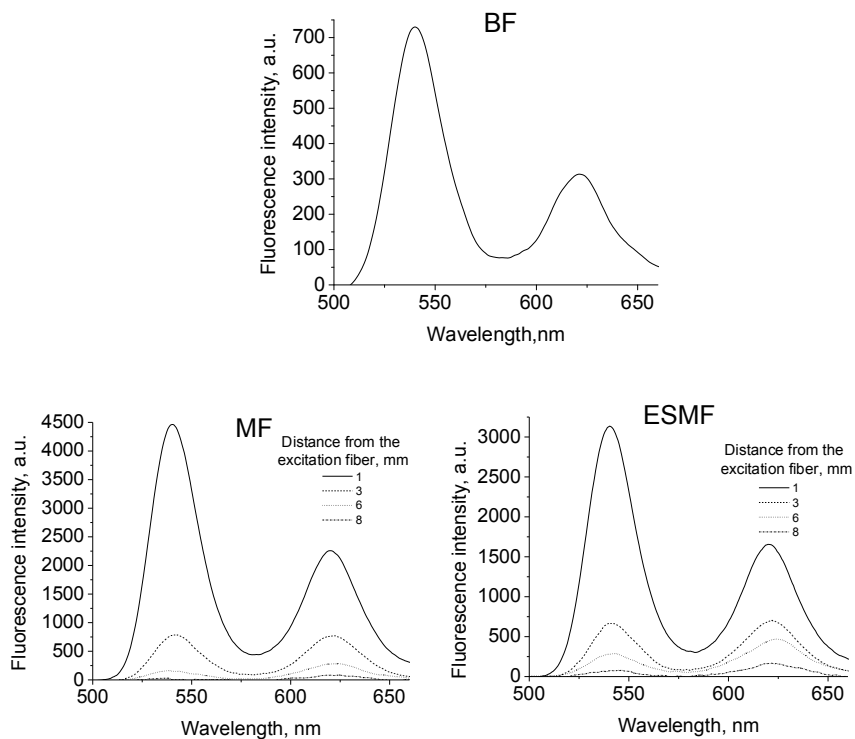


Fig. 4. Fluorescence spectra registered with BF, MF and ESMF systems.

The value of S_2 reflects a factor, by which the intensity decreases increasing the registration distance from 1 to 8 mm from the excitation fiber. Therefore, the fluorescence intensity measured with the ESMF system changed significantly less than in the case of the MF system. This indicates that the ESMF design enhanced general sensitivity of the system. This can be proved additionally by comparing fluorescence intensities of MF and ESMF systems registered at 8 mm distance. ESMF gave 2.6 and 2.0 times higher fluorescence intensities at 540 nm and 620 nm, respectively.

Conclusions

The obtained results indicate that compared systems could be used for different tasks. BF is most suitable for fluorescence measurements from superficial layers of the tissue. MF and ESMF systems are suitable for depth-resolved fluorescence measurements. However, ESMF showed significantly higher efficiency when detecting signals originated in the deeper layers, while MF is a simplified multidistance system and could be used for detection of highly fluorescing objects in the deeper layers of the tissue.

References

1. Wagnieres G.A. et al. In vivo fluorescence spectroscopy and imaging for oncological applications. – J. Photochem. Photobiol., 68, 1998, 630-632 p.
2. Rotomskis R, Streckytė G. Fluorescencinė navikų diagnostika. – Medicina, 40, N12, 2004, 1219-1230 p.
3. Venius J. et al. Optical visualization of the heart conduction system. – Acta Bio-Optica et Informatica Medica, 12, 2005, 6–9 p.
4. Zhu Ch. et al. Effect of fiber optic probe geometry on depth-resolved fluorescence measurements from epithelial tissues: a Monte Carlo simulation. – J. of Biomed. Opt. 8, N2, 2003, 237-247 p.
5. Brian W. et al. Fiber-optic bundle design for quantitative fluorescence measurement from tissue. Applied Optics. 1998, 37(31), p. 7429-7436.
6. Venius J. et al. Depth-resolved fluorescence measurements of quantum dots in scattering medium, 11th ESP 2005 - Aix-les-Bains, France, September 7, 2005.

SPECTROSCOPIC EVIDENCE OF PLACENTA AS A NATURAL BARRIER FOR A PHOTODRUG

J. Lapienis¹, V. Zalgeviciene², E. Zakarevicius¹, E. Zurauskas², A. Sukackaite¹, G. Grazeliene¹, J. Didziapetriene¹, R. Rotomskis¹

Institute of Oncology¹ and Faculty of Medicine², Vilnius University, Vilnius, Lithuania;
Santariskiu 1, Vilnius;
e-mail: lapienis@loc.lt

Abstract

Spectroscopic and fluorescence microscopy methods were used to evaluate Photofrin II accumulation in embryo and surrounding tissues (placenta, uterus, amniochorionic membrane) 24 hours after intravenous administration of the photosensitizer at 7th, 12th, 14th and 18th day of rat embryogenesis. It has been shown that embryo accumulates Photofrin II at a high rate in the first stages of embryogenesis. When placenta is being formed, accumulation of the photodrug in embryo is much lower. It has been shown that the main reason of that is the formed barrier in placenta and the most active part of barrier is chorion.

Keywords: *fluorescence spectroscopy, fluorescence microscopy, photosensitizer, photodrug, uterus, placenta, embryo.*

Introduction

A recently developed method for the treatment and diagnostics of various tumors – a photodynamic therapy (PDT) – has already been approved in some countries (USA, Canada, Japan, EU, etc.) for some cancers (bladder cancer, skin, head, neck cancers, etc.). This method consists of administration of light sensitive drug (photosensitizer) selective accumulation of it in tumor following the irradiation at a sensitizer certain wavelength light, what leads to the generation of singlet oxygen and targeted cell death [1,2]. Using this technology, however, today it is not possible to reach a complete selectivity because photosensitizers accumulate in healthy tissues as well [3,4]. This means that photodynamic reactions also occur in healthy tissues and may damage them. Therefore, a lot of experiments were made to determine the possible effect of PDT on healthy tissues and there are many results indicating that PDT is safe enough. For example, PDT might be very useful in treating pregnant women, while the other methods are too dangerous for them. Marco de Santis *et al.* showed that after the administration of photosensitizer Verteporphyrin into pregnant women (3rd week of embryogenesis), there were no side effects on newborns [5]. On the other hand, Yang JZ *et al.* showed that after the administration of 5-aminolevulinic acid into pregnant rats following the irradiation, resorptions were observed on newborns [6]. Grazeliene G. *et al.* showed that accumulation of photosensitizers in embryo depends on the stage of embryogenesis [7]. However, there is not enough information about the accumulation of photosensitizers in the organs of pregnant animal and more experiments in this field should be performed.

During the process of embryogenesis, placenta formation begins at the 6th day of embryogenesis and completes nearly at the 13th day of it. In the beginning, the embryo is surrounded by chorion. When the embryo is growing, the chorion changes and the direct contact with mother blood appears. During the formation of placenta, the most important subject is angiogenesis when inside the chorion's villi blood-vessels forms. Then the metabolism between mother and embryo becomes much more active. The formed placenta becomes a natural barrier, which starts preserving embryo from various exogenous harmful factors, ensures tolerance between mother and foetus, and supplies oxygen to the embryo [8]. This barrier also allows the passage of many chemical agents, which are harmful to the foetus and have selective negative effect on the cell proliferation and embryo development [9,10].

The aim of this study is to determine dyhenatoporphyrin ether (Photofrin II[®]) accumulation in pregnant rat uterus, placenta and embryo tissues and to estimate if natural placenta barrier could prevent embryo from the negative effect of PDT. It is expected to discover which part of a placenta works as a barrier for a photosensitizer, in which stage of embryogenesis PDT effects on embryo could be minimal, and to estimate the optimal stage for safe PDT.

Materials and methods

46 Wistar line white rats (160-240 g) were used in experimental studies. 110 embryos have been examined. The oestrous cycle of Wistar rats is about 4-5 days. During the cycle, female rats were kept together with male rats for a night. After 24 hours vaginas of the rats were examined. Oestrus stage phase was determined and presence of spermatozoa was checked. The day when the spermatozoa were found was assumed as zero day of the embryogenesis. Each group contained of 4 pregnant rats. The animals of control group were the same age

and weight as the experimental ones. All the animals were kept under the same conditions during all the experiment.

Photofrin II[®] (Axan Pharma Inc. - Canada) was used as a photosensitizer. It was intravenously administrated into experimental animals with a dose of 5 mg/kg at 7th, 12th, 14th and 18th day of embryogenesis. 24 hours after administration rats were killed and tissues were examined.

For spectroscopic measurements Perkin Elmer spectrophotometer was used. The tissues were frozen, cut into 1 mm slices, stored into Perkin Elmer spectrophotometer cuvete section and spectra were measured. The artifacts of intensity of fluorescence appeared because of shifting of samples, were removed by amount of measurements, averaging spectra and normalizing them to 550 nm.

For visualization haematoxylin-eosin and fluorescence microscopy methods (excitation maximum at 360 nm and observation filter passes 420-700 nm light) in histological preparations were used. Pregnant rats were killed and carefully dissected. Then the embryos were removed, the tissues were frozen, cut into 1 mm slices and stained with haematoxylin-eosin (methods are routinely used for histological studies). Colored photomicrographs were obtained from MOTIC B3-223 ASC microscope and photo camera CANON EL-2000. The digital photos were taken and analyzed in a computer.

The animal husbandry and experiments on animals were carried out according to the national and European regulations and were approved by the Lithuanian Animal Care and Use Committee.

Results and discussion

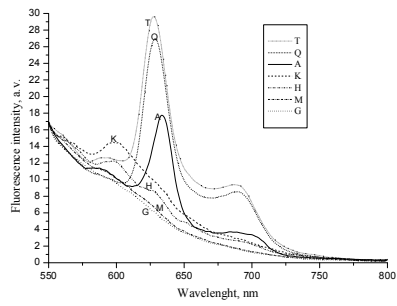


Fig. 1. The fluorescence spectra in rat organs 24 hours after administration of Photofrin II at the 7th day of embryogenesis: T – uterus incubated, Q – embryo incubated, A – liver control, K – muscle control, H – muscle incubated, M – uterus control, G – embryo control.

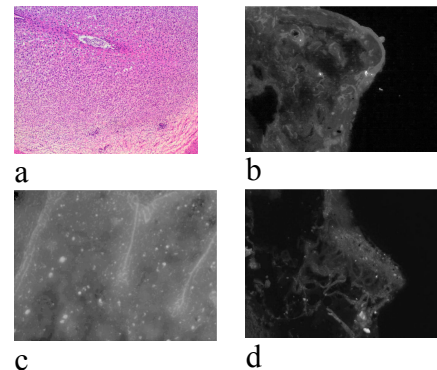


Fig. 2. a – embryo visualization at the 7th day of embryogenesis; b, c, d – fluorescence of embryo at the 7th day of embryogenesis

During the embryogenesis the rat placenta is being formed at 6th-13th day, thus the observation of accumulation of Photofrin II was started at the 7th day of embryogenesis. Fig. 1 shows the fluorescence of the photosensitizer in different tissues of sensitized rats (24 hours after the administration of a photodrug at 7th day of embryogenesis) and control ones. The peaks are at 630 and 705 nm that correspond Photofrin II fluorescence. It is obvious that photosensitizer accumulates in all the tissues. At the 7th day of embryogenesis placenta is not formed yet and the embryo is directly connected to mother's blood system. That is why the accumulation in embryo is as high as in uterus – even a little bit higher. That accords with previous article of our group [7]. Fig. 2 shows visualization of embryo and uterus using haematoxylin-eosin and fluorescence microscopy methods. As we can see there is no localized fluorescence in uterus or embryo and this tells that no barrier is formed at the 7th day of embryogenesis and supports spectroscopic measurements. The common fluorescence in uterus and embryo of Photofrin II could not be registered because of the much lower sensitivity of fluorescence microscopy method comparing with spectroscopic method. At the 12th-14th day of embryogenesis an embryo is already up to 1 cm. Placenta is completely formed as well – it is possible to distinguish amniochorionic membrane, chorion and other parts of placenta (Fig. 3).

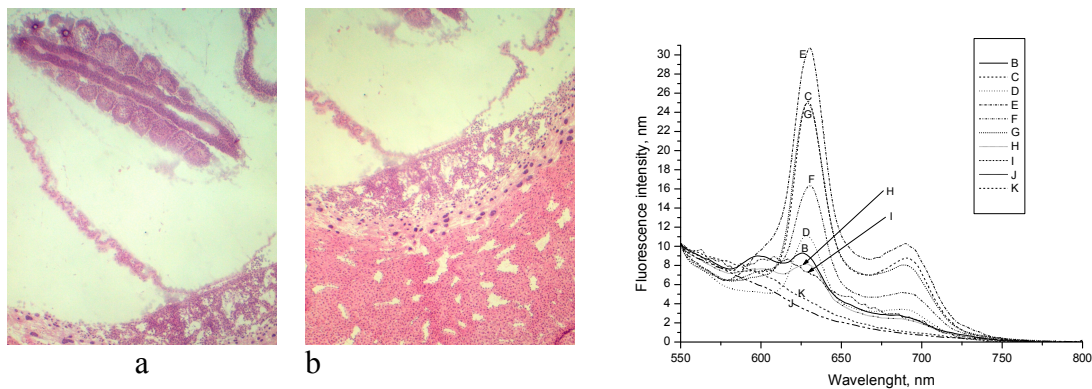


Fig. 3 (left). Embryo and chorion (a) and placenta (b) at the 12th day of embryogenesis
 Fig. 4 (right). The fluorescence spectra in rat organs 24 hours after administration of Photofrin II at the 14th day of embryogenesis: B – muscle incub., C - liver incub., D – uterus incub., E – placenta (embryo side) incub., F – placenta (mother side) incub. G – amniochorionic membrane incub., H – embryo incub., I – placenta (embryo side) control, J – amniochorionic membrane control, K – embryo control.

Spectroscopic measurements following 24 hours after administration of Photofrin II at the 14th day of embryogenesis (Fig. 4) show different fluorescence intensity of photosensitizer in embryo, uterus and embryo surrounding tissues (amniochorionic membrane, placenta at 14th day) comparing with the spectroscopic data from tissues at 7th embryogenesis day. It is obvious that at 14th day the accumulation of photosensitizer in embryo is much lower comparing with uterus, placenta and amniochorionic membrane. This means that some kind of barrier from outside factors is already formed and protects foetus from photosensitizer as well. On the 12th and 14th days of embryogenesis fluorescence microscopy (performed following 24 hours after the administration of Photofrin II) results (Fig. 5) shows that it is clear selective Photofrin II fluorescence only from the chorion that is believed to be a main barrier preserving foetus from outside factors. The villi of the chorion are surrounded with the syncitiotroblast. The stroma of the villi contains fetal fibroblasts and Haufbauer cells. The Haufbauer cells may be a type of macrophage. Haufbauer cells phagocytates exogenous antibodies, produces various cytokines and prostaglandins, takes place in ion transport, liquids regulation, and transmits the information from the main intracellular material to a nucleus [11]. They are in close contact with villus stroma collagen fibers, reticular cells and fibroblasts. It is believed that these cells are the most important for a barrier. We can conclude that chorion is a main barrier for a photosensitizer as well. Fluorescence microscopy data helps to explain why the fluorescence from the placenta foetus side is much higher than from the mother side (Fig. 4). This is because chorion is gripped to the foetus side of placenta at the area where spectroscopic measurements were performed. The same can be said to explain the extremely high fluorescence in the amniochorionic membrane (Fig 4).

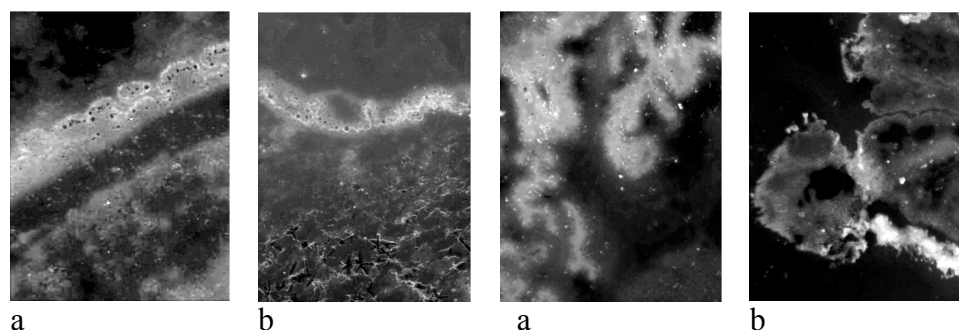


Fig. 5. Chorion fluorescence visualization at the 12th (a) and 14th (b) day of embryogenesis

Fig. 6. Chorion (a) and uterus (b) fluorescence visualization at the 18th day of embryogenesis

At the 18th day of embryogenesis, fluorescence microscopy (performed following 24 hours after administration of Photofrin II) results show the fluorescence in the part of amniochorionic membrane – chorion. This means that the barrier is still working (Fig 7a). On the other hand, during the fluorescence microscopy measurements it was noticed selective Photofrin II accumulation in uterus (Fig. 7 b). It may be because of the changes of uterus before the birth. However, it is necessary to perform more experiments in order to explain that.

Conclusions

Spectroscopic measurements show that Photofrin II accumulates in all the examined tissues. The accumulation of the photosensitizer in an embryo depends on the stage of embryogenesis. At the 7th day of embryogenesis the placenta is not formed yet and Photofrin II accumulates in the embryo and uterus almost similarly. At about 12th-14th day of embryogenesis placenta and the natural barrier are already formed. Spectroscopic method showed that the fluorescence of the photosensitizer in embryo is much lower than in placenta and uterus. This means that the barrier for a Photofrin II really exists and the fluorescence microscopy methods showed that amniochorionic membrane is responsible for that. The results from experiments performed at the 18th embryogenesis day confirmed the presence of barrier. Photosensitizer was observed selectively accumulated in a amniochorionic membrane again. On the other hand, the selective accumulation of the photosensitizer in a uterus was noticed. This might be explained by the changeover of uterus before the birth but it is necessary to perform more experiments to explain that.

The accumulation of the photosensitizer in an embryo may have negative effects but it is also possible that the natural barrier preserves it enough. However, further experiments are necessary in order to determine the total effect of PDT on the embryo.

References

1. Rotomskis R, Streckyte G, Grigiute L. Fotosensibilizuota navikų terapija: pirminiai vyksmai (monografija). (Photosensitized tumour therapy: primary processes.). Vilnius: Lietuvos mokslas; 2002.
2. Jori G. Photodynamic therapy: a novel approach to the treatment of tumors. Bull. Mol Biol Med 1990; 15:73-83.
3. Dennis EJGJ, Dolmans, Dai Fukumura and Rakesh K. Jain. Photodynamic therapy for cancer. Nature Reviews. Cancer 2003; 3(5):380-387.
4. Dougherty TJ, Gomer CJ, Henderson BW, Jori G, Kessel D, Korbelik M, et al. Photodynamic therapy. J Natl Cancer I 1998; 90(12):889-905.
5. De Santis M, Carducci B, De Santis L, Lucchese A, Straface G. First case of post-conception Verteporfin exposure: pregnancy and neonatal outcome. Acta Ophthalmol Scand 2004;
6. Yang JZ, Van Vugt DA, Melchior MF, Hahn PM, Reid RL. Photodynamic ablation of early pregnancy in the rat with 5-aminolevulinic acid: a potential new therapy for tubal ectopic pregnancy in the human. Fertil Steril 1994;62(5):1060-5.
7. Graželiénė G, Rotomskis R, Žalgevičienė V, Didžiapetrienė J, Žukienė J, Sukackaitė A, Legenis V. Accumulation of photosensitizer in rat embryos (a spectroscopic study). Medicina 2006; 42(2): 142-146.
8. Marin JJ, Briz O, Serrano MAA review on the molecular mechanisms involved in the placental barrier for drugs. Curr Drug Deliv 2004;1(3):275-89.
9. Miller R., Hendrickx A.G., Mills J.L., Hummler H., Wiegand U.W. Periconceptional vitamin A use: how much is teratogenic? Reproductive Toxicology 1998; 1(12):75 - 88.
10. James C. Cross. Placental function in development and disease. Reproduction, Fertility and Development 2005; 18(2):71–76.
11. Demir R, Erbengi T. Some new findings about Hofbauer cells in the chorionic villi of the human placenta. Acta Anat (Basel) 1984;119(1):18-26.

THE INFLUENCE OF PHOTOSENSITIZED TREATMENT ON DEVELOPMENT OF RAT EMBRYO

V. Zalgeviciene² M. Burkanaus¹, J. Zukiene² J. Lapienis¹, A. Sukackaite¹ G. Grazeliene¹,
J. Didziapetriene¹

Vilnius University, Institute of Oncology¹, Vilnius University, Faculty of Medicine, Vilnius, Lithuania²;
Ciurlionio 21, Vilnius;
e-mail: violeta.zalgeviciene@mf.vu.lt

Abstract

The aim of the experimental study was to evaluate the influence of the irradiation and the photodynamic therapy (PDT) on the rat embryo development. Photosensitizer Photofrin II administered to the *Wistar* rats intravenously on the 6th and 13th days of embryogenesis. The fluorescence measurements and application of irradiation and of PDT were performed 24 h. after injection of photosensitizer. For the examination of the embryos toxicity and teratogenicity, rats were sacrificed on the 21th day of embryogenesis. The results were allowed to make the conclusion that the amount of photosensitizer which was accumulate in the rats and embryo tissues had no hazardous effect on the embryo development on the treated days of embryogenesis.

Key words: *embryo, teratogenicity, skeleton, sensibilisation, photofrin II, photodynamic therapy*

Introduction

Photodynamic therapy (PDT) is a relatively new modality used for cancer treatment, consisting of the combined use of systemically administered photodrug and local applications of light emitted by lasers in the presence of oxygen. The photosensitizer can damage tumour cells and blood vessels in the tumour, thereby preventing the cancer from receiving necessary nutrients (1).

The results of some authors studies of the impact of photodynamic therapy (PDT) on the rat uterus endometrium after local intrauterine application of photosensitizer and laser light of 690 nm (a peak at high light penetration rate in tissues) showed that photosensitizer could penetrate deeper into uterus tissue. The same authors established that in the treated uterine horn (compared to the untreated horn) had an atrophy of the endometrial layer (2). *In vivo*, the photosensitizer mainly accumulates in the organs, which are rich of cells of mononuclear system (liver, spleen, kidney, and lungs), atherosclerotic plaques, areas of inflammation and healing wounds. The photo agent is absorbed by the cells all over the body, but it stays in well proliferative cells longer than it does in normal cells (3, 4).

Well proliferation of cells is par for the embryo, because embryogenesis of a multicellular organism is a result of the interaction of its component cells. The main cytophysiological processes in the formation of the foetus are changes in their size and form, as well as their morphological differentiation. Therefore, after experimentally blocking (completely or partially) of one of these cytophysiological processes in the foetus during embryogenesis, it becomes possible to identify the interaction of different external factors and their influence on embryo formation. In the embryogenesis there are critical periods in which the embryo is sensitive and mostly exposed to different negative effects. The harmful factors in those periods can induce the embryo mortality or different congenital anomalies. Classical critical periods of the foetus formation are as follows: implantation, placenta formation and organogenesis. The first critical period for the foetus is the implantation, the second one - the formation of placenta, i.e. 10th - 14th day of embryogenesis (5). The placenta is a highly permeable organ, natural barrier, for a large variety of substances with diverse molecular structures that are readily able to cross it from the maternal blood to reach the foetus (6).

The placental membrane (barrier) separates maternal blood from the foetal blood, regulates the transfer of nutrients and waste products through the placental membrane. This membrane acts as the filter, provides nutrients and oxygen from the maternal blood and allows diffusion of waste products. After 14th day of embryogenesis the mechanisms of regulation of homeostasis are more perfect but at the same time this barrier also allows the passage of many chemical agents, which could be harmful to the foetus and have selective negative effect to the cell proliferation and embryo development (7, 8).

In respect that, the purpose of the study was to evaluate if the amount of photosensitizer which was accumulate in the rats and embryo tissues had no hazardous effect on the embryo development on the treated days of embryogenesis and to identify possible malformations of the foetus of pregnant rats after PDT and irradiation without photosensitizer.

Materials and methods

The animal husbandry and experiments of animals were carried out according to the national and European regulations and were approved by the Lithuanian Animal Care and Use Committee.

In the experiment 20 Wistar line rats (160-240 g) and 94 embryos were used. In the proestrus stage the female rats were mated with male in the evening. The following morning the vaginal smears of females were examined microscopically. The day when the sperm in vagina was found was designated as day 0 of pregnancy. The intravenous injection of photofrin II (5 mg/kg) was taken on 6th (the period of implantation) and on 13th (the latest stage of placenta formation and active organogenesis) day of embryogenesis. The highest accumulation of photofrin II in the rat uterus and embryo tissues were 24 hours, so, the experiment was carried out on the 7th and 14th days of embryogenesis. The rats were sacrificed on the 21th day of embryogenesis.

Spectroscopic measurements in order to determine photosensitizer accumulation in rat tissues were performed 24 hours after administration of photofrin II, i.e. at 7th and 14th day of embryogenesis.

To determine photobleaching of the photosensitizer after irradiation and PDT, spectroscopic measurements in the irradiated part of uterus with foetuses inside and not irradiated part were performed. One of rats uterus horn (right horn) was taken as a control, the second one (the left) horn – experimental, i.e. 30 min. (200J) it was under the sway of irradiation or PDT.

Semiconductor light diodes (emission spectrum maximum at 633 nm) were used for irradiation. 6 diodes where focused to achieve a fluence rate of 120 mW/cm² and to overlap 1cm x 3cm area with the same fluence rate.

Using the same irradiation system, the second part of experiment for the determination of malformation were performed. The irradiation without photofrin and PDT was performed on the 7th and 14th days of embryogenesis and the pregnant rats were preserved until 21th day of pregnancy. For the examination of embryotoxicity and teratogenicity, rats were sacrificed on the 21th day of embryogenesis. After opening the uterus, live and dead pups were counted each of them was weighed and measured. For the skeletal defects examination, half of the embryos of a litter were examined macroscopically, half - for skeletal and the other defects. In order to render the skeleton visible, the soft tissues were macerated using NaOH, stained with alizarin red and cleared with glycerine. The Buen's solution was used for the macroscopical defects examination (5).

Results

High fluorescence of Photofrin II in the rat's uterus and embryo supporting tissues (i.e. chorion) indicates high penetration and accumulation of photosensitizer in pregnant rat organs (Fig 1). The fluorescence spectrum of uterine becomes distinct probably due to the fact that the mucous of uterine of pregnant rat thrives, its circulation of blood intensifies and much more photosensitizer gets into it. The amount of photofrin II in the embryo at 14th day of embryogenesis was signally less than in the uterus, placenta and chorion, while amount of the photosensitizer in the embryo at the 7th day of embryogenesis was close to the amount in uterus. This result shows that at the 7th day no barrier is formed yet. In order to determine if there could be any PDT effect photobleaching experiments were performed. The results showed (Fig 1. a, b) that after administration of photosensitizer at the 7th day of embryogenesis accumulated Photofrin II obviously bleaches after irradiation. Fluorescence intensity of the photodrug in embryo reduced more than three times. This tells that light penetration is high enough to reach embryo and make work PDT. It is obvious that some influence to the embryo was done. At the 14th day of embryogenesis photobleaching of the photosensitizer was observed as well. At this stage placenta and the placental barrier are already formed, the embryo is surrounded by more tissues (i.e. amniochorionic membrane). The bleaching in the embryo was hardly noticed while Photofrin II fluorescence intensity in placenta and uterus after irradiation reduced 2-10 times. This can be explained results from Fig. 1 (b) – much higher sensitizer fluorescence was observed in uterus, placenta and amniochorionic membrane than in embryo. We may conclude that the concentration of photosensitizer in embryo at the 14th day of embryogenesis is not high enough to make work PDT.

However, the results in the Fig 2 (a, b) shows, that PDT effects not only the embryo. Photobleaching was observed also in uterus and placenta both stages (i.e. at 7th and 14th) of embryogenesis. The following results show how PDT affected embryos.

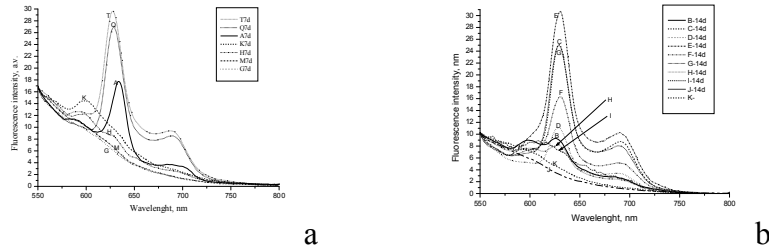


Fig. 1. Fluorescence spectra of rat organs 24 hours after administration of Photofrin II at 7th (a) and 14th (b) day of embryogenesis in comparison with control spectra (T7d - uterus incubated, Q7d - embryo incubated, A7d - liver control, K7 d - muscle control, H7d - muscle incubated, M7d - uterus control, G7d - embryos control; B14d - muscle incubated., C14d - liver incubated, D14 d - uterus incubated, E14d - placenta (embryo side) incubated, F14 d - placenta (mother side) incubated, D14d - amniochorionic membrane incubated, H14d - embryo incubated, I 14d - placenta (embryo side) control., J 14d - amniochorionic membrane control, K- embryos control).

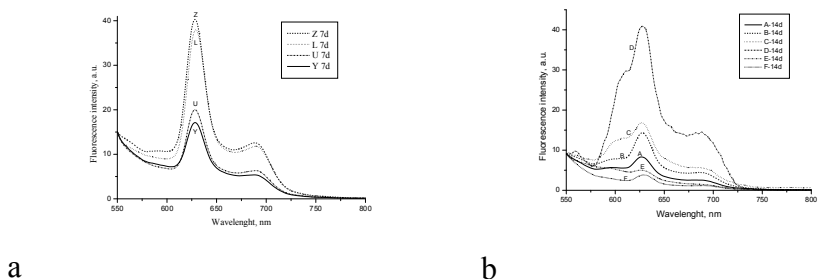


Fig. 2. Photobleaching of the Photofrin II fluorescence after irradiation (fluence rate 120 mW/cm² (634 nm), irradiation time 28 min.) 24 h after administration at 7th day of embryogenesis (a) and 14th day of embryogenesis (b); Z7d - uterus incubated, L 7d - embryo incubated, U7d - embryo incubation+irradiation, Y7d uterus incubatio+irradiation, A14d - uterus incubation+irradiation, B14d - uterus incubation, C14d - placenta incubation+irradiation, D14d - incubation, E14d -embryo incubation+irradiation, F14d embryo incubation

The embryo mass and length is the informative index to the embryotoxicity and teratogenicity. The harmful effect of different egzogeneous agents, are reflective of both sign, but changes in the embryo mass are more reflective on organogenesis and the length – on the skeletogenesis. The changes in the embryo length showed the toxicity as well as teratogenicity of the different egzogeneous agents, while the changes of ossification are more reflective to the teratogenicity: the origin of time of ossification centre, their length and deformation. It is possible to know the character of congenital anomalies.

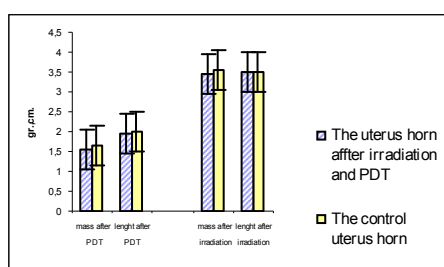


Fig.3. The 7th day of embryogenesis. The embryo mass and length after irradiation (without photofrin II) and PDT. Gestation day 21st

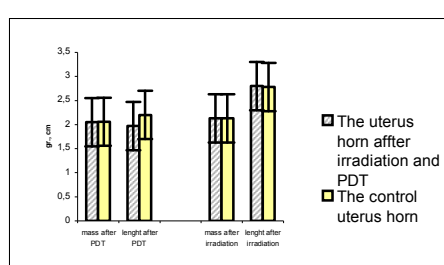


Fig.4. The 14th day of embryogenesis. The embryo mass and length after irradiation (without photofrin II) and PDT. Gestation day 21st

Our data showed that after influence of irradiation without photosensitizer and PDT on the embryo, in the both (left and right) uterine horn embryo stayed alive until 21th day of embryogenesis. Importantly was that were absent any harmful effect of the irradiation without photofrin II and PDT on the embryo all treated days. However, moderate alterations in the embryo mass and length was found: the less embryo mass in the both uterine horn was after PDT on the 7th day, while the length was considerably high after irradiation on the 14th day of embryogenesis. The embryo mass and length after laser light without photofrin II was slightly differ, than that after PDT (Fig. 3, 4, 5).

The purpose of different malformations origin is the blockade of embryogenesis after influence different derivatives (i.e. pharmaceutical ect). Irrefutable possibility that the PDT can raise harmful effect, therefore in second part of experiment a few series were aplyed: the first – PDT , the second – irradiation without photofrin II aplyed on the 7th and the 14th days of embryogenesis.

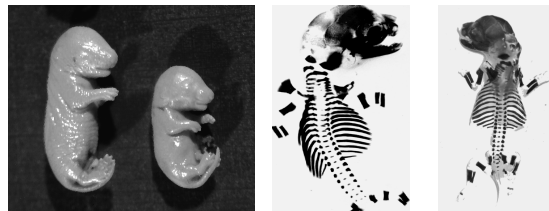


Fig. 5. The embryo after PDT (Gestation Day 20). Control embryo (on the left).

Fig. 6. The stained with alizarin red and cleared with glycerine embryo skeleton after PDT (Gestation Day 20). Control embryo on the left, on the right –embryo after PDT.

After an influence of PDT, the shortened or deformed ossification centre of the embryo skeleton was not established during all treated days. The embryo skeletons were clear observable all ossification centre were well formed and were parallel to the control embryo (Fig.6).

Conclusions

The accumulation of photofrin II in embryo tissues depends on the stage of embryogenesis. Spectroscopic measurements results show that PDT affects embryo and its surrounding tissues. However due to the surrounding tissues and placental barrier the penetration of the photosensitizer to the embryo is reduced and the concentration of the photofrin II in the embryo is too low for a PDT effects to be harmful.

Reference

1. Furuse K, Fukuoka M, Kato, et al. A prospective phase II study on photodynamic therapy with photofrin II for centrally located early-stage lung cancer. The Japan Lung Cancer Photodynamic Therapy Study Group. J Clin Oncol. 1993; 11(10):1844-5.
2. Steiner RA, Tadir Y, Tromberg B, Wyss P, Walt H, Haller U, [Benzoporphyrin derivative mono acid for photodynamic therapy of the endometrium] Geburtshilfe Frauenheilkd. 1996 Jan; 56(1):1-7.
3. Dolmans DEJGJ, Fukumura D, Jain RK. Photodynamic therapy for cancer. Nature Reviews. Cancer 2003;3 (5):380–387.
4. Dennis E.J.G.J., Dolmans, Dai Fukumura and Rakesh K. Jain. Photodynamic therapy for cancer. Nature. 2003. Vol.3; 380-387.
5. Wallace Hayes A. Principles and Methods of Toxicology. New York: Raven Press, 1994, p. 1006–1036.
6. Marin JJ, Briz O, Serrano MAA review on the molecular mechanisms involved in the placental barrier for drugs. Curr Drug Deliv. 2004; 1(3): 275-89.
7. Miller R.K., Hendrickx A.G., Mills J.L., Hummller H., Wiegand U.W. Periconceptional vitamin A use: how much is teratogenic? // Reproductive Toxicology. - 1998. - Vol 12, No 1. - P. 75 - 88.
8. James C. Cross. Placental function in development and disease. Reproduction, Fertility and Development . 2005.- 18(2) 71–76.

INFLUENCE OF pH AND ENVIRONMENT ON PHOTOSTABILITY OF SECOND GENERATION SENSITIZER TPPS₄: SPECTROSCOPIC STUDY

J. Žerebcova, J. Valančiūnaitė, S. Bagdonas,,G. Streckytė and R. Rotomskis

Vilnius University Laser Research Center, Saulėtekio 9, c.3, LT-10222 Vilnius, Lithuania

e-mail: Jelena.Zerebcova@ff.vu.lt, Jurga.Valanciunaite@ff.vu.lt

Abstract

TPPS₄ is a well-known 2-nd generation sensitizer used in the photosensitized tumour therapy. Inside the cells the sensitizer could exist in protonated form. In these studies, we investigated how variation in medium acidity and microenvironment affects TPPS₄ photostability. Absorption spectroscopy methods were applied. It was found that TPPS₄ is more photostable in acidic than in neutral solution. The same effect was observed in model media; however, the photobleaching of TPPS₄ absorbance was generally enhanced as compared to pure solutions. The decrease of oxygen concentration during irradiation revealed that photodestruction was caused by type II photochemical reactions.

Key words: absorption spectroscopy, sensitizer, photobleaching, albumin, singlet oxygen.

Introduction

The efficiency of the photosensitized therapy depends on the photophysical properties of sensitizers. The important photophysical property is intense absorbance in the red spectral region. Optical properties of TPPS₄ in different medium highly depend on pH. In the neutral and basic medium TPPS₄ exist in a nonprotonated form. The absorption spectrum of this form is typical of the etio-type spectra: the Soret band at around 413 nm and four Q bands of decreasing intensity in the visible spectral region: at around 515 nm (Q IV), 550 nm (Q III), 580 nm (Q II) and 635 nm (Q I). The ionic equilibrium constant (pK_a) of TPPS₄ is 4.8-4.9 and in more acidic medium the protonated form becomes dominant. The absorption spectrum of the protonated form consists of the red-shifted Soret band at around 433 nm and two relatively intense bands at 592 nm and 645 nm. It is shown that TPPS₄ localize in lysosomes[1] where pH is around 4 and, therefore, inside the cells the sensitizer might exist in a protonated form (TPPS₄²⁺), which has more suitable spectral properties for PTT.

Most of the sensitizers used in the PTT are degraded on light illumination. Photodegradation of the sensitizer results in a decrease in its initial concentration and, as a consequence, a lower sensitizing effect. Photostability of the sensitizer could be affected by changes in its ionic form, therefore, it is important to understand how variation in medium acidity and microenvironment affects TPPS₄ photostability.

Materials and methods

TPPS₄ was obtained from Porphyrin Products (Logan, Utah, USA) and bovine serum albumin (BSA) from Fluka (USA). Photobleaching and oxygen consumption of TPPS₄ were studied in phosphate buffered solutions (PBS) (pH 5–7), in the presence of bovine serum albumin (BSA) and in pure aqueous solutions. A singlet oxygen quencher sodium azide (NaN₃) was used for comparative purposes.

For irradiation diode lasers with emission maxima at 652 nm and 635 nm were used. Fluence rate was 10–100 mW/cm². Samples (V=2 ml) were irradiated in quartz and plastic cuvettes (a path length – 1 cm), and simultaneously oxygen concentration was measured. Absorption spectra were recorded with the fibre optics built-in spectrometers PC1000, PC2000 (Ocean Optics Inc., USA) and a scanning spectrometer UV-3101PC (Shimadzu, Japan). Bleaching rate constants were evaluated by following formula:

$$K = \frac{1}{D} \frac{1}{A_{\lambda_{irr}}} \frac{\Delta A_{\lambda_{bl}}}{A_{\lambda_{bl}}} \quad (1)$$

where D=It is the delivered irradiation doze (I, fluence, t, irradiation time), $\Delta A_{\lambda_{bl}}$ is the absorption bleaching at the wavelength of measurement λ_{bl} estimated from the absorption difference spectrum after irradiation, $A_{\lambda_{bl}}$ and $A_{\lambda_{irr}}$ are the initial absorbance values at λ_{bl} and λ_{irr} , respectively.

For oxygen consumption measurements, Fibre Optics Oxygen Sensor (FOXY) System obtained from Optics Ocean Inc. (USA) was used. FOXY system consists of S2000-FL

spectrometer, oxygen probe FOXY-R with a 600 micron bifurcated fibre QBIF600-VIS/NIR-BX and a blue LED excitation source LS-450 ($\lambda_{\text{em}}=492$ nm).

Results and Discussion

In neutral media (pH=7.0, PBS) TPPS₄ is relatively photostable [2]. Exposure of the solutions to 360 J/cm² dose induced about 7% decrease of the absorbance (Fig.1a, b). The bleaching rate constant (calculated at the QIV band) was $K_{\text{TPPS}4}(\text{pH}=7.0)=1.55 \times 10^{-3} \text{ J}^{-1}\text{cm}^2$. At slightly acid media (pH=5.9; PBS) the sensitizer is more photostable: exposure of the solutions to 360 J/cm² dose induced only about 1% decrease of the initial absorption (data not shown) and the bleaching rate constant was $K_{\text{TPPS}4}(\text{pH}=5.9)=0.65 \times 10^{-3} \text{ J}^{-1}\text{cm}^2$.

The tendency is retained in more acid media. The bleaching rate constant of the TPPS₄ protonated form was $K_{\text{TPPS}4}(\text{pH}=4.0)=0.22 \times 10^{-3} \text{ J}^{-1}\text{cm}^2$. This implies that the ionic species TPPS₄²⁺ is more photostable during PTT (Fig.1.c,d).

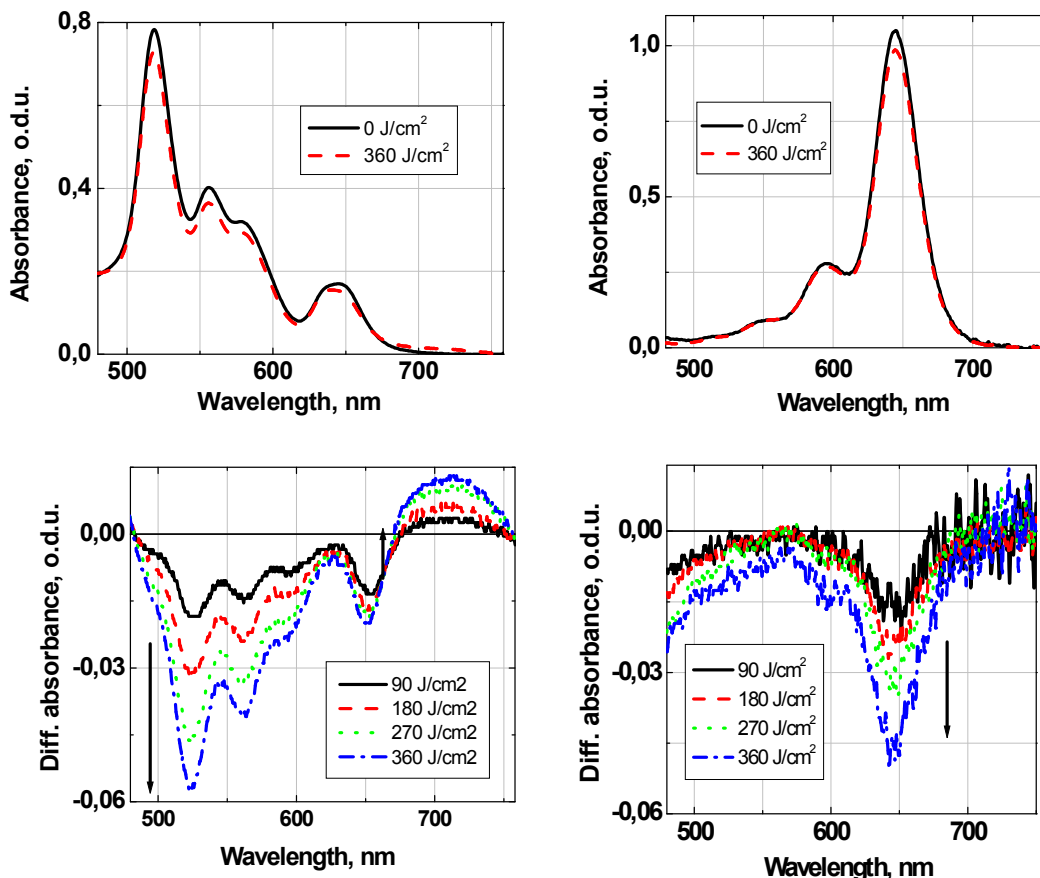


Fig. 1. Absorption and absorption difference spectra of TPPS₄ during irradiation: a, b – nonprotonated form (pH=7; $c=7.5 \times 10^{-5}$ M) c, d – protonated form (pH=4; $c=3 \times 10^{-3}$ M)

The photostability can change because of interaction of the sensitizer with tissue molecules. We have chosen bovine serum albumin (BSA) as a model of biological system. Under irradiation of TPPS₄ in PBS solutions in the presence of BSA (at molar ratio 1:0.2) more intensive degradation of the sensitizer was observed (data not shown). The bleaching rate constants were $K_{\text{TPPS}4/\text{BSA}}(\text{pH}=7.0)=2.97 \times 10^{-3} \text{ J}^{-1}\text{cm}^2$, $K_{\text{TPPS}4/\text{BSA}}(\text{pH}=5.8)=1.38 \times 10^{-3} \text{ J}^{-1}\text{cm}^2$.

A noteworthy fact is that the tendency of increase in photostability in more acid solutions is sustained in the model media. Enhancement of TPPS₄ photobleaching in the presence of BSA could occur due to the formation of active oxidative albumin species, which could further react with the sensitizer.

Photobleaching of TPPS₄ also leads to the formation of photoproducts as indicated by appearance of spectral changes in red and UV regions [3]. In neutral media (pH=7.0) (Fig. 1. b) and in the presence of BSA (pH=5.8-7.0) (data not shown) photobleaching of initial TPPS₄ absorbance is accompanied by formation of a broad band in the red region.

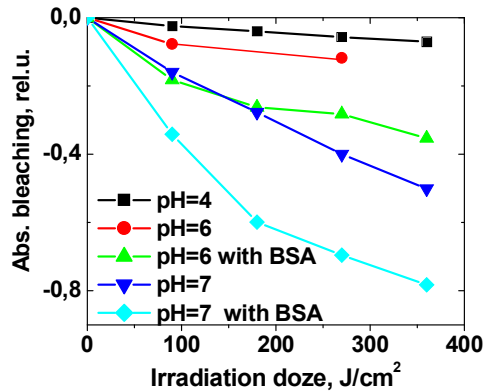


Fig. 2. Kinetics of absorption bleaching of TPPS_4

Photodegradation of the sensitizer results in depletion of oxygen. During irradiation low oxygen consumption up to 10% was observed for pure TPPS_4 solution ($c = 10^{-4}\text{M}$, PBS, pH=7.2) (Fig. 3).

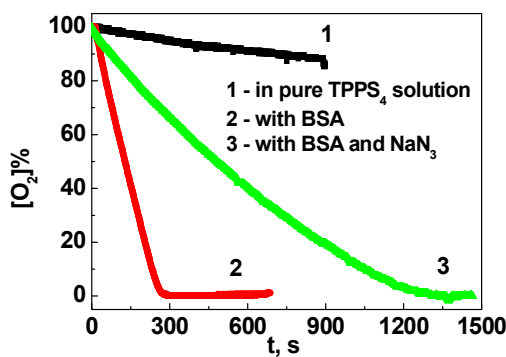


Fig. 3. Oxygen consumption during irradiation of TPPS_4

However, when the solution was irradiated in the presence of BSA (at molar ratio 1:1), oxygen concentration decreased almost to zero. Addition of singlet oxygen quencher - sodium azide (at molar ratio 1:1:100) significantly slowed oxygen consumption rate. Oxygen consumption in the presence of NaN_3 supports the involvement of singlet oxygen in TPPS_4 induced photochemistry. It shows that photodestruction of TPPS_4 is induced by the type II photosensitization reactions.

Conclusions

TPPS_4 is more photostable in pure solutions; presence of BSA induces faster photobleaching of TPPS_4 .

The photostability of TPPS_4 in aqueous solutions and in model media containing protein substrate (BSA) is increased at lower pH values. Rate constants of initial absorbance photobleaching:

$$K_{\text{TPPS}_4}(\text{pH}=7.0)=1.55 \cdot 10^{-3} \text{ J}^{-1}\text{cm}^2, K_{\text{TPPS}_4/\text{BSA}}(\text{pH}=7.0)=2.97 \cdot 10^{-3} \text{ J}^{-1}\text{cm}^2, K_{\text{TPPS}_4}(\text{pH}=5.9)=0.65 \cdot 10^{-3} \text{ J}^{-1}\text{cm}^2, \\ K_{\text{TPPS}_4/\text{BSA}}(\text{pH}=5.8)=1.38 \cdot 10^{-3} \text{ J}^{-1}\text{cm}^2, K_{\text{TPPS}_4}(\text{pH}=4.0)=0.22 \cdot 10^{-3} \text{ J}^{-1}\text{cm}^2.$$

Addition of NaN_3 suppressed photoinduced oxygen consumption of neutral TPPS_4 form in the presence of BSA implying that TPPS_4 induce type II photosensitization reactions.

References

1. Berg K., Western J. C., Boomer J.C., Moan J. Intracellular localization of sulphonated meso-tetraphenylporphines in a human carcinoma cell line. - Photochem. Photobiol., 52, N3, 1990, 481 - 487 p.
2. Rotomskis R., Streckytė G., Bagdonas S. Phototransformations of sensitizers 1. Significance of the nature of the sensitizer in the photobleaching process and photoproduct formation in aqueous solution. - J. Photochem. Photobiol. B: Biol., 39, 1997, 167 - 171 p.
3. Rotomskis R., Bagdonas S., Streckytė G. (1996) Spectroscopic studies of photobleaching and photoproduct formation of porphyrins used in tumor therapy. -J. Photochem. Photobiol. B: Biol., 33, 1996, 61 - 67 p.

A PNEUMATICALLY DRIVEN STIMULI SYSTEM FOR SPATIAL MAPPING OF PRIMARY SOMATOSENSORY FINGER AREAS

A. Weibull¹, H. Hall², K. Abul-Kasim³, P. Maly³, G. Lundborg⁴, J. Svensson¹

¹Department of Medical Radiation Physics, ²Department of Biomedical Engineering, ³Department of Diagnostic Radiology, ⁴Hand Surgery Research Group.

Malmö University Hospital, 205 02 Malmö, Sweden E-mail: andreas.weibull@med.lu.se

Abstract

To be able to spatially resolve and map the finger areas in the primary somatosensory cortex using fMRI, it is important to apply an exact and reproducible stimulus. The purpose of this work was to construct a pneumatically driven, computer controlled, system for tactile stimuli of targeted skin areas, and to test it in fMRI for cortical mapping.

The presented system was able to deliver a stimulus resulting in distinct and precise fingertip activation in the primary somatosensory cortex. The ability of this system to separate fingers in the cortex makes it very promising for studies of brain plasticity in hand and finger disorders and injuries.

Keywords: fMRI, somatosensory cortex, tactile stimuli

Introduction

Spatial mapping of finger areas in the primary somatosensory cortex is interesting for several different applications (e.g. studies of functional changes in the brain after hand surgery, and studies of neurological pathologies like focal hand dystonia, could benefit from a reliable mapping method). To be able to spatially resolve and map the finger areas in the primary somatosensory cortex using fMRI, it is important to use a system able to apply an exact and reproducible stimulus.

The purpose of this work was to construct a pneumatically driven, and computer controlled system for tactile stimuli of targeted skin areas, and to test it in fMRI for cortical mapping, and separation of somatosensory finger areas.

Subjects and Methods

Stimuli system. The stimuli system is pneumatically driven and electronically controlled (Fig 1) similar to Wienbruch et al (1), but with a different control design. It has eight separate channels that can be individually controlled. Each channel consists of a pneumatic valve (Festo, 525146, Fig 2a) connected with a plastic tube to a membrane (4-D Neuroimaging, area ca. 0.8 cm², Fig 2b). The membrane can be attached to the target skin area using tape, and when the valve is alternately opened and closed the membrane delivers a tactile stimulus. The system is driven by compressed air with a few bars overpressure. In the current set-up the permanently installed air supply in the scanner room is used, but an external air bottle could also be used.

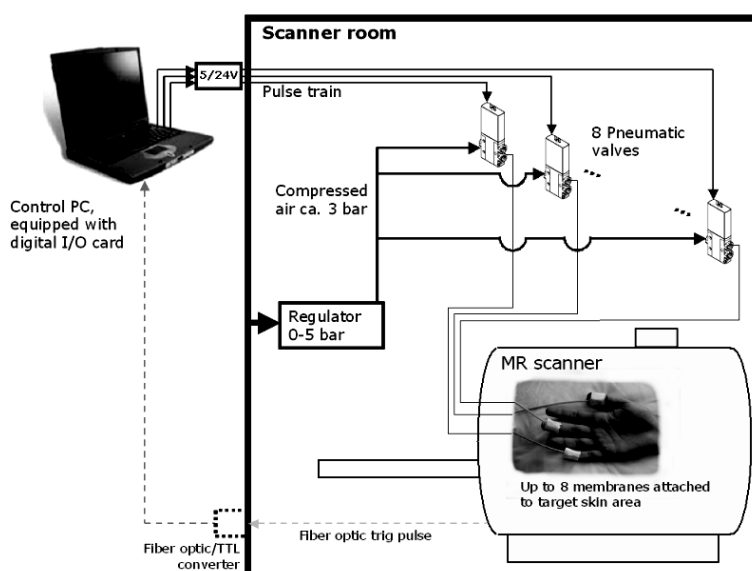


Fig 1. Schematic view of the stimuli system set-up

The pneumatic valves are electronically controlled using an ordinary laptop PC equipped with a 24 channel digital I/O PCMCIA card (National instruments, 776912-01), and a custom written LabVIEW software (Fig. 2c). The software allows individual setting of the desired pulse timings and frequencies for each separate channel. The pulse signals are amplified from 5 to 24 V using an in-house built power amplifier.

All pneumatic equipment is placed inside the scanner room whereas the electronic control equipment is placed outside, in the control room. The system is prepared for accepting a trig pulse from the scanner for exact synchronization of scanning and stimuli. This was however not utilized in this preliminary set-up.

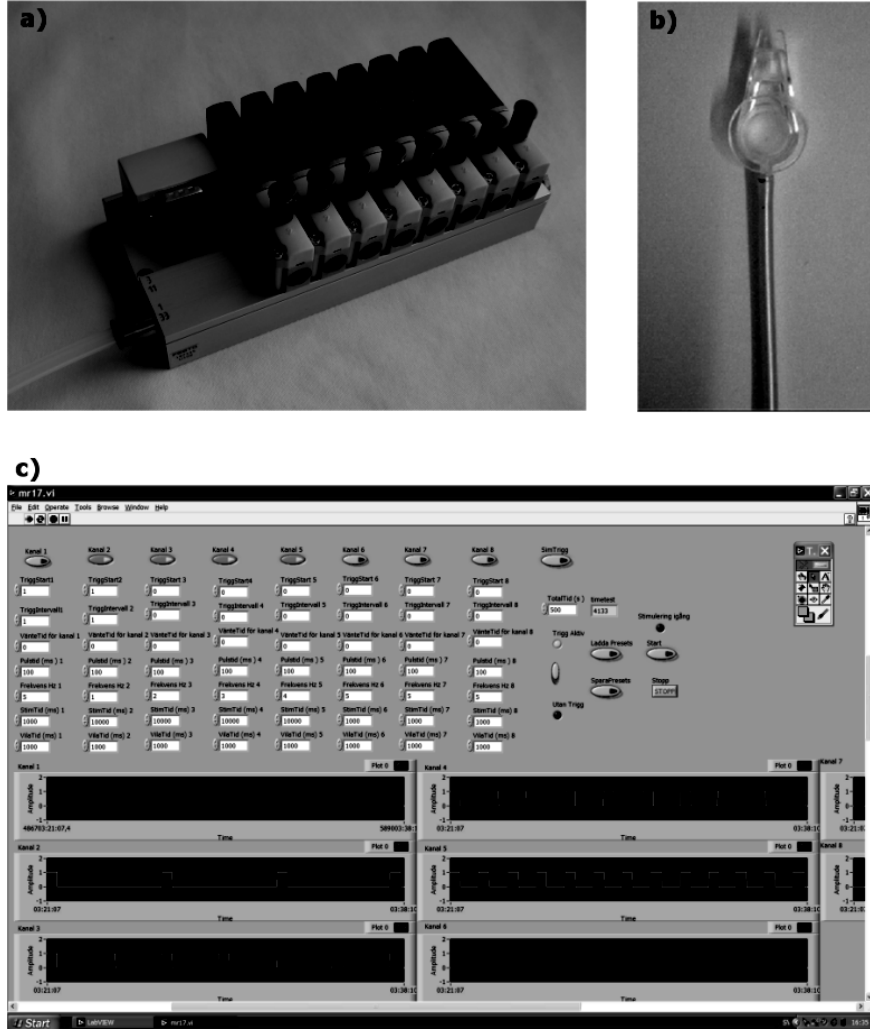


Fig 2. a) The 8 pneumatic valves mounted in valve terminal, b) Plastic membrane used for tactile stimuli and c) LabView interface on PC

FMRI experiment. To test the stimuli system, fMRI was performed on 11 healthy subjects using a Siemens Trio 3 T scanner equipped with an 8-channel head coil. Three membranes were attached to the tips of the thumb, middle, and little finger respectively. Tactile stimuli of the three fingers (pulse frequency = 1 Hz, pulse width = 100 ms, 3 bars pressure) were separately applied in a randomised block design alternating between rest conditions (block length = 30 seconds). Before functional imaging a high-resolution anatomical scan was acquired (FLASH, TE/TR = 4.9/11 ms, Flip angle = 15°, Resolution = 1x1x1 mm³, 176 slices). Functional BOLD imaging was performed using a GR-EPI pulse sequence with TE/TR = 30/2660 ms (288 time points). During each session two BOLD data sets with different spatial resolution were acquired (2x2x2 mm³, and 3x3x3 mm³).

Evaluation. Evaluation of the data was performed using Brainvoyager QX software. Following motion correction, and preprocessing, separate activation maps for the three different fingers were created and corrected for false discovery rate (FDR). The data were evaluated for single subjects as well as on a group level.

Results

In single subject evaluation with a significance threshold of $q(FDR) < 0.05$, contralateral activation of the primary somatosensory cortex was observed for the thumb, middle finger, and the little finger in 50%, 55%, and 27% of the cases respectively. A subject with activation in all three fingers is shown in Fig. 3.

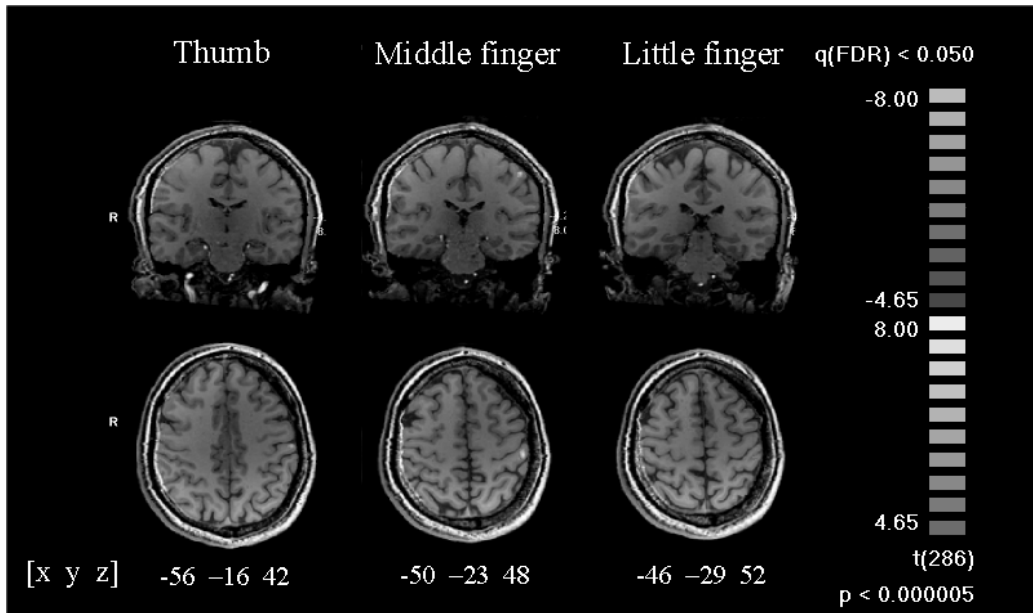


Fig 3. Single subject activation in primary somatosensory cortex from stimuli of three different fingertips.
No spatial smoothing was applied. Clusters do not overlap. Coordinates are given in Talairach space.

Group analysis of the 3^3 mm^3 data, yielded activation at $q(FDR) < 0.05$ for the thumb and middle finger only (Fig. 4). At 2^3 mm^3 however, all three fingers showed activation. The group analysis activation clusters appeared large and somewhat overlapping at this level. In this type of study it is often of more interest to obtain a precise localization of the respective activation foci rather than the cluster centre of gravity. To achieve this, the statistical threshold was restricted further until cluster sizes were no larger than 100 voxels, and hence only the most significant activation coordinates were visualized (Fig. 5).

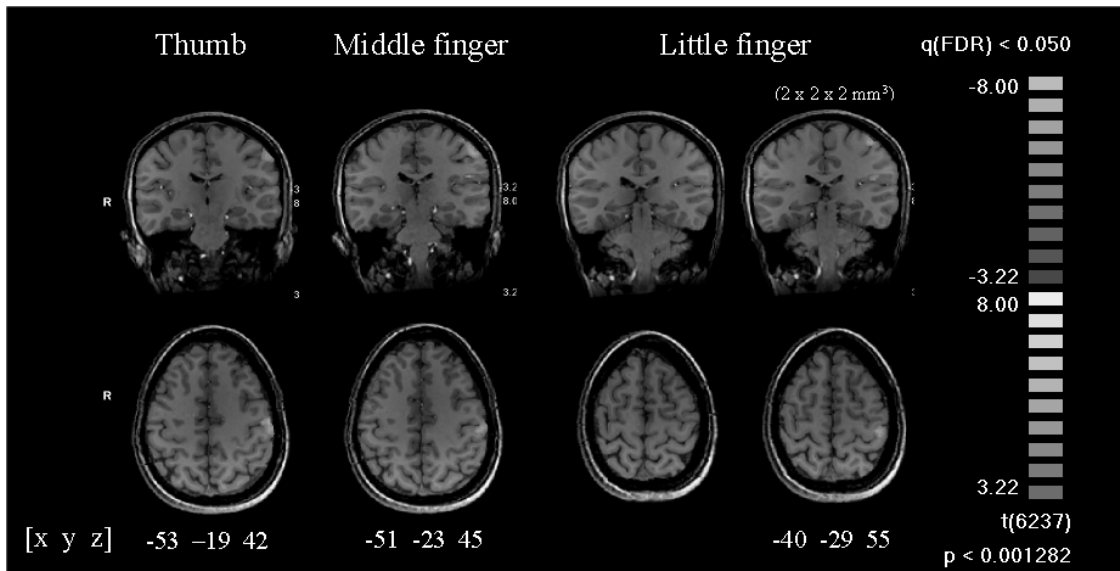


Fig 4. Group activation for the three fingers in 3^3 mm^3 resolution. The little finger is also presented at 2^3 mm^3 .
Coordinates are given in Talairach space.

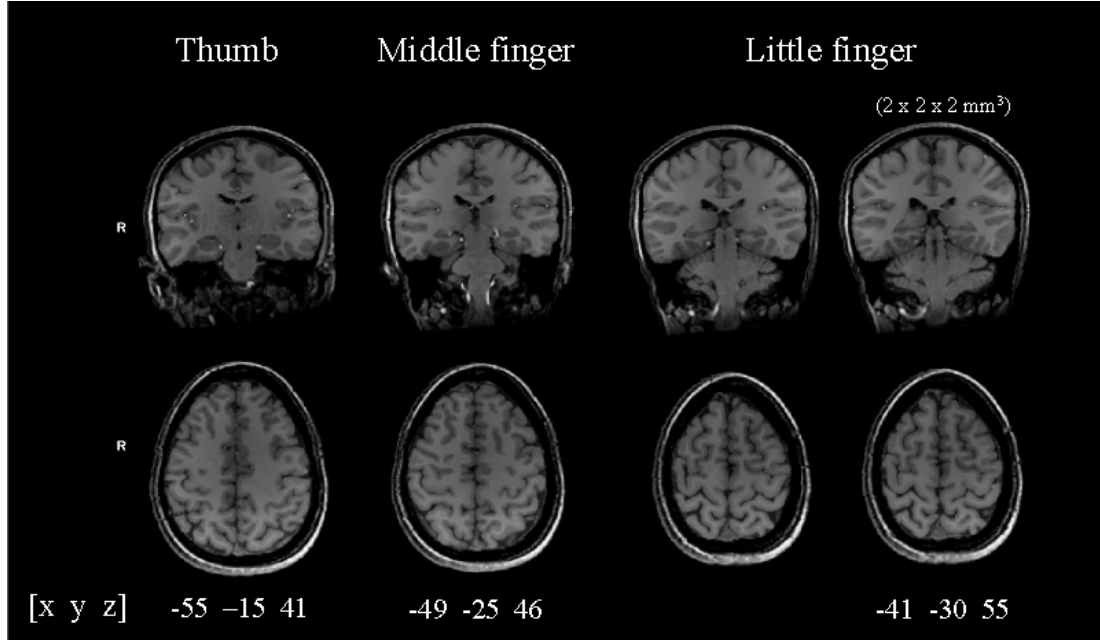


Fig 5. Same results as in fig 4, but at a more strict threshold (cluster sizes < 100 voxels) to visualize activation foci.

Overall, the activation cluster localization for the separate fingers corresponded well to the expected organization in primary somatosensory cortex. I.e. the thumb, middle finger, and little finger were organized in an anterior-to-posterior, inferior-to-superior and, lateral-to-medial manner. No ipsilateral activation was observed in any of the cases, neither for single subjects nor in the group analysis.

Discussion/Conclusion

The electronic control of the system assures a reproducible tactile stimulus delivery. Another advantage is that the membranes can be attached to the fingertips without constraining the subject's hand position, thus reducing the risk for problems of fatigue during the experiment.

In summary, the presented system proved able to deliver a stimulus resulting in distinct fingertip activation in the primary somatosensory cortex. This system seems promising for studies aiming to separate cortical finger areas such as studies of brain plasticity in hand and finger disorders and injuries.

References

1. Wienbruch et al, Neuroscience letters 398, 2006, 183-188 p.

INVESTIGATION OF THE GAFCHROMIC® FILM FOR USE IN RADIOTHERAPY QUALITY ASSURANCE WITH THE AID OF THE RISØSCAN SOFTWARE

Mats Nilsson and Maisa Warda

Dept of Radiation Physics, Malmö University Hospital, SE-205 02 Malmö, Sweden
e-mail: Mats.Nilsson@med.lu.se, Maisa.Warda@skane.se

Abstract

Self-developing film has been investigated with respect to basic properties such as response to absorbed dose and to time, spatial and dose resolution and noise power spectra. Also, key properties of a commercial flat bed scanner that can influence the accuracy and precision of the film as a dosimeter have been studied. The film has been tested as an alternative tool for mapping dose distributions in homogeneous and inhomogeneous media. The results indicate that self-developing film is a potential candidate for quality control of radiation fields in radiotherapy, with special focus on dosimetric control of complex IMRT fields.

Key words: Radiotherapy, quality control, film, dosimetry, IMRT

Introduction

Self-developing radiochromic film has been available for a number of years and is a potential candidate as a tool for quality assurance in radiotherapy. However, its use as a quality assurance tool has been limited due to the availability of common industrial X-ray film and the presence of film developing facilities in most radiotherapy departments.

X-ray film for diagnostic purposes is rapidly being replaced by digital systems. In the Nordic countries, this has almost completely been carried out. Consequently, there are few arguments for continued use of the old film technology for radiotherapy purposes. Also, it is not unlikely that the use of film developing agents will, for environmental protection reasons, be heavily restricted in the near future.

The properties of common industrial X-ray film as a tool for quality assurance in radiotherapy are well known due to its use for more than 50 years in the field. Prior to changing to radiochromic film a thorough investigation of its properties as a quality assurance tool has to be undertaken. The purpose of this paper is to report investigations of a number of basic properties of the Gafchromic® EBT film (International Specialty Products, Advanced Materials Group, 1361 Alps Road, Wayne, NJ 07470, USA).

Materials and methods

Gafchromic® EBT radiochromic film (Lot no 35076-002AI) was investigated for this study.

All films were irradiated using a linear accelerator (Varian Clinac 2300, Varian Medical Systems, Palo Alto, CA, USA) using photon energies of 6 MV or 18 MV and an absorbed dose range between 0.1-3 Gy.

Irradiated films were scanned using an EPSON Perfection 4990 Photo flat bed scanner, which is an inexpensive and widely available standard flat bed scanner. The output from this scanner can be chosen in many formats ranging from 1 bit B/W to 48 bits colour. In this work the signal output chosen was either in 24 bit RGB or in 8 bit greyscale format. The pixel value output from the scanner can, if needed, be manipulated with a built-in tool which allows conversion of the pixel values using a conversion curve set by the user. In the following text this is referred to as *colour correction*. If the scanner signal not is manipulated, it is in the following called *uncorrected*.

The scanning software was initiated from Adobe Photoshop Elements 2.0 using a Twain interface. The scanned images were written to disk in bitmap format.

Quantitative analysis of the films were made using either the RisøScan Software [1] or the ImageJ analysis package (<http://rsb.info.nih.gov/ij/> NIH, Bethesda, MD, USA)

A. Absorbed dose calibration. For dose calibration, 18 square pieces of film of $2 \times 2 \text{ cm}^2$ were cut from the same sheet and irradiated with 6 MV X-rays in a solid water phantom (Gammex RMI, Middleton, WI, USA). The film pieces were placed at the maximum buildup depth (15 mm). The phantom was placed in the beam with a distance of 1000 mm from the focus to the phantom surface and with a field size of $20 \times 20 \text{ cm}^2$ giving a dose distribution as uniform as possible in the central area of the beam where the films were placed. The films were irradiated with different absorbed doses ranging from 0.1 to 3.0 Gy. The accuracy of the absorbed dose given is of the order of $\pm 1.5\%$.

After exposure the films were arranged on the scanner surface in ascending dose order including a non-irradiated piece of film. The film pieces were scanned together with a reference film strip of another type (Gafchromic® FWT, Risø B3), which is known not to change its colour properties with time. Absorbed dose calibration was done using the RisøScan software. The calibration procedure was thereafter repeated first on a weekly basis and later at increased time intervals.

Initially, the scanner was operated in uncorrected mode. In this mode, the minimum and maximum pixel values are around 80 and 190, respectively. This means that the dynamic range of the scanner (in 24 or 8 bit mode [0-255]) is not fully used, which makes the system less sensitive. In order to increase the sensitivity, the colour correction facility of the scanner was used. The output of the scanner was corrected using the function graphically illustrated in figure 1:

$$pixel\ value_{corrected} = \begin{cases} 0 & for\ pixel\ value_{uncorrected} \leq 58 \\ [2.09 \cdot (pixel\ value_{uncorrected}) - 121] & for\ 59 < pixel\ value_{uncorrected} \leq 180 \\ 255 & for\ pixel\ value_{uncorrected} > 180 \end{cases} \quad (1)$$

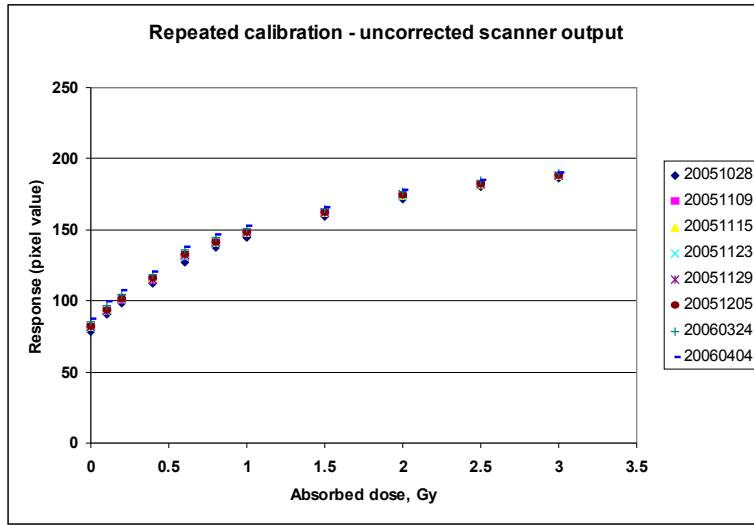


Fig. 1. Uncorrected and colour corrected mode of signal conversion from the scanner.

In this way, the output from the scanner is expanded into the full 8 bit pixel value range from 0 to 255.

B. Dependence on film orientation using small film pieces. From the same set of irradiated pieces of film that were used for dose calibration, films irradiated with 0, 0.1, 0.8 and 3 Gy were chosen. They were all oriented at angles 0, 90, 180 and 270 degrees and scanned. The films were also turned upside-down in the 0 degree position. After scanning the pixel value histograms were produced individually for the red, green and blue channels using the ImageJ software package.

C. Dependence on position of the film on the scanner surface. A piece of film was cut to a size of 15x15 cm² and was placed centrally at maximum dose depth in a solid water phantom. The film was irradiated with 3 Gy using a 30x30 cm² field, thus covering the whole phantom. The film was scanned, rotated 180 degrees, placed at the other end of the scanner surface and was scanned again. The scanner signal had no colour correction. Histograms for the red, green and blue channels were produced using the ImageJ software.

D. Effects on histogram of film rotation and colour channel using a large film. A film of 15x15 cm² was irradiated with 1 Gy in a solid water phantom and scanned to investigate the uniformity of the film. The film was scanned without colour correction in the same position on the scanner surface but rotated in different angles. It also was placed upside down in the zero degree angle position. Histograms for the red, green and blue channels were produced using the ImageJ software.

E. Modulation transfer function. The modulation transfer function (MTF) is easily found from the Fourier transform of the Line Spread Function (LSF). As the LSF is extremely difficult to measure, especially for high energy X-rays, the LSF was obtained from deriving the Edge Spread Function (ESF) data. The ESF was measured using a 5 cm thick piece of brass (density 8.7 g/cm³), which was carefully prepared and grinded with a computer controlled milling cutter into a piece having right angles at every corner.

A piece of film was placed in the centre of a 6 MV X-ray field. The film was placed on a thick plexiglass plate that was carefully aligned horizontally using a high grade spirit level. The gantry angle of the accelerator was also carefully set to zero degrees using the same spirit level, giving an entrance angle of exactly 90 degrees

to the film surface. The brass piece was thereafter placed with one edge exactly in the middle of the beam, thus producing a geometry for measurement of the edge spread function.

After scanning, the LSF data was obtained by deriving the ESF data and a Gaussian function was fitted by eye to the LSF data. The MTF was obtained by the absolute value of the Fourier transform of the Gaussian fit to the LSF data.

G. Low dose resolution. Four pieces of film were cut into a size of $15 \times 15 \text{ cm}^2$, placed at dose maximum in a solid water phantom and were irradiated with 0.5 Gy, 1.0 Gy, 2.0 Gy and 3.0 Gy in a solid water phantom. The images were analyzed using a computer program written especially for this purpose. The program places 20 circular regions of interest (ROI) with the same diameter randomly in the central part of the image. For each ROI its mean pixel value is calculated. The (grand) mean and standard deviation of the 20 mean values are calculated and converted to absorbed dose. The minimum detectable absorbed dose deviation from the surroundings for a ROI of a certain size is given as the ratio $3 \times \text{s.d.}/(\text{grand mean})$. The procedure was repeated for other ROI diameters.

H. Noise Power Spectrum. The computer program mentioned in section “G” also produced the Noise Power Spectra (NPS) for the same films. The NPS is given as the absolute value of the Fourier Transform of the image and is thus a two-dimensional function of frequency and phase. For simplicity and presentation purposes, the 2D NPS array was resampled to a one dimensional vector, averaging the data over all phase angles.

I. Comparison of dose distributions. One Gafchromic[®] film was placed between plexiglass blocks, forming a phantom with dimensions $35 \times 35 \times 35 \text{ cm}^3$. The phantom was irradiated with a $15 \times 15 \text{ cm}^2$ 18 MV field with a 60 degree wedge. The “slit” with the film was placed approximately 10 mm from the centre of the radiation field in order to avoid any effects of the air present in the thin slit outside the edges of the film.

The film was irradiated giving a maximum dose in the field of 3 Gy. Following scanning in the Epson scanner, the pixel values were converted to absorbed dose values. Isodose curves were produced with the contour plotting routine of the ImageJ software and were visually compared to those produced by the dose planning system (MDS Nordion TMS v6.1) which is used in the radiotherapy department.

In another experiment, two pieces of film were placed in an anatomical phantom (Alderson Rando phantom) in the pelvic area. This phantom is constructed using a human skeleton which is filled with a plastic which simulates the attenuation properties of human tissue very well. The phantom is divided into sections (“slices”) which are 25 mm thick. The films were placed between slices so that they were separated by 50 mm. The phantom was placed in a cast which pressed the slices firmly together. Again, none of the films were placed in the centre of the field in order to avoid effects of the thin air slit outside the film edges. The whole set-up was irradiated with a four-field technique with 6 MV X-rays and the experiment was repeated using 18 MV X-rays. The films were scanned, pixel values were converted to absorbed dose and isodose curves were produced with the ImageJ software. These curves were visually compared to the output of the dose planning system.

Results

A. Dose calibration. Stretching the pixel value histogram already in the output signal of the scanner (“colour correction”) significantly increases the sensitivity of the system. The overall slope of the calibration curve in the dose interval from 0.1 to 3 Gy is increased so that the minimum sensitivity increases from 89 to 190 pixel units/Gy at 0.2 Gy (+213 %) and from 15 to 27 pixel units/Gy at 3 Gy (+180 %). The calibration curves are given in figures 2 and 3.

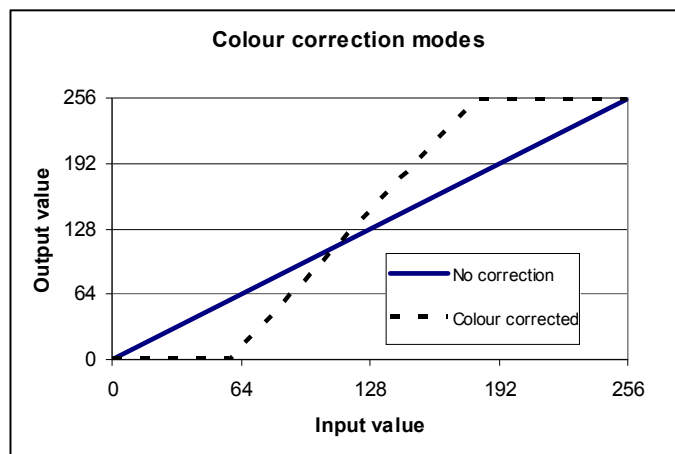


Fig. 2. Absorbed dose calibration curves for uncorrected scanner output

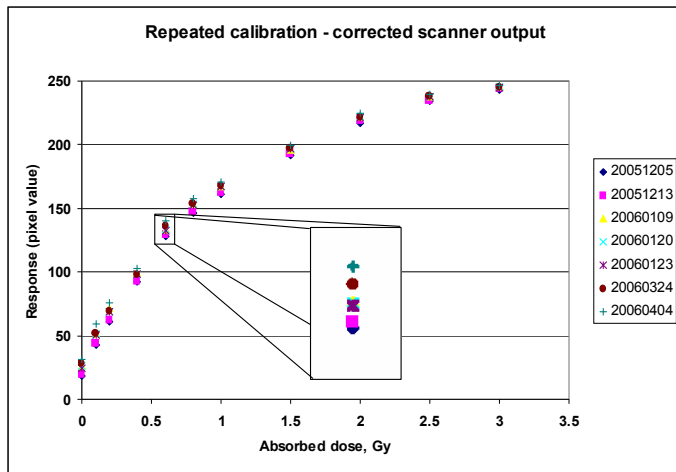


Fig. 3. Absorbed dose calibration curves for colour corrected scanner output

In these figures can also be seen that the film spontaneously darkens with time. Following analysis of these data, the effect of spontaneous darkening on absorbed dose value is given in figure 4. In this figure is illustrated the dose error for different dose levels if the film not is recalibrated before repeated readout at a later point of time.

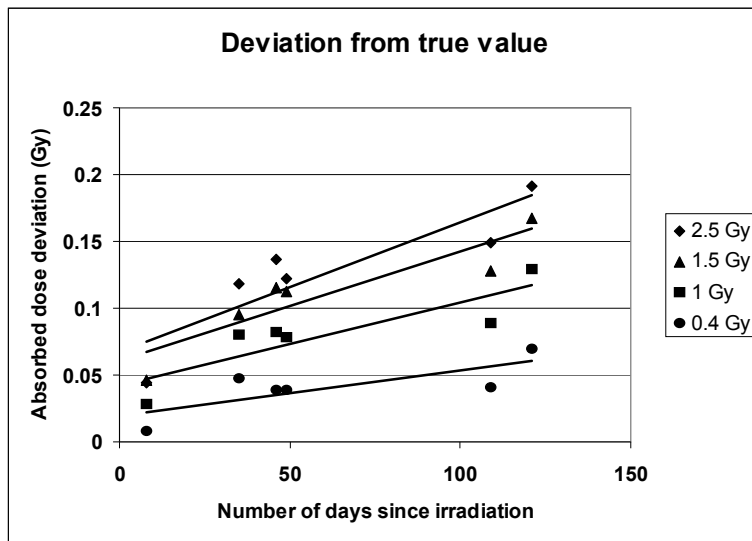


Fig. 4. Time dependence of spontaneous darkening of the film for different absorbed dose levels

B. Dependence on film orientation. Histograms of the pixel value distribution produced with the ImageJ software are given in figures 5a-d. The histograms are represented as a continuous distribution for clarity. The pixel distributions are decreasingly affected by orientation as the dose increases. The histograms for blue channel are clearly more affected by film orientation than those for the red or green channel, regardless of dose.

C. Orientation of the film on the scanner surface. The effect on histogram of placing the large $15 \times 15 \text{ cm}^2$ film in two different orientations (0 and 180 degrees) is shown in figure 6. The histograms are slightly affected and are shifted approximately one (1) pixel value for all three channels; all in the same direction. This shift is in agreement with what was found for the small films when they were rotated 180 degrees.

D. Effects on histogram of film rotation and colour channel using a large film. In figure 7 is shown the effect on histograms of rotation angle for the three colour channels. As for the small film pieces in section "B", the effect, however small, was most pronounced for the blue channel. The effect of rotation was of the same order as that of turning the film upside down, except for the blue channel, where the rotation affected the histogram significantly more.

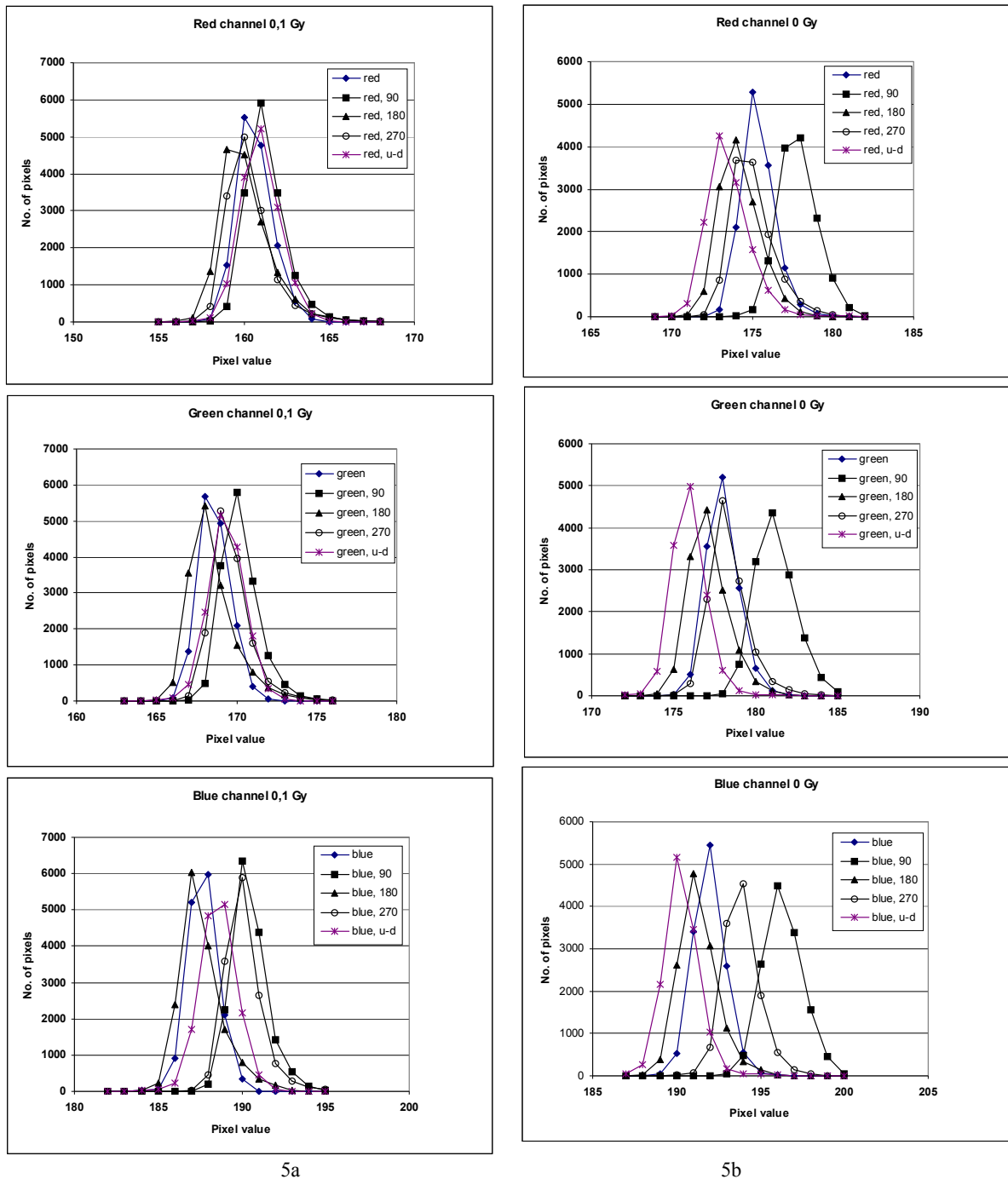


Fig. 5 a-b. Pixel value histograms (red, green and blue) in $2 \times 2 \text{ cm}^2$ films for different orientations at 0 Gy (5a), 0.1 Gy (5b)

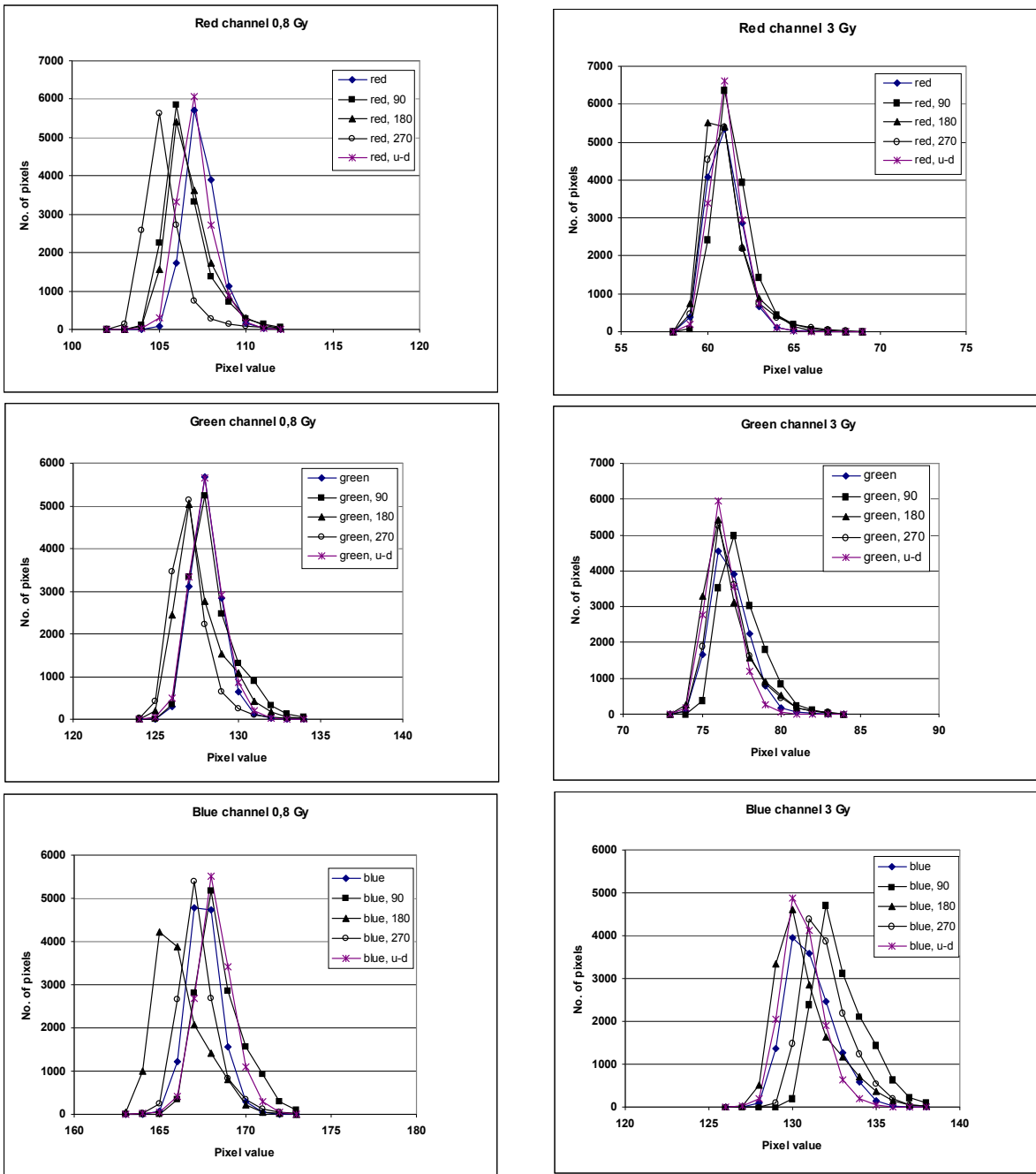


Fig. 5 c-d. Pixel value histograms (red, green and blue) in $2 \times 2 \text{ cm}^2$ films for different orientations at 0.8 Gy (5c) and 3 Gy (5d)

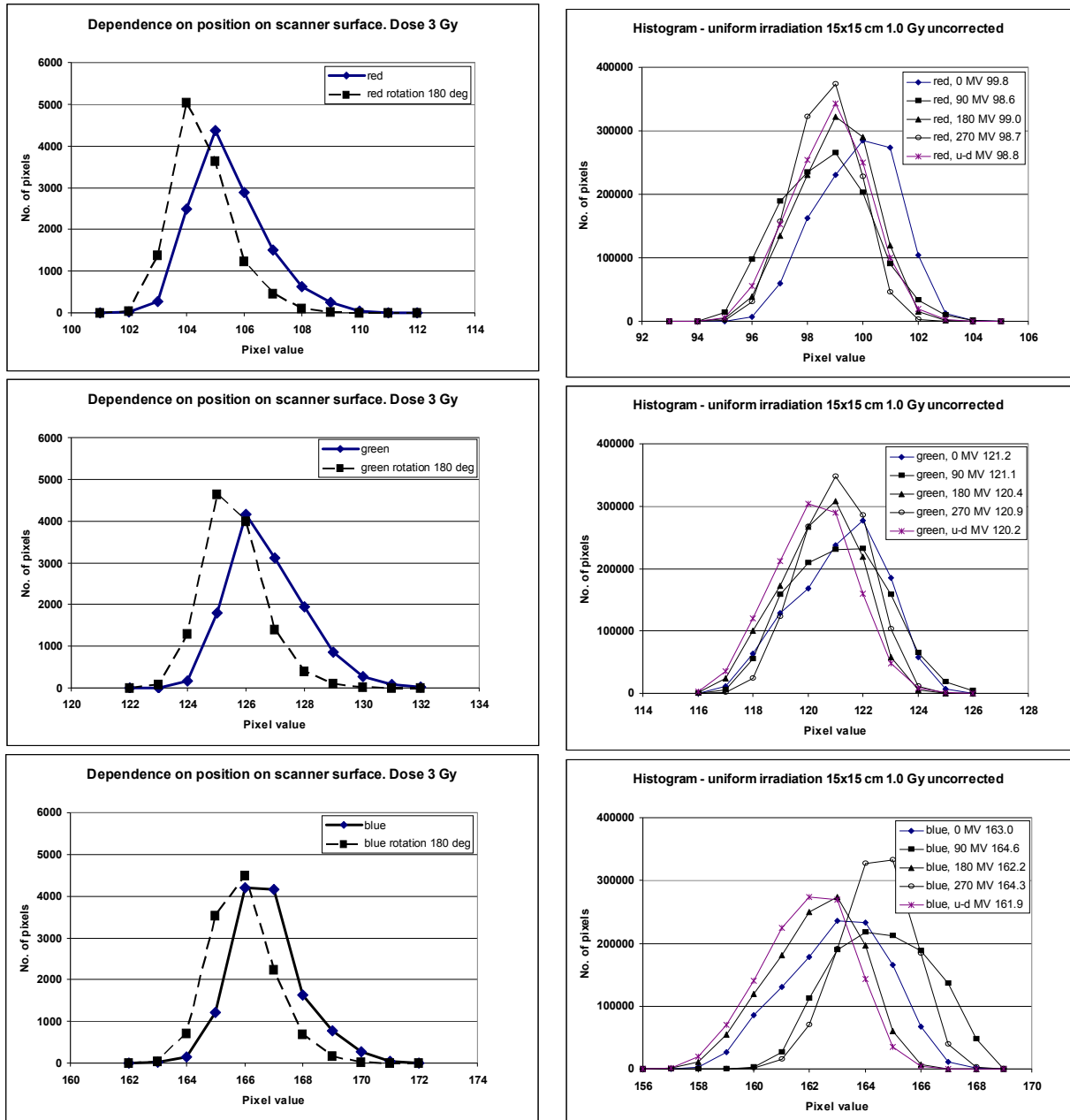


Fig. 6. Pixel value histograms (red, green and blue) for a film placed at 0 degrees at one end of the scanner surface and rotated 180 degrees and placed at the other end of the scanner surface.

E. Modulation transfer function. The edge spread function data (ESF) is given in figure 8. The little ‘notch’ in the ESF curve (see arrow) can not be explained and the effect of this notch is omitted in the analysis. From the ESF data, the line spread function (LSF) was obtained from derivation of the ESF. The LSF together with the Gaussian fit is given in fig.9.

Fig. 7. Pixel value histograms (red, green and blue) $15 \times 15 \text{ cm}^2$ films irradiated with 1.0 Gy and differently oriented when they were scanned.

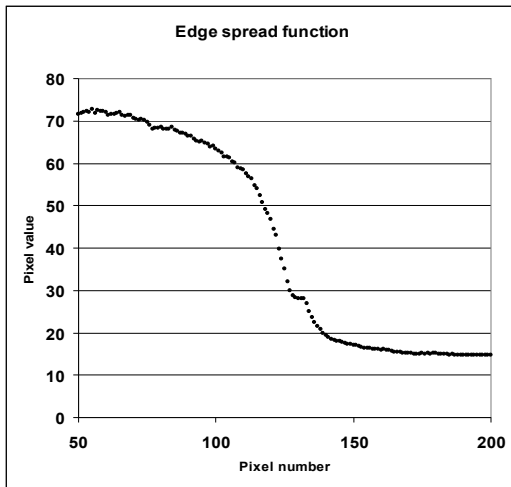


Fig. 8. Edge spread function ESF (in pixel values, colour corrected mode)

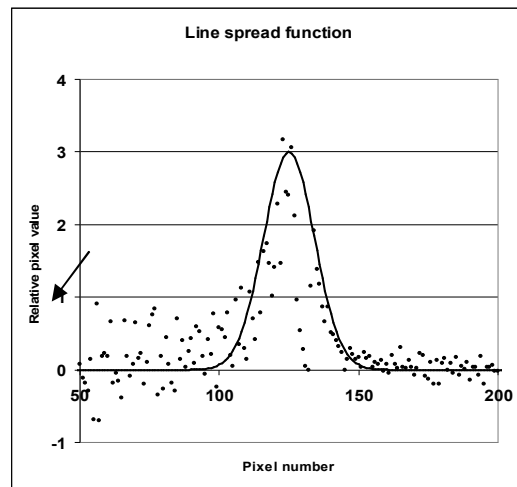


Fig. 9. Line spread function LSF, obtained as derivative of the ESF and the Gaussian fit (line)

The MTF curve, found as a FFT of the fitted LSF data, is given in figure 10.

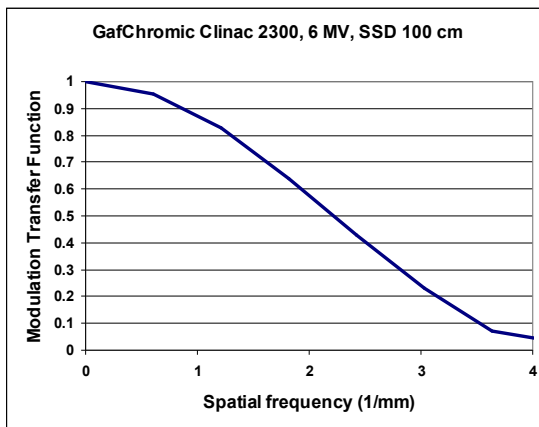


Fig. 10. MTF, given as the Fourier transform of the LSF

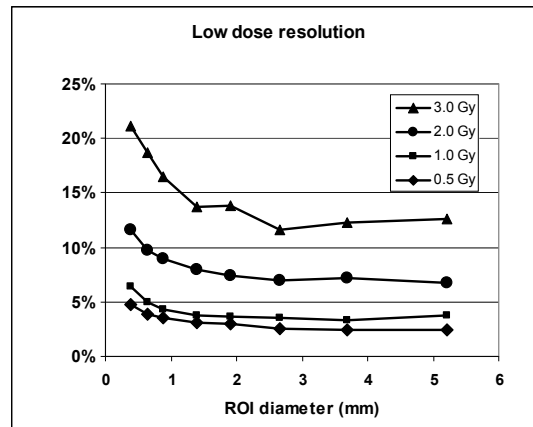


Fig. 11. Low dose resolution for the Gafchromic® film at different absorbed dose levels and for different size of the region of interest used for dose measurement.

F. Low dose resolution. The low dose resolution should be understood as the lowest change in dose, compared to the background signal, that can be detected with the film. This is illustrated in figure 11, in which can be seen that the film is most sensitive in the low dose region (0.5 and 1.0 Gy) and that the low dose resolution is not improving as the ROI for signal integration exceeds 2.5 mm in diameter, corresponding to approximately 400 pixels in size.

G. Noise Power Spectrum. The noise power spectra for the same films as in section “G” are shown in figure 12. Contrary and surprisingly to what the low contrast resolution results suggest, the amplitude of the noise power spectrum *increases* for all frequencies as the dose is lowered.

H. Comparison of dose distributions. The isodose distribution of the film which was irradiated in the cubic plexiglass phantom is shown in figure 13. The curves are normalized to the maximum dose value found within the field (mean value in a ROI with a diameter of 3 mm). The dose value calculated in that ROI using the film calibration curve was 2.97 Gy. The corresponding dose distribution from the dose planning system is shown in figure 14. The isodose levels and colour scheme for display are the same in both figures.

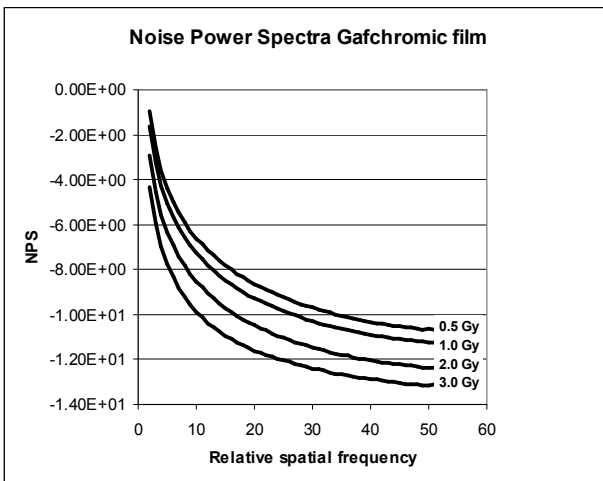


Fig. 12. Noise power spectra at different absorbed dose levels.

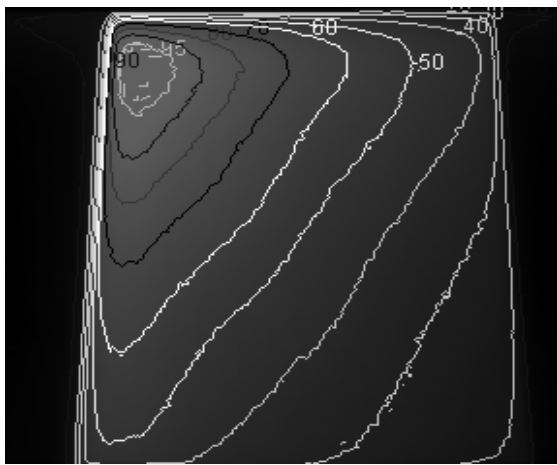


Fig. 13. Isodose distribution measured with Gafchromic® film measured for a 18 MV 15 x 15 cm² wedged field in a plexiglass radiation field

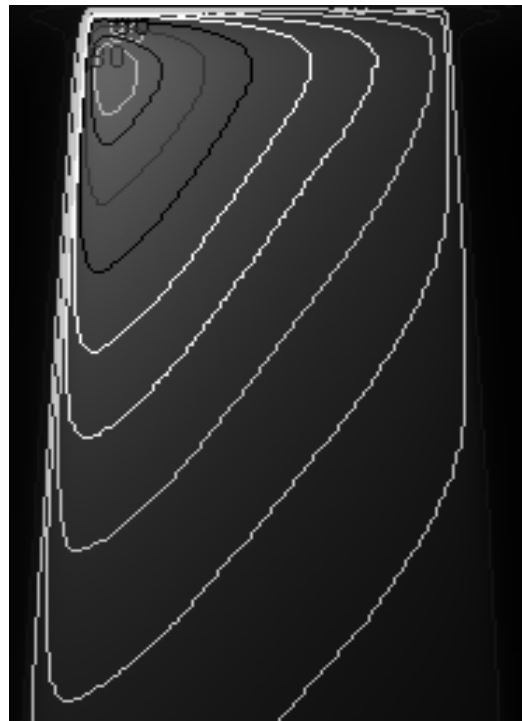


Fig. 14. Isodose distribution calculated by the dose planning system for the same phantom.

Dose distributions from films placed in the humanoid Alderson phantom and those given by the dose planning system are shown in figures 15 and 16. The isodose levels and colour scheme for display are the same in both figures. It can be noted that rather large discrepancies are found compared to the results for the case with the plexiglass phantom (figures 13 and 14).

Discussion

From these preliminary studies of the Gafchromic® film, it is clear that it has a potential as a candidate for some applications in clinical dosimetry and quality assurance for radiotherapy purposes. This is especially true for those applications which rely on an integrating dosimetry system capable of measuring the spatial distribution of absorbed dose with a high degree of geometrical definition. However, some properties of the film have to be considered and understood prior to bringing it into clinical use.

Spontaneous signal variation. It is evident that the signal will change with time. The change in signal depends on the irradiation and amounts to (see figure 17) 3 % (at 0.4 Gy) to 1.3 % (at 2.5 Gy) per month. These numbers apply to the situation when the film since irradiation has been stored in darkness at room temperature. This means that if a clinical film has to be scanned a second time at a later stage, a new calibration curve has to be produced using the set of calibration films produced at the same (or close to the same) time as when the clinical film was irradiated.

The reason for this spontaneous increase in signal is presently not known, but should be subject to further studies. Possible environmental factors such as influence of temperature and humidity should be investigated

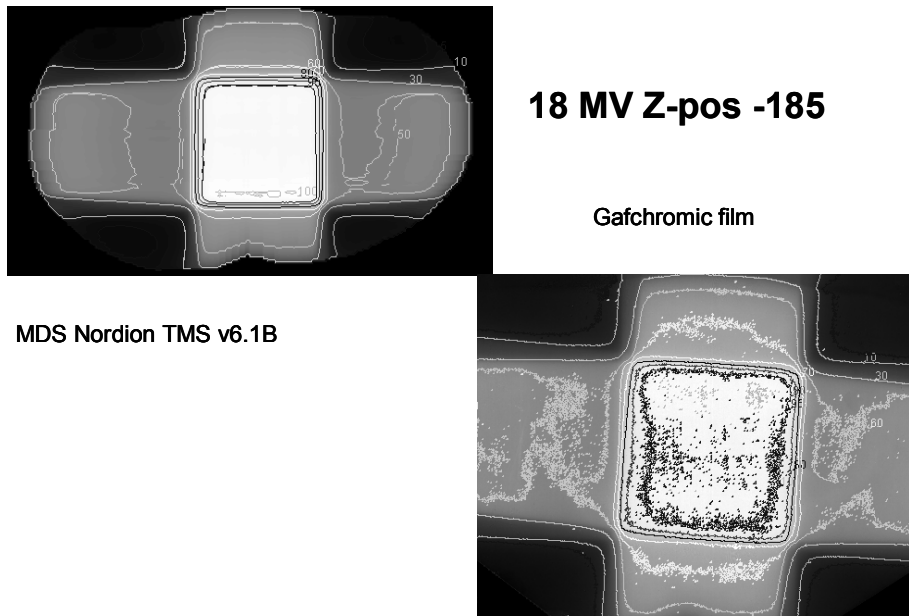


Fig. 15. Measured absorbed dose distribution for a four-field technique with 18 MV X-rays in a humanoid phantom compared to that calculated by the dose planning system

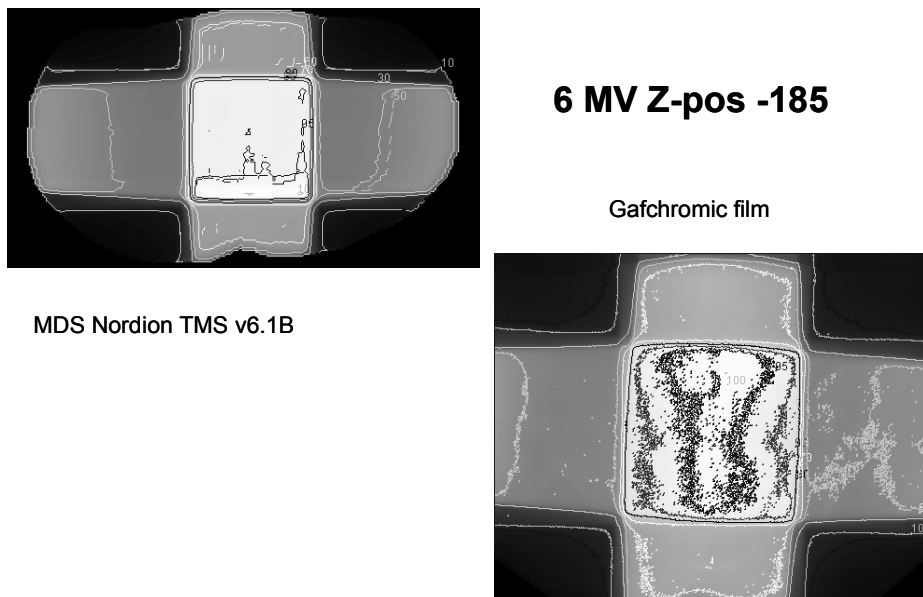


Fig. 16. Measured absorbed dose distribution for a four-field technique with 6 MV X-rays in a humanoid phantom compared to that calculated by the dose planning system

Choice of measuring channel in an RGB scanner and sensitivity to different orientation. The film base in itself has a light hazy blue colour. In theory, the best results should be obtained using the complementary colour to blue when measuring the signal, thus omitting the blue component. When studying the pixel value histograms at different dose levels it could be seen that for the lowest dose levels (0.1 Gy) the pixel values measured were affected up to 5 % by the orientation of the film when it was rotated in 90-degree steps. Turning the film upside-down affected the result much less. When the dose was increased, this effect decreased rapidly, however, for the blue channel it was still clearly seen even at the highest doses. The reason for this is probably reflection phenomena between the different layers inside the film which are more pronounced in the blue component due to the blue colour of the film base. These findings were reproduced when the experiment was repeated with a larger film ($15 \times 15 \text{ cm}^2$) irradiated with 1.0 Gy.

Placing the film on another part of the scanner's surface does not affect the result as when rotating the film. This can be seen in figure 8 where the histogram is shifted approximately one (1) pixel value when the film, irradiated with 3 Gy was rotated 180 degrees and placed at the other end of the scanner's surface. The same shift

was noted for the small films (irradiated with 3 Gy) when they were rotated and placed in the same area on the scanner. This result indicates that the scanner is sufficiently stable during scanning.

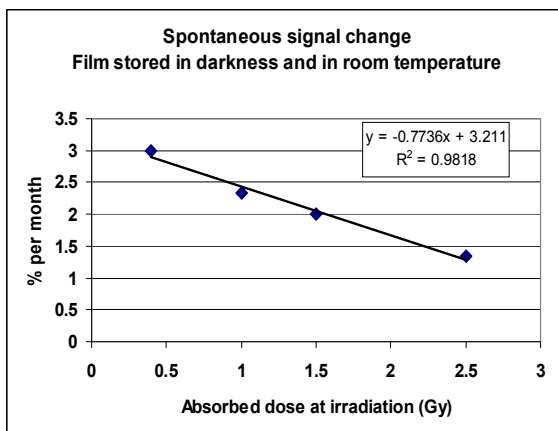


Fig. 17. Dependence of the absorbed dose at irradiation of the spontaneous signal change.

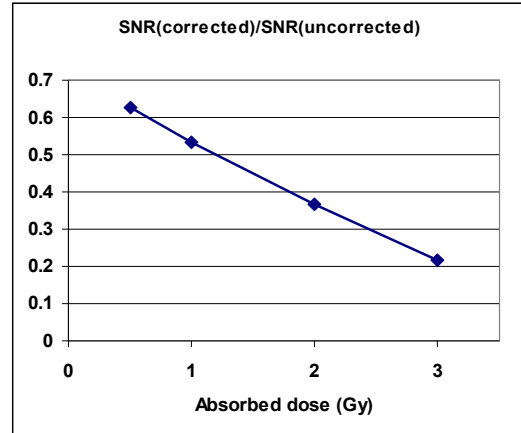


Fig. 18. Influence on the SNR of colour correction

In consequence, measurements should only be based on the green and/or the red channel and careful attention has to be given to that the orientation of the films used for calibration and measurement are the same.

Increasing the system sensitivity by correcting the scanner signal output. It is obvious that the full dynamic range of 8 bits should be utilized for maximum sensitivity. However, increasing the sensitivity using the colour correction curve in figure 1 also affects the noise level and thus the signal-to-noise ratio (SNR).

Applying the correction equation (eq. 1) for uncorrected pixel values between 59 and 180 means that the pixel noise will increase with 209 %. This noise level will not be affected when subtracting the offset value. However, the absolute pixel values will be affected as the whole pixel value distribution is shifted 121 units towards zero. This means that the SNR will be lowered for the colour corrected data, increasingly with increasing dose due to the increasing effect of the offset (=121) for lower uncorrected pixel values. This is illustrated in figure 18.

The low dose resolution properties are reflected by the SNR characteristics. To determine the lowest absorbed dose variation that can be detected in a surrounding “background”, the signal variation in the background has to be determined. In this work, this variation is taken as the standard deviation of the mean value in 20 regions of interest placed randomly but rather close to each other centrally in a uniformly irradiated film. An absorbed dose variation is considered significant if it differs from the background with more than three such standard deviations. This method has since long been used in signal theory on one dimensional data. However, it has been argued if two or three standard deviations should be used as criterion. To be on the safe side, three SD:s is used in this work.

As expected, the ability to measure small spatial fluctuations in dose decreases as the dose is increased (see figure 11). The ability to demonstrate small spatial dose fluctuations is remarkably good, being around 3-4 % for absorbed doses up to 1 Gy in a measurement region exceeding 1 mm in diameter. For 2 Gy the figure is still acceptable (7-8 %), whereas for 3 Gy the SNR has decreased so the figure is 13-15 %. For precision measurements using Gafchromic® film, the absorbed dose should therefore be restricted and should not exceed 1 Gy.

Measuring the *spatial resolution properties of the film* for megavoltage X-rays is a difficult task due to the high energy of the X-rays in a medical accelerator. Choosing the appropriate thickness of the object giving the edge spread function (ESF) is a compromise between X-ray penetration and alignment in the beam. Also, the measured ESF includes contributions from scattered radiation from the accelerator head and the absorbing object, effects of a X-ray focus *not* having an infinitely small area, effects of misalignment of the absorber etc. In order to obtain the true MTF, each of these contributions should be measured separately and deconvolved from the measured (total) line spread function. Unfortunately, they are almost impossible to measure one by one or even as a total disturbance. Therefore, the MTF given should be looked on as a “system MTF” rather than the true MTF of the Gafchromic® film. In fact, this is what is most clinically relevant.

When the *Noise Power Spectra* (NPS) are compared to the low dose resolution, the results are contradictory. A higher SNR should normally give a NPS with lower amplitude. It was not until the images were examined very carefully that the reason for this was discovered. When viewing the images with a very narrow window setting (approximately 10 pixel value units) a phenomenon resembling “Newton rings” appears on the low dose images. These artefacts gradually disappear as the dose is increased and can not be seen at 3 Gy. The film in figure 19 is irradiated with 0.5 Gy and in figure 20 with 3.0 Gy. The explanation why these artefacts appear is probably interference of reflected light from the different layers in the Gafchromic® film.

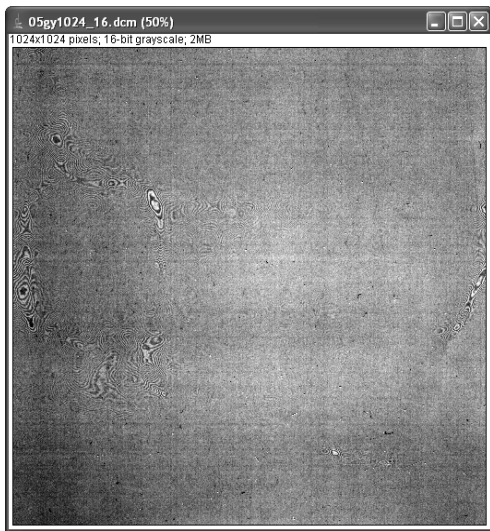


Fig. 19. A $15 \times 15 \text{ cm}^2$ film irradiated with 0.5 Gy and displayed with a very narrow window setting.

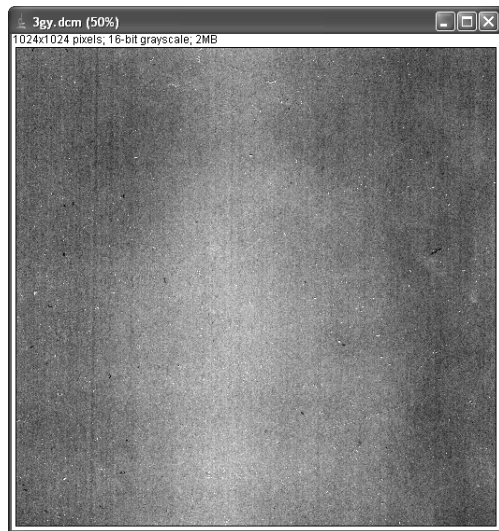


Fig. 20. A $15 \times 15 \text{ cm}^2$ film irradiated with 3.0 Gy and displayed with a very narrow window setting

The low dose resolution was measured using a number of ROIs that were placed in the central area of the film, in which the artefacts never appeared at any dose level. As the NPS are calculated from the entire film area, the artefacts has such great influence that the NPS amplitude increases as the dose is lowered, which explains the contradictory results.

The very good low dose resolution, at least for absorbed doses below 2 Gy, together with a reasonably good spatial resolution, indicates that the Gafchromic® film should perform well for *displaying dose distributions*. This is confirmed by figures 13 and 14, where a dose distributions is compared to that from the dose planning system; the latter being known to be very close to the true distribution. The isodoses coincide well and it should be noted how well the film performs at the edges of the field where the dose gradient is very steep.

When comparing the dose distributions in the irradiated Alderson phantom (figures 15 and 16), the dose distributions do not coincide as well as for the experiment using the plexiglass phantom. As this discrepancy could be a problem connected to the calculation accuracy of the dose planning system it is beyond the scope of this paper to discuss the underlying reasons. However, it can be noted that the ability of the Gafchromic® film to visualize isodoses in the high dose region (3 Gy) clearly is impaired due to the decrease in low dose resolution at high doses that has been discussed above.

Conclusion

Self-developing Gafchromic® film clearly has a potential for use as a quality assurance tool in radiation therapy. However, careful attention has to be given to control a number of factors in order to achieve the accuracy and precision needed for absolute and relative dosimetry. The most important factors found so far are 1) a dose-dependent sensitivity to film orientation in the scanning device, 2) a time- and dose-dependent spontaneous signal shift, 3) a dose dependent SNR and 4) a position-dependent low dose resolution. Further studies of basic film properties are needed and modifications of scanning device and procedures have to be further investigated. It is, however, our impression that the additional work that has to be done probably is well worthwhile and will lead to a tool with a high potential for radiation therapy quality assurance.

References

1. RisøScan – a new dosimetry software. Radiation Physics and Chemistry 71 (2004) 359-362

OPTICAL CHARACTERISTICS AND BACTERICIDE ACTIVITY OF PHOTOGENERATED SILVER AND GOLD NANOPARTICLES IN SOLUTION AND ON THE SILICA SURFACE

A.M. Eremenko, G.V. Krylova, Yu. I. Gnatyuk, N.P. Smirnova, E. S. Tuchina¹, D. V. Rudik¹, and V. V. Tuchin¹

Institute of surface chemistry, National Academy of Sciences, Ukraine 03164 Kyiv, General Naumov str., 17,

email: annaerem@voliacable.com

¹Saratov State University, Saratov, 83 Astrakhanskaya str., Saratov, Russia, 410012

Abstract

New photoactive material, obtained via modification of silica by benzophenone (BP) for reduction of silver and gold ions and formation of its' nanoparticle both stabilized in aqueous solution and on the surface of SiO₂ is revealed. Irradiation of the system SiO₂-BP_{ads} / Ag⁺(Au³⁺)_{solut} in the presence of stabilizers – colloidal silica Ludox or surfactants leads to appearance of surface plasmon resonance bands in the absorption spectra with the maxima at 390nm for silver and 520nm for gold nanoparticles.

The irradiation of *Staphylococcus lugdunensis* and *Micrococcus halobius* by a broadband light in presence of Ag-SiO₂ nanoparticle film decreases population's quantity relatively to control for certain.

Key words: mesoporous silica films, silver, gold nanoparticles, benzophenone (BP), photoreduction, surface plasmon resonance, microorganisms

Introduction

The preparation of small noble metal particles at the nanoscale has received increasing attention due to unique properties of such particles which result in their application in chemical catalysis, in cancer diagnostics, as antimicrobial tools [1-4]

Among a number of methods have been applied to generate noble metal nanoparticles the photochemical methods have a several advantages, e.g., provide easy control of reaction kinetics. The photochemical reaction of benzophenone (BP) with isopropyl alcohol [5-8] can be transferred to the silica interface to produce the material with high photoreductive yield concerning removal of transient and noble metal ions from aqueous solution. In this work, the photosensitizer, benzophenone, has been adsorbed on the surface of photochemically inactive silica film. Mesoporous silica films have been synthesized via a low-temperature sol-gel process of the acid hydrolysis of tetraethoxysilane in the presence of template agents. Porous silica powders have also been used. These SiO₂-BP films and powders have been used as photoreduction agents to generate silver and gold nanoparticles in colloid solutions. Chemical and physical modifying of silica surface with photoactive organic compounds allow us to obtain heterogeneous photosensitive systems advantageous for redox photocatalysis, which are able to compete with semiconductors (for example TiO₂) which are usually used for this purposes.

In the present work we created a new photocatalytically active material, obtained via modification of silica surface by the molecules of organic sensitizer – benzophenone (BP) for reduction of silver and gold ions and formation of its' nanoparticle both stabilized in aqueous solution and on the surface of SiO₂. BP molecules in photoinduced triplet excited state are able to abstract hydrogen atom from aliphatic alcohol, forming two ketyl-radicals, which have high negative electrochemical potential and could reduce noble and transition metal ions [5-8].

Experimental

Film preparation. The mesoporous silica films have been prepared by the sol-gel method using nonionic tri-block copolymer Pluronic EO₂₀PO₇₀EO₂₀ (P123, Aldrich) by the method described in literature [9]. The precursor sol was prepared by hydrolysis of TEOS in a mixture of distilled water, ethanol (Fluka), and 1 M HNO₃ solution. Twenty-four hours after hydrolysis, either an ethanolic solution of P123 was added to this solution. The total molar ratio was 1 TEOS: 0.008 P123: 0.16 HNO₃: 15 H₂O: 15 C₂H₅OH. To prepare Ag⁺-containing SiO₂ coatings with 0.1 Ag/ SiO₂ atomic ratios, aqueous solutions of AgNO₃ were added to the hydrolyzed silica sol before film deposition procedure.

The coatings were deposited onto a clean glass substrates by the dip-coating technique. The films were dried for 12 hours at ambient temperature, followed by heat treatment at 400⁰ C with a rate of 1⁰ C/min and calcinated at 400⁰ C for 6 h.

The adsorption of BP on silicagel (SG) and SiO_2 films was carried out from hexane solution. To measure the adsorption isotherm, the samples were thermoactivated at 250°C , and silica was placed in the BP hexane solution with the initial concentration in the range 10^{-5} to 10^{-3} M for 24 h to achieve the adsorption equilibrium. The amount of adsorbed BP molecules was monitored by the measurements of the optical density of BP at 355nm using Lambda UV-Vis spectrophotometer (Perkin Elmer). We detected negligible BP desorption from silica-BP system after prolonged contact of silica-BP with water under stirring. Porous silica powders and SiO_2 films with adsorbed BP have been investigated as catalysts in the photochemical reduction of silver and gold ions in water-alcohol solvent under mercury lamp irradiation. In accordance with Yonezawa et al [10], colloid silica plays role of stabilizer of colloid nanoparticles in solution and prevents their precipitation and aggregation. An aqueous solution containing AgNO_3 or HAuCl_4 ($1.5 \times 10^{-4}\text{M}$), i-pro (0.4M), and Ludox (1%) was irradiated with 254nm or 365 nm light in presence of SiO_2 with adsorbed BP (films or powders). The catalyst is removed immediately after irradiation and the absorption spectra of the irradiated solutions are measured.

Microorganisms and photodynamic studies The pure bacterial strains used in this study were *Staphylococcus lugdunensis* and *Micrococcus halobius* taken from the oral cavity of patients with caries diagnosis. In experiments 24-hours cultures were used. Suspensions of bacteria ($10^3/\text{ml}$) were placed on glass with nanofilms. Used films samples TiO_2 10%, Ag-SiO_2 10%. As a light source a halogen lamp with wavelength ranges from 380 to 800 nm and provided doses ranging from 6 to 90 J/cm^2 at a power density of 100 mW/cm^2 was used. After irradiation bacterial suspension was placed on plates with all culture medium (Difco). Number of survival cells was calculated after 24-hours incubation at 37°C by counting the CFU on the plates and dividing by number of colonies from control plates that were not exposed to light and photosensitize.

Results and discussion

Irradiation of the system $\text{SiO}_2\text{-BP}_{\text{ads}} / \text{Ag}^+(\text{Au}^{3+})_{\text{solut}}$ in the presence of stabilizers – colloidal solution silica (Ludox) leads to appearance of a new symmetrical band in the absorption spectrum of solution with the maximum at around 390-410 nm for silver and 520-530nm for gold nanoparticles (Fig.1). The intensity of the surface plasmon resonance absorption band is proportional to the nanoparticle concentration. Such bands appear due to excitation of collective resonant oscillations of electron gas at the surface of metal particles, whose sizes are smaller, than free path length of the electron (52 nm for silver), under the effect of electromagnetic field of light wave, and are generally called surface plasmon resonance (SPR) bands.

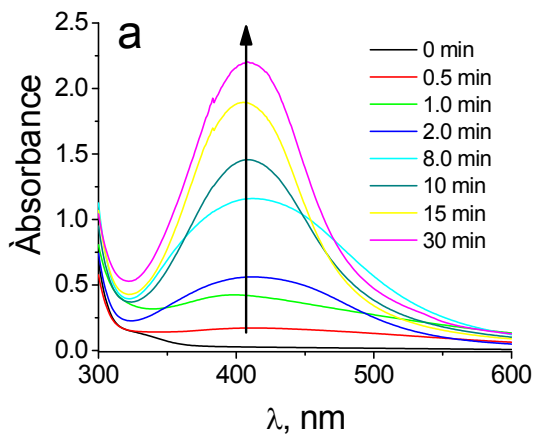


Fig.1. Absorption spectra of silver nanoparticles in solutions generated using $\text{SiO}_2\text{-BP}$ film at various irradiation times.

Generation of $\text{SiO}_2\text{-Ag}$ films. To prepare $\text{SiO}_2\text{-Ag}$ films with 0.1 Ag/ SiO_2 atomic ratios, an aqueous solution of AgNO_3 was added to the hydrolyzed silica sol before the film deposition procedure. After calcinations in air at 400°C transparent colorless films were produced with no traces of silver nanoparticles. Irradiation of the $\text{SiO}_2\text{-Ag}$ film was carried out in a solution of $1.4 \times 10^{-3}\text{M}$ BP, $1.7 \times 10^{-3}\text{M}$ SDS, and 1.84M IPA in aqueous solution. SDS was used to increase the solubilization of BP in the alcohol-water solution. SDS could also act as a hydrogen donor in the reaction with BP triplet. Absorption spectra and SEM image of silica film comtained with silver nanoparticles are shown at Fig.2 confirming the presence of silver nanoparticles on the surface and in the interior of the silica film. Particle size is observed to be 5-10 nm, which is in agreement with the XRD measurements.

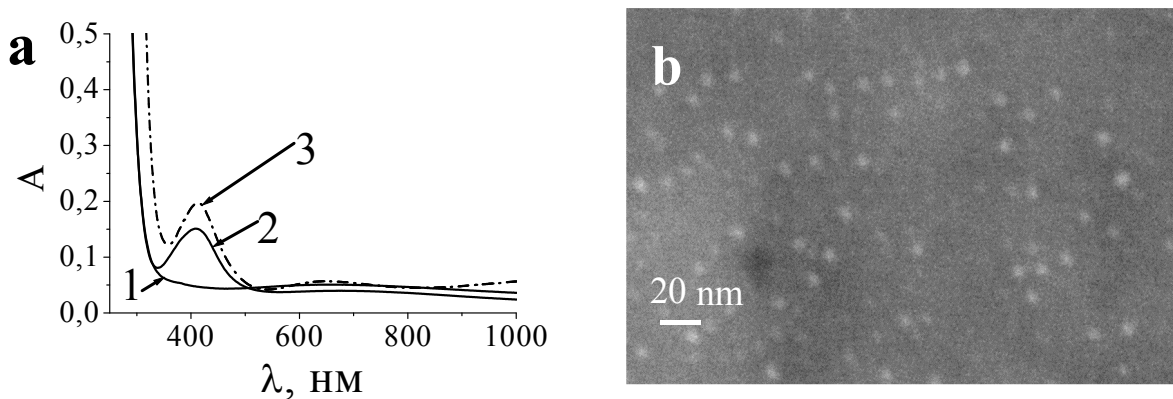


Fig.2. a) Absorption spectra of $\text{SiO}_2\text{-Ag}$ 2% films before (1) and after irradiation of 15 min (2) in the $1,4 \times 10^{-3}$ M BP solution in IPA. (3) – $\text{SiO}_2\text{-Ag}$ film after 6h of treatment at 500°C . b) SEM image of $\text{SiO}_2\text{-Ag}$ film after 15min irradiation.

It is necessary to note, that with the $\text{SiO}_2\text{-BP}$ powders the silver nanoparticles attach to the silica surface, while no nanoparticle deposition on the $\text{SiO}_2\text{-BP}$ film is observed, probably due to the small size of the silica pores for embedding of silver nanoparticles, smaller available surface, and charge density as compared to $\text{SiO}_2\text{-BP}$ powder.

Irradiation of BP/ SiO_2 – AuCl_4^- in presence of stabilizer 1% Ludox results in the formation of nanosized gold particles which are adsorbed on the colloid silica Ludox particles (Fig.3).

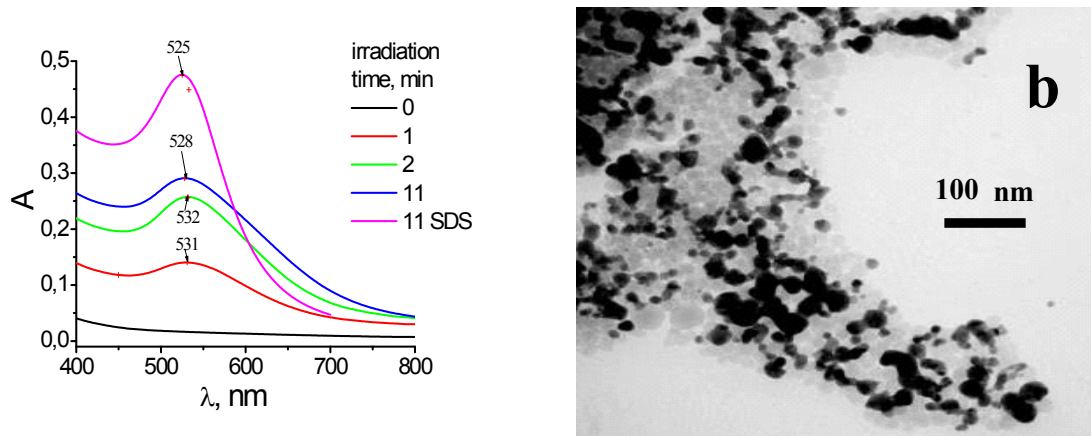
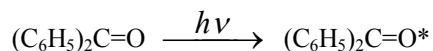


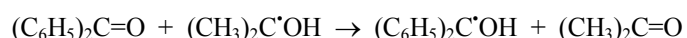
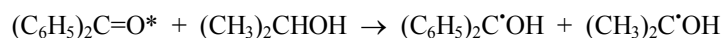
Fig.3 Absorption spectra and TEM image (right; scale bar is 100nm) of Au nanoparticles solution stabilized by Ludox versus irradiation time at $\lambda_{\text{irrad}}=253,7$ nm. The highest curve is the spectum of Au np solution stabilized by SDS after 11 min irrad., given for comparison.

From the pH studies, it could be concluded that the ketyl radicals and anion-radicals of BP and IPA take part in the reduction of silver ions. These synthetic studies provide another approach to photochemical reduction by immobilizing a reactant on the silica surface, allowing control of the reaction, and generation of silver nanoparticles in solution, attached to powders or inside the film for catalytic applications or increased conductivity of silica films [11]. In accordance with previous publications [12,13] and based on the obtained results, we suggest the following reaction mechanism:

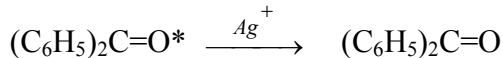
- 1) Photoexcitation of triplet state of adsorbed benzophenone



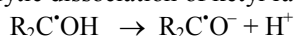
- 2) Hydrogen atom abstraction by benzophenone triplet from isopropanol



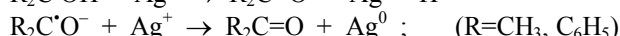
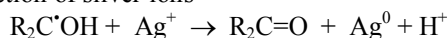
3) Quenching of BP triplet by silver ions



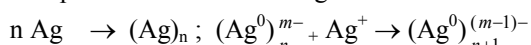
4) Protolytic dissociation of ketyl radicals [26, 44]



5) Reduction of silver ions



6) Silver nanoparticles formation and growth



It was revealed that irradiation of *Staphylococcus lugdunensis* and *Micrococcus halobius* by a broadband light decreases population's quantity relatively to control for certain. Greater effect we have found in experiments with such photosensitize as Ag-SiO₂ nanoparticle film, as well as colloid solutions of silver and gold nanoparticles. Light without exogenous photosensitizes suppressed bacteria growth as well, but considerably less than with Ag-SiO₂ nanoparticle film, therefore some endogenous chromophores with a photodynamic action can be supposed to be involved in the bacteria inhibition process. Pigmented *Micrococcus halobius* was more susceptible for photodynamic action. Irradiation of the test-cultures, photosensitized Ag-SiO₂, inhibit bacterial cell division. Microbial quantity of *Staphylococcus lugdunensis* decreased up to 20% in average, and for *Micrococcus halobius* – to 50%. Evidently, interaction of endogenous and exogenous photosensitizes under influence of light caused significant bactericidal action.

Conclusion

Porous sol-gel produced silica films and powders modified with adsorbed benzophenone molecules have been found to be effective in the photoreductive formation of silver and gold nanoparticles. The formation of noble metal nanoparticles within the thin silica film has been achieved by introducing of corresponding ions in the SiO₂ matrix during the sol-gel preparation process and subsequent irradiation in the BP-IPA medium. These structures can be used for diverse purposes such as supported catalysis of metal clusters, removal of metal ions from solution, increased conductivity of silica films and for antimicrobial photodynamic therapy.

References

1. Weiss R.M., Warshel A., Catalysis of hydrogen production in irradiated aqueous solution by Gold soles *J. Am. Chem. Soc.*, **101**, pp. 6133-6135, 1979.
2. T. Hirakawa, P. V. Kamat, Photoinduced electron storage and surface plasmon modulation in Ag-TiO₂ clusters. *Langmuir*, **14**, pp. 5645-5647, 2004.
3. I. H. El-Sayed, X. Huang, M.A.El-Sayed, SPR Scattering and Absorption of anti-EGFR Antibody Conjugated Gold nanoparticles in Cancer Diagnostics:Application in Oral Cancer. *Nanoletters*, **5**, pp. 829-834, 2005.
4. J.P. Gugenbichler, M. Boswald, S. Lugauer, T. Krall, A new technology of microdispersed silver in polyurethane induces antimicrobial activity in central venous catheters. *Infection*, **27**, pp.16-23, 1999.
5. S. Kapoor, D. K. Palit and T. Mukherjee, *Chem. Phys. Lett.* Preparation, characterization and surface modification of Cu metal nanoparticles 355 (2002) 383-387.
6. N. Kometani, H. Doi, K. Asami and Y. Yonezawa, *Phys. Chem. Chem. Phys.* Laser flash photolysis study of the photochemical formation of colloidal Ag nanoparticles in the presence of benzophenone 4 (2002) 5142-5147.
7. T. Sato, N. Maeda, H. Ohkoshi and Y. Yonezawa, *Bull. Chem. Soc. Japan* Photochemical Formation of Colloidal Silver in the presence of Benzophenone 67 (1994) 3165-3171.
8. G. Krylova, A. Eremenko, N. Smirnova, S Eustis. Structure and spectra of photochemically obtained nanosized silver particles in presence of modified porous silica // *Int. J. Photoenergy.* – 2005. – V.7. – P. 193-198.
9. Y. Takeguchi, T. Ida, K. Kimura. Colloidal Stability of Gold Nanoparticles in 2-Propanol under Laser Irradiation // *J. Phys. Chem. B.* – 1997. – V. 101. – P. 1322-1327.
10. Y. Yonezawa, T. Sato, M. Ohno, and H. Hada, *J. Chem. Soc., Faraday Trans. Photochemical Formation of Colloidal Metals* **83** (1987), 1559.
11. S. Eusti, G. Krylova, A. Eremenko, N. Smirnova, A. W. Schill and M. El-Sayed. Growth and fragmentation of silver nanoparticles in their synthesis with femtosecond laser and UV light by photo-sensitization with benzophenone // *Photochemistry and photobiology science*, 2004, N 11, p. 115-123.
12. Y.Yonezawa, T.Sato, Sh.Kuroda. Photochemical Formation of Colloidal Silver: Peptizing Action of Acetone Ketyl Radical // *J. Chem. Soc., Faraday Trans.* – 1991. – V.87. – P.1905-1910.
13. Henglein, A. Colloidal Silver Nanoparticles : Photochemical Preparartion and Interaction with O₂, CCl₄, and Some Metal Ions // *Chem. Mater.* – 1998 – V. 10 – P. 444-450.

SILVER NANOPARTICLES

J. Puišo^{1,2}, A. Šileikaitė^{1,2}, A. Guobienė^{1,3}, S. Tamulevičius^{1,2}
I. Prosyčėvas¹, A. Juraitis¹

¹ Institute of Physical Electronics, Kaunas University of Technology

² Department of Physics, Kaunas University of Technology,

³ International Study center, Kaunas University of Technology,

Abstract

A method for size-controlled synthesis of silver nanoparticles in polymer is proposed and described. The synthesis is based on the reduction of silver nitrate by hydroquinone in water. The method allows to synthesize particles of 60 nm diameter. Nanoparticles were characterized by UV-Vis spectroscopy, X-ray diffraction (XRD) and X-ray fluorescence (XRF) techniques.

Key words: silver, nanoparticle, X-ray radiation

Metallic nanoparticles have been the subject of extensive research in the past several years [1]. In particular, noble metal nanoparticles (e.g., Au and Ag) with their associated strong plasmon resonance have generated great interest in fields such as nanoscale photonics and biological sensing [1-5]. Metal nanoparticles can be dendritic macromolecules or reversible block copolymers, which provide hydrophobic interiors suitable for the storage of many polycyclic anticancer agents, or could be used in radiological treatments to achieve the same overall result, the destruction of pathogenic cells.

Furthermore, manipulation of these nanoparticles on surfaces by attaching antibodies or other ligands (such as vitamins) allows the metal nanoparticles to preferentially target cells, which express receptors that correspond to the ligand on the surface of the nanoparticle. It may exploit natural cellular uptake mechanism causing the nanoparticles to concentrate in desired pathogenic cells. One concentrated in a region of the human body, most likely within a tumor, radiological techniques could be used for imaging and therapy. The unique photo-physical and spectral characteristics of these nanoparticles make them ideal for such radiological techniques [6-10].

However the absorption of ionization radiation by matter is proportional to the density of the absorbing medium, and high radiation doses could change the size and shape of the adsorbed nanoparticles. As the absorption efficiency of incident radiation by single metal nanoparticle increases, the radiation dose necessary decreases, resulting in lower systematic toxicity from the radiological treatment [7-10].

The most common methods used for the preparation of colloidal suspensions of metals (including silver) are the reduction of corresponding metal cation. In addition to inorganic or organic reduction agents, an ultrasound, UV radiation and gamma radiation can be used to initiate the reduction [1-5].

In this work we report a simple and novel method to fabricate Ag nanoparticles in polymer matrix. The structure and optical properties of the silver nanoparticles in polymer matrix were characterized by UV-VIS spectroscopy, X-ray diffraction (XRD), X-ray fluorescence (XRF) measurements. The influence of X-ray irradiation on characteristics of silver nanoparticles in polymer matrix was investigated.

Polymer blends solutions were produced by mixing chloroform solutions with the weight concentration 2.5% of the homopolymers in the desired proportions (25%PS:75%PMMA and 50%PS:50%PMMA, (Sigma Aldrich, UK)). Polymer blends were deposited onto amorphous silica substrate by spin-coating ($r=2000 \text{ min}^{-1}$) and then dried in a horizontal position at room temperature in a chamber with constant humidity (60%). Substrate was cleaned chemically and with oxygen plasma ($RF = 13.56 \text{ MHz}$, $P=0.3 \text{ W/cm}^2$, $t=5\text{-}60\text{s}$). The surface patterning was done by extraction of PS from PS-PMMA structure. The PS extraction was done in cyclohexanone solution exposing blends for 30s and after this drying in vacuum ($p=10^{-5} \text{ mbar}$, $t=30\text{s}$).

Silver nanoparticles were prepared by the reduction of silver nitrate. Silver nitrate, gelatin and hydroquinone of analytical grade purity were used as starting materials, without further purification. In a typical experiment, 2 ml of 17% AgNO_3 , 0.2 ml of 0.25% gelatin and 1 ml of 0.001N hydroquinone solutions were added to 30 ml of distilled water. The pH of solution was 9.8. Silver nanoparticles from silver colloid solutions were transferred onto glass substrates modified with the polymer blends by dipping for approximately 10 min. The films were dried for 12 hours at ambient temperature.

The absorption spectra of silver nanoparticles in the solution and in the polymer matrix were measured with a UV-VIS spectrophotometer (AvaSpec-2048, Avantes). The absorption spectrum of isolated spherical particles was characterized by the well-known Mie resonance model [1]. Amount of silver as element in the polymer was obtained with a XRF spectrometer a VRA-20, X-ray source voltage 35 kV and current 26 mA. Registration time was 30 s and the investigated area was 78.5 mm^2 . XRD analysis was performed on the thin films using a diffractometer DRON-3 (Cu $\text{K}\alpha$ radiation). The influence of X-ray irradiation on the silver nanoparticles in polymer matrix was investigated by irradiation with X-ray source (at 35 kV and 26 mA, 300s).

Fig. 1 shows the UV-VIS spectra of Ag nanoparticles in solution and in the different polymer matrix. The main peak observed at 420 nm corresponds to the plasmon surface resonance of Ag nanoparticles. According to calculations done employing Mie's theory, the silver particle diameter was 60 nm. The optical absorbance peak of Ag nanoparticles in polymer matrix is located at 490-500 nm. The simple adsorption of the silver nanoparticles on the polymer from the solution, reached only 30% that of the silver nanoparticles in solution. A red shift in this band to longer wavelengths was observed [3-5].

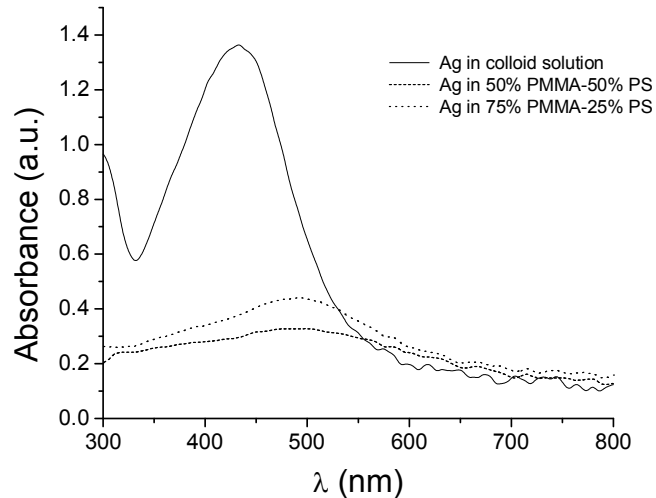


Fig.1. UV-VIS spectra of the silver nanoparticles in solution and in polymer matrix

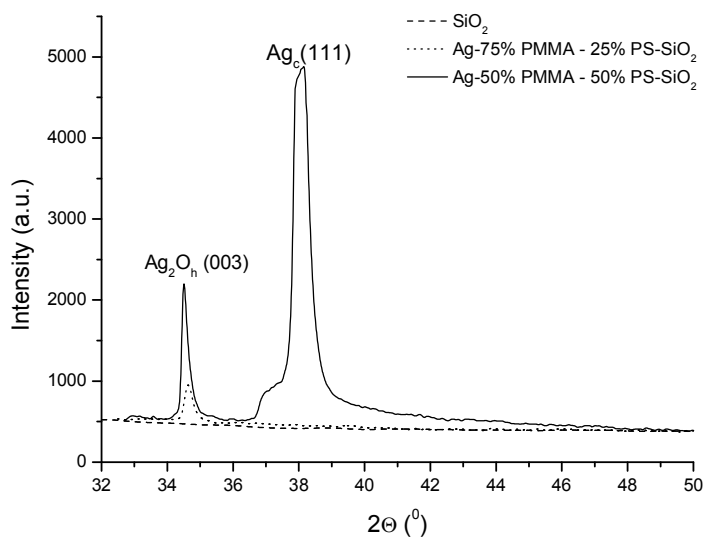


Fig.2. X-ray diffraction pattern of silver nanoparticles in polymer

XRD analysis (Fig.2) showed two characteristic diffraction peaks ($38^{\circ}, 34^{\circ}$). They were the result of crystal faces (111) of cubic silver and (003) of hexagonal silver oxide crystals.

Table 1. Amount of silver in polymer before and after X-ray irradiation

Sample	Amount of silver, µg	
	Before irradiation	After irradiation
Ag on 50 % PMMA - 50% PS	1.46	0.632
Ag on 75 % PMMA - 25% PS	0.99	0.758

Amount of silver before and after X-ray irradiation was investigated by XRF (Table 1). The amount of silver in polymer matrix was dependent on the polymer blends. It varied from 1 to 1.45 µg. After X-ray irradiation the amount of silver decreased by 23 % and 56 %.

Conclusions

A method of silver nanoparticles incorporation in polymer is presented. This method can be applied under normal pressure at room temperature and is relatively simple and fast. This method is considered to be a promising way in preparation of polymer/inorganic nanocomposites for applications in medicine (nanocomposites sensitive to x-ray radiation).

Acknowledgement

The Lithuanian Science and Study Foundation has supported this work.

References

1. Elechiguerra J.L, Burt J.L, Mrones J.R, CAmacho-Bragado A., Gao X., Lara H.H, Yacaman M.J., Interaction of silver nanoparticles with HIV-I. Journal of Nanobiotechnology 2005, 3- 6 p.
2. Safonov V.P., Shalaev V.M., Markel V. A., Danilova Yu. E., Lepeshkin N. N., Kim W., Rautian S. G., and Armstrong R. L., "Spectral Dependence of Selective Photomodification in Fractal Aggregates of Colloidal Particles," Phys. Rev. Lett., 80, 1998. 1102-1105 p.
3. Jin, Y. Cao, C. A. Mirkin, K. L. Kelly, G. C. Schatz, and J. G. Zheng, "Photoinduced Conversion of Silver Nanospheres to Nanoprisms," Science 294, (2001), 1901-1903 p.
4. Jin R. C., Cao Y. C, Hao E., Metraux G. S., Schatz G. C., and Mirkin C.A., "Controlling Anisotropic Particle Growth through Plasmon Excitation," Nature **425**, 2003, p. 487-490.
5. . Karpov S. V., Bas'ko A. L., Popov A. K, Slabko V. V., and. George T. F, "Optics of Nanostructured Fractal Silver Colloids" Chapter in Recent Research Developments in Optics, vol. 2, Research Signpost, Trivandrum, India, 2002, 427-463 p.
6. <http://www.physorg.com/pdf63004522.pdf>
7. X.S Xie, J. Yu, W.Y. Yang WY. Perspective – living cells as test tubes. Science, 5771 2006; **312**, 228-230 p.
8. X. Xu X, R. Patel , "Imaging and Assembly of Nanoparticles in Biological Systems" in Handbook of Nanostructured Biomaterials and Their Applications in Nanobiotechnology, H. S. Nalwa, Ed., American Scientific Publishers, Vol. 1, Chapter 13, , 2005, 435-456 p.
9. www.nsti.org/img/nwn/0606.
10. <http://nano.cancer.gov/>

NEW LINES OF DEVELOPMENT FOR RADIATION THERAPY OF CANCER

Sören Mattsson and Per Nilsson

*Department of Medical Radiation Physics, Malmö University Hospital, SE-205 02 Malmö and
Department of Medical Radiation Physics, Lund University Hospital, SE-221 85 Lund,
Sweden*
soren.mattsson@med.lu.se

Abstract

Radiation therapy is in the process of great advancement. The current improvements in medical imaging are remarkable. The advances in methods of dose delivery (3D conformal, IMRT, protons) are also extraordinary. In the future, biological modeling based on nuclear medicine imaging (PET) is a way to get better understanding of the tumour biology and adapt the treatment to target and normal structure characteristics as they respond to the ongoing therapy. Adaptive radiation therapy offers increased probability of tumour control under reduced or equivalent toxicity. Such adaptations can be based upon biological changes in target signatures (changes in metabolism, hypoxia, perfusion, replication, etc.) or simple alterations in the geometric position/shape of the target and normal structures as the treatment is delivered.

Key words: *radiation, therapy, radiotherapy, patients, IMRT, PET/CT, imaging, conformal, adaptive.*

Introduction

Cancer is one of the leading causes of death in the Baltic countries and the only major disease for which death rate is increasing. The demands for cancer care will increase over the next decade due to the continuous aging of the population. Surgery and radiation therapy are the main treatment methods for curing cancer. It is also of high importance for palliative treatment. In Sweden, every second cancer patient is treated with radiotherapy at some stage during the management of his/her disease. This means that one of five persons will get radiotherapy during lifetime. Radiation therapy currently undergoes dramatic changes and improvements (1, 2). The main goal of radiation therapy is to give a sufficiently high absorbed dose to the target volume while limiting the dose to nearby healthy organs in order to improve control of tumour growth and limit side effects.

Methods of radiation therapy

There are three main methods of radiotherapy: external beam radiotherapy, brachytherapy (sealed source radiotherapy) and systemic or unsealed source radiotherapy. External beam therapy, which totally dominates, uses radiation beams from linear accelerators and still occasionally from ^{60}Co -sources. These devices are mounted on a gantry, which can rotate to allow for many beam directions to be focused on the target volume. Sparing of normal tissue is accomplished in two fundamental ways: 1) Geometric avoidance of normal tissues by directing multiple beams at the target, thus delivering a high dose where the beams intersect at the target, and a relatively lower dose outside the intersection. 2) Biological sparing of normal tissue is accomplished by fractionating the therapy over several weeks, irradiating daily. The tumour tissue often has poorer mechanisms for repairing sublethal DNA damage than normal tissues. Therefore by fractionating the treatment, normal tissues are provided time to repair, thus biologically sparing the normal tissue.

Who is treated and how?

Common malignancies for radiotherapy are prostate cancer, breast cancer, head & neck cancer, tumours in the gastro-intestinal tract, lung cancer or various gynaecological tumours. Today the current workflow begins with fixation of the patient using body moulds and/or head masks. A CT scan is performed of the tumour volume and its surroundings, and the patient is marked for repeated alignment with localisation lasers - to be able to reproduce the position of the body during the whole series of treatments. The CT-images are transferred to the treatment planning computer and tumour and normal tissues are outlined on all relevant CT-images. The results of other diagnostic investigations are also used. On the treatment-planning computer different beam arrangements are tested in order to find an acceptable 3D dose distribution. An important tool in the treatment-planning system is the *beam's eye view* (BEV), which gives the observer a depiction of beam's position in relation to the bony anatomy of the patient and normal organs. Using information from the BEV, blocking of parts of the radiation beam is done in order to spare normal tissue as much as possible. In this way beam geometries, energies and collimation are determined and the resultant dose distribution computed.

The treatments (3-D conformal radiation therapy) are then performed daily for several weeks. During the course of the treatment, different imaging modalities are used to monitor the geometric set-up of the patient to verify constancy in the patient position.

New imaging tools for target and normal structure definition

In the late 1980s and 90s computed tomography (CT) based treatment planning became available due to the increased computer power. Both the imaging capabilities and the ability to compute radiation dose distributions on CT gave the possibility to plan the treatments and visualise the treatment plans in 3D. The CT-technique has improved dramatically and new imaging methods are introduced. PET/CT promises great improvements in finding primary tumours and metastases and to improve accuracy in positioning and outlining active tumour tissue during treatment planning and during follow-up of the treatments. The main tracer up to now has been ¹⁸F-FDG, but new agents are likely to become more available and gaining increasing clinical importance for radiotherapy applications. There are also important advances regarding MR-imaging and ultrasound imaging giving new and improved possibilities to localise tumours as well as nearby organs and to follow the effect of a treatment.

IMRT

There have been many advances in the techniques used to deliver a treatment. Intensity modulated radiotherapy (IMRT) uses an inverse planning strategy that interactively optimises the intensity patterns of each beam to deliver the desired dose distribution defined by an objective function. IMRT allows for each beam to be modulated, enabling dose distribution to carve out the target volume and spare normal tissues in the millimetre range. The development during the last 5 years have improved our possibilities to deliver the radiation to volumes of the body where it is needed and to get better tumour volume coverage and less dose to risk organs than before.

Proton and other particle therapy

With protons and heavier ions, we will increase the possibilities to get better tumour volume coverage and less dose to organs at risk compared to conventional radiotherapy. An advantage with particle beams is that they deliver their maximum dose deep in the body and at depth which can be adjusted with the energy of the particles. This gives much more favourable dose distributions and relations between dose to tumour and normal tissue and will be of special importance for the treatment of children, head&neck tumours, etc. In Sweden, we have now a decision to build a national particle therapy unit jointly owned and driven by all the Swedish university hospitals and located to Uppsala.

Gated and image guided radiation therapy

Respiratory gating is used to counteract the effects of organ motion during radiotherapy for e.g. chest tumors. Image Guided Radiation Therapy (IGRT) machines have a CT scanner integrated with the treatment system (3). The patient can be scanned and the tumour located in 3D space immediately before treatment. The ability to correct for movement and setup errors allows smaller margins to be used, sparing healthy tissue and escalating the tumour dose.

Biological parameters

Together with new imaging technology, treatment technique and types of radiation, new biological information is becoming more and more available. We know that a badly oxygenated part of the tumour needs more radiation to be killed. We can expect that a part of the tumour where the tumour cell density is high needs a higher absorbed dose, etc. New PET-markers may help us to identify regions in the tumour that are resistant to radiation and therefore needs a higher absorbed dose (4). Development in gene technology may give us markers to foresee individual radiosensitivity and an instrument to follow effects of the first treatment(s) in a series, giving a possibility to adjust and adapt the following treatments in the series.

Summary and conclusions

Radiation therapy has up to now mainly been a standardised procedure. We now proceed further towards more individualised radiation therapy, which in a real-time is adapted to the target and normal structure characteristics as they respond to the ongoing therapy. Such adaptations can be based upon biological changes in the target (changes in metabolism, hypoxia, perfusion, replication, etc) or simple alterations in the geometric

position/shape of the target and normal structures as the treatment is delivered. We see around the corner a real renewing of a classical treatment method, which we believe will give a more efficient radiation therapy for a number of diagnoses.

References

1. Bentzen S.M. Radiation therapy: Intensity modulated, image guided, optimized and evidence based. Radiotherapy and oncology 77, 2005, 227-230 p
2. McNutt T., Kaus M.R., Spies L. Advances in external beam radiation therapy. In: Advances in Healthcare Technology (Ed by Spekowius G. and Wendler T.), Springer, 2006, 201-216 p
3. Jaffray D.A., Siewersen J.H., Wong J.W., Martinez A.A. Flat-panel cone-beam computed tomography for image-guided radiation therapy. Int. J. Radiat. Oncol. Biol. Phys. 53, N5, 2002, 1337-1349 p.
4. Rajendran J.G, Hendrickson K.R.G, Spence A.M., Muzy M., Krohn K.A., Mankoff D.A. Hypoxia imaging-directed radiation treatment planning. Eur. J. Nucl. Med. Mol. Imaging, 33, 2006, S44-S53 p

DOSIMETRIC VERIFICATION OF BREATHING ADAPTED RADIOTHERAPY USING POLYMER GEL

Sofie Måansson¹, Anna Karlsson¹, Helen Gustavsson^{1,2},
Johan Christensson³ and Sven Å J Bäck¹

¹Department of Medical Radiation Physics, Lund University, Malmö University Hospital, Sweden (email: sofie.mansson@med.lu.se); ²Siemens Medical Solutions, Stockholm, Sweden; ³Department of Radiotherapy, The Finsen Centre, Rigshospitalet, Copenhagen, Denmark

Abstract

Background: In radiation therapy patient movement caused by respiration can be a major challenge to the ambition to deliver a high-absorbed dose to the target volume while minimizing the dose to healthy tissue. Respiratory gating is a method that allows radiation beam-on only during a pre-specified phase of the respiratory cycle. Depending on the beam-on window, which determines the maximum allowed extent of motion, a dose-smearing effect will appear. Dosimetric verification of gated dose delivery in 1D and 2D has been performed. However, there is no experimental 3D data on the dosimetric benefit of respiratory gating.

Aim: The aim of this study was to investigate the feasibility of using a polymer gel dosimeter for 3D dose verification of breathing adapted radiotherapy.

Methods: A moving gel phantom, simulating respiratory motions of the thorax region, was used. Two identical treatment plans were delivered; one for the un-interrupted beam treatment with the gel phantom in a static position, and one for the gated treatment with a moving gel phantom. Both small and large gating windows were investigated. The measured dose distributions were read out using magnetic resonance imaging.

Result: The dose-smearing effect around field edges for small and large gating windows was compared for the gated and static un-interrupted beam treatment. For the small gating window (2 mm) no smearing effect was detected. For the large gating window (10 mm), however, there was a significant smearing effect.

Conclusion: This study shows that it is feasible to use a 3D gel dosimeter for dose verification of breathing adapted radiotherapy.

Key words: radiotherapy, gel dosimeter, respiratory gating, BART

Introduction

In radiation therapy patient movement caused by respiration can be a major challenge to the ambition to deliver a high absorbed dose to the target volume while minimizing the dose to normal tissues. Large respiratory motion requires increased margins, which implies an increased risk of morbidity from late toxicity. It is therefore important to take respiratory motion into account when treating targets in the thorax region. Studies show that breathing adapted radiotherapy (BART) of breast and lung cancers reduces the dose to organ at risks, without compromising target coverage [1,5]. Respiratory gating is a BART method that allows radiation beam-on only during a certain pre-specified phase of the respiratory cycle. Depending on the length of the duty cycle, however, a certain dose smearing of the field edges due to movement during the beam-on time will remain [2]. Other factors, such as for instance accelerator output stability during switching on and off the beam, may also contribute to the uncertainty of the delivered dose [4]. In previous studies, ionization chambers, film and diode arrays have been used for dosimetric verification of gated dose delivery in 1D or 2D [2,3]. However, there is no experimental 3D data on the dosimetric benefit of respiratory gating. The aim of this study was to investigate the feasibility of using a 3D gel dosimeter for dose verification of breathing adapted radiotherapy.

Methods and materials

In this study a moving gel phantom, simulating small and large respiratory motions of the thorax region, was used. Two identical gel phantoms were irradiated. One was irradiated in a static position, and the other gel was irradiated repeatedly in a specific phase of its motion, representing gated radiotherapy. Since the moving device had both vertical and horizontal motion both a small and a large gating window could be investigated at the same time. The resulting data from the static and dynamic measurements was compared and analyzed. A gated CT-scan of another identical gel phantom was obtained, and the irradiation was reconstructed in a treatment planning system for comparison.

Gel preparation. The gel was prepared under normal levels of oxygen using gelatine (8% w/w swine skin, 300 bloom, Sigma Aldrich), ultra pure deionized water (90% w/w), methacrylic acid (2% w/w, purity grade approx. 99%, Sigma Aldrich) and Tetrakis(hydroxymethyl)-phosphonium (2 mM, techn. 80% in water, Sigma Aldrich). The mixing procedure has been described elsewhere [7]. The gel was poured into 2 cylindrical glass bottles (gel phantom, Ø 10 cm, volume 1.2 l), 12 glass vials (calibration, Ø 1.5 cm, length 6 cm) and 4 test tubes

(depth dose, \varnothing 1.6 cm, length 13 cm). Another identical cylindrical glass bottle, containing only water and gelatine, was used for gated CT scan and dose planning.

Moving gel phantom. To simulate respiratory motion, the gel bottles were mounted on an in-house designed and constructed motion device (figure 1).

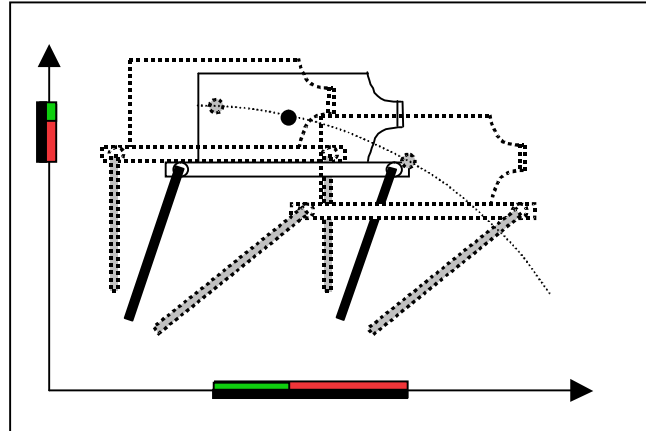


Fig. 1. Black bar indicates motion of the gel phantom, where the green fraction denotes beam-on and the red denotes beam-off. Not to scale.

The cyclic motion of the device had a total vertical motion extent of 7 mm and a total horizontal motion extent of 37 mm. The Varian Real-time Position Management (RPM) system was used to monitor the moving gel phantom, to gate the CT-scanner and to gate the treatment machine. The real-time position of the gel was obtained using an infrared camera system viewing the RPM marker box placed on the moving phantom. The RPM system allowed beam-on only in the pre-specified phase of the phantom motion cycle, which was set around the maximum of the motion extent. The duty cycle was set to 26% and both small (2 mm vertical motion) and large (10 mm horizontal motion) gating windows were investigated (figure 2).

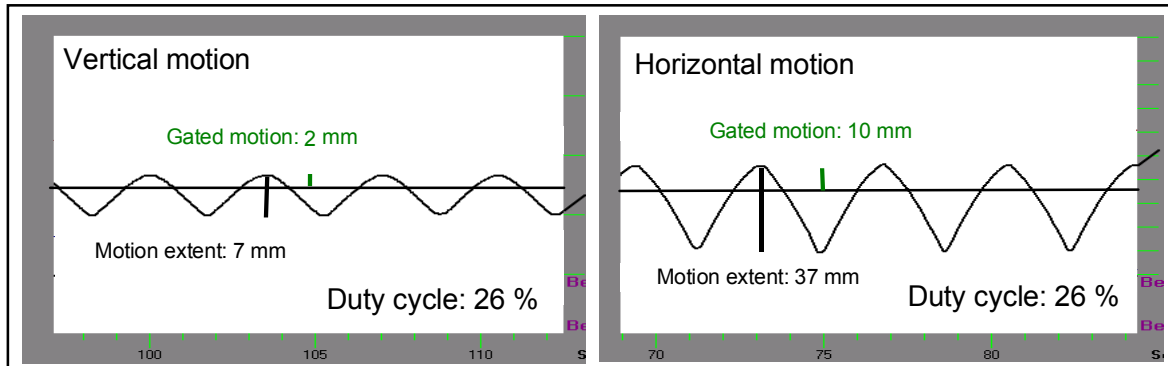


Fig. 2. The Varian RPM system shows the horizontal and vertical motion of the gel phantom. Please note that the scale of the y-axes differs (10 mm/unit in both cases).

Gated treatment planning and gated irradiation. A single slice Siemens CT scanner was used together with the Varian RPM system to acquire images of the moving gel phantom during the phase that represented maximum extension. The dataset was input into the Eclipse treatment planning system (Varian Medical Systems) to plan two 6 MV, $6 \times 6 \text{ cm}^2$ beams with gantry angles 109° and 285° . The linac was set to deliver 600 MU/min. A dose of 2 Gy at the isocentre was chosen to minimize dose rate effects, cf. De Deene *et al* 2006 [8]. Two identical treatment plans were delivered; one for the uninterrupted beam treatment with the gel phantom in a static position, and one for the gated treatment with a moving gel phantom. During irradiation the first gel received 112 MU/beam in one uninterrupted fraction, while the gated treated gel received 10 beam-on segments with 11 MU each, plus one with the remaining 2 MU.

Magnetic resonance imaging and evaluation. Magnetic resonance imaging was carried out using a 1.5 T Siemens Symphony scanner (Siemens Medical Systems, Erlangen, Germany). The images were acquired using a 32-echo multi spin echo sequence with inter-echo spacing equal to 10.6 ms. The repetition time was 4000 ms and the voxel size was $1 \times 1 \times 3 \text{ mm}^3$. In-house developed software was used for image processing [6]. The measured dose profiles were normalized at the isocentre. To focus on the smearing effect the vertical profiles were matched at the beam edges, i.e. at 50% relative dose.

Results and discussion

Dosimetric measurements were undertaken to verify whether gel is a useful dosimeter for dose verification of breathing adapted radiotherapy. The dose-smearing effect around field edges for small and large gating windows was compared for the gated and static uninterrupted beam treatment. For the small gating window (2 mm) no smearing effect was detected (figure 3a). For the large gating window (10 mm), however, there was a significant smearing effect (figure 3b). The static non-gated profiles satisfactorily agreed with the TPS-profiles. A difference between the vertical profiles of the static non-gated and gated data close to the surface of the gel phantom (inset in figure 3a) was not fully understood. The gated and non-gated gels were from the same batch, which suggests that this deviation was not caused by gel malfunction. Output stability and set-up deviations are parameters that could have an effect on the result. However, a study shows that for a 6 MV gated photon beam from a Varian linear accelerator, maximum deviations in output, flatness and symmetry are only a small fraction of the actual measured difference in the resulting data [4]. The differences between the vertical profiles will be further investigated, for example using other detector systems. A more realistic gel phantom, containing for instance a low-density gel insert [9] simulating lung tissue, could also be developed.

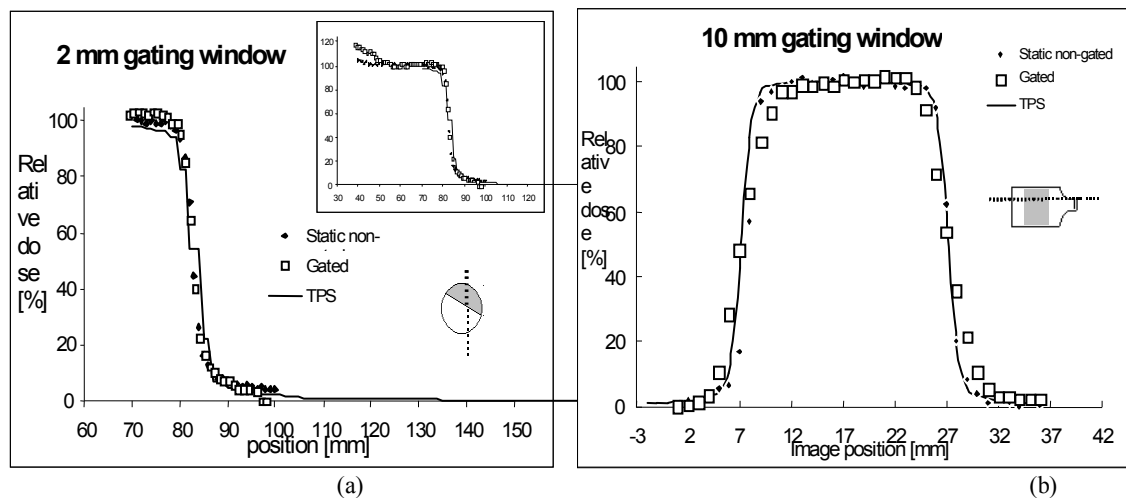


Fig. 3. (a) Vertical dose profiles through iso centre in the isocentre slice. (b) Horizontal dose profiles through the gel phantom at the isocentre.

Conclusion

This study shows that it is feasible to use a 3D gel dosimeter for dose verification of breathing adapted radiotherapy. As long as the gating window can be kept small the smearing effect is negligible according to our measurements.

References

- Korreman S S, Pedersen A N, Nottrup T J, Specht L and Nystrom H 2005 Breathing adapted radiotherapy for breast cancer: Comparison of free breathing gating with the breath-hold technique *Radiother. Oncol.* **76** 311-318
- Li XA, Stepaniak C and Gore E 2006 Technical and dosimetric aspects of respiratory gating using a pressure-sensor motion monitoring system *Med. Phys.* **33** 145-154
- Kubo H D and Hill B C 1996 Respiration gated radiotherapy treatment: a technical study *Phys. Med. Biol.* **41** 83-91
- Ramsey C R, Cordrey I L and Oliver A L 1999 A comparison of beam characteristics for gated and nongated clinical x-ray beams *Med. Phys.* **26** 2086-2091
- De Pooter C, Alberly J, Pittomvils G, Dirix L and Huget P 2004 Real-time position management (RPM) gating in the treatment of NSCLC: effect on tumour (Tu) motion of patient specific target volumes (GTV-PTV) and surrounding normal lung tissue (V20) *Radiother. Oncol.* **73** S453-S454
- Karlsson A, Gustavsson H, Olsson L and Bäck S. A. (2003) Image Processing Software for 3D Dose Evaluation in Gel Dosimetry. *Proceedings of the World Congress on Medical Physics and Biomedical Engineering, Aug 24-29, Sydney, Australia, ISBN 1877040142.*
- Gustavsson H, Bäck S Å J, Medin J, Grusell E and Olsson L E 2004 Linear energy transfer dependence of a normoxic polymer gel dosimeter investigated using proton beam absorbed dose measurements *Phys. Med. Biol.* **49** 3847-3855
- De Deene Y, Vergote K, Claeys C and De Wagter C 2006 The fundamental radiation properties of normoxic polymer gel dosimeters: a comparison between a methacrylic acid based gel and acrylamide based gels *Phys. Med. Biol.* **51** 653-673
- Haraldsson P, Karlsson A, Wieslander E, Gustavsson H and Back S Å J 2006 Dose response evaluation of a low-density normoxic polymer gel dosimeter using MRI *Phys. Med. Biol.* **51** 919-928

IMPLEMENTATION OF PORTAL DOSIMETRY FOR PATIENT RELATED QUALITY CONTROL IN INTENSITY MODULATED RADIOTHERAPY

S. Popov¹, G. Boka¹, A. Miller², Yu. Dekhtyar³

¹Riga Eastern Hospital, Latvian Oncology Center, Riga, Latvia

²Vilnius University Oncology Institute, Vilnius, Lithuania

³Riga Technical University, Riga, Latvia

Abstract

During past decade Intensity Modulated Radiotherapy (IMRT) become widely accepted and used in clinical practice worldwide. At this moment Latvian Oncology Center (LOC) is only hospital in Latvia and Baltic States using IMRT in clinical practice. IMRT in LOC primarily is used for Head and Neck cancer patients, where it is clinically proven to give increased benefit for patients from point of view of both higher tumor control and reduced normal tissue complications. Due to intentionally non-homogeneous fluence distributions of Intensity Modulated (IM) fields it's necessary to perform patient related Quality Assurance of all IMRT plans prior to delivery to the patient. Standard methods employing film and ionometric dosimetry are time consuming and expensive. At present moment we are implementing into daily clinical practice Portal Dosimetry system for patient related QA and routine quality control of IMRT delivery system.

Key words: *Intensity Modulated Radiotherapy, Quality Assurance, Portal Dosimetry*

Introduction

Intensity Modulated Radiotherapy (IMRT) is widely used nowadays for treatment of virtually all tumor localizations. Presently, Latvian Oncology Center (LOC) is only hospital in Latvia and Baltic States using IMRT in clinical practice. IMRT in LOC is used primarily for Head and Neck cancer patients, where it is clinically proven to give increased benefit for patients from point of view of both higher tumor control and reduced normal tissue complications.

Complexity of IMRT plans makes it necessary to perform patient related Quality Assurance of each plan delivered in a Radiotherapy Department. At present moment standard of practice for patient related QA in our center is widely accepted procedure, consisting of verification of fluence matrix of each Intensity Modulated (IM) field by means of film dosimetry and ionometric verification of point dose at the centre of each field in homogeneous PMMA or water phantom. This procedure is labor intensive and expensive because of cost of the films. During this year we had obtained commercial solution for portal dosimetry to be used in conjunction with existing Amorphous Silicon and Liquid Chamber portal imaging detectors.

This work is presenting preliminary results of clinical evaluation of the Varian Portal Dosimetry system, performed in Latvian Oncology Center, in cooperation with Vilnius University Oncology Institute.

Materials and Methods

Portal Dosimetry system commissioning and basic tests, including evaluation of linearity and stability of the Portal Vision aS-500 system in dose acquisition mode, were performed during initial phase of portal dosimetry implementation. System has shown excellent short and long term stability as well as dose linearity, so it was decided to implement part of the routine QA tests of dynamic Multileaf Collimator (dMLC) using mainly Portal Vision system, regularly verified by film dosimetry.

Second phase was designed to evaluate possibility of use of the Portal Dosimetry system for patient related QA in IMRT, particularly for Head and Neck cancer patients.

For 20 IMRT plans we performed patient related tests both by means of portal dosimetry and film/ionometric dosimetry methods. Then comparison of film dosimetry and portal dosimetry results have been performed and absolute dose comparison results provided by Portal Dosimetry algorithm were compared with results of ionometric dosimetry.

Optimization and dose calculation of IMRT plans was performed using Eclipse Treatment Planning System (Varian Medical Systems) with integrated Helios optimization module. Portal dose acquisition was performed with Varian aS-500 imager (image pixel size = 0.8 mm). Portal dose prediction was performed using Portal Dose Prediction algorithm, developed by Van Esch *et al* [1] and commercialized by Varian. This algorithm is using pencil beam convolution to calculate predicted dose at the imager detector plane, employing special kernel which is taking into account absorption and scattering by imager and imager cassette material.

For film dosimetry Kodak X-OMAT V radiotherapy verification films were used, developed in automatic developing machine existing in diagnostic department of LOC. For film calibration and evaluation was used method developed by Childress *et al* [2] and non-commercial DoseLab software [3]. Ionometric dosimetry was done with cylindrical ionization chamber with 0.125 cm³ volume (PTW 31002).

Film dose distributions were evaluated by visual comparison of superimposed isodose curves and by gamma evaluation method [4]. Portal dosimetry results were evaluated by comparison of acquired dose image with dose image predicted by portal dose prediction algorithm of treatment planning system using gamma evaluation method.

Gamma evaluation criteria of 3% for dose and 3 mm for Distance to Agreement (DTA) were used.

Additional processing of acquired portal dose images and film dosimetry results was performed in Wavemetrics IgorPro [5] software using in-house developed procedures.

Results and discussion

At the Figure 1 are shown results of gamma evaluation of doses measured by film dosimetry and calculated by TPS (left image) and of the gamma evaluation of the same field dose acquired by Portal Image aSi-500 system and dose image calculated by Portal Dose Prediction algorithm (right image). In both cases gamma evaluation criteria 3%/3mm was chosen. One can see in general good agreement between measurement and calculation in total, except region linked by arrow on both images, which was detected as by Portal Dosimetry system, as by film dosimetry. This region was investigated and narrow dose spike with local dose difference of less than 5% was found, so plan was accepted to be treated clinically. Central axis deviation between ionometric dosimetry and dose calculated by TPS was well inside acceptance criteria of 3% (-1.5%). High gamma regions on evaluated portal dose of this field were attributed to cassette positioning deviation on this particular gantry angle.

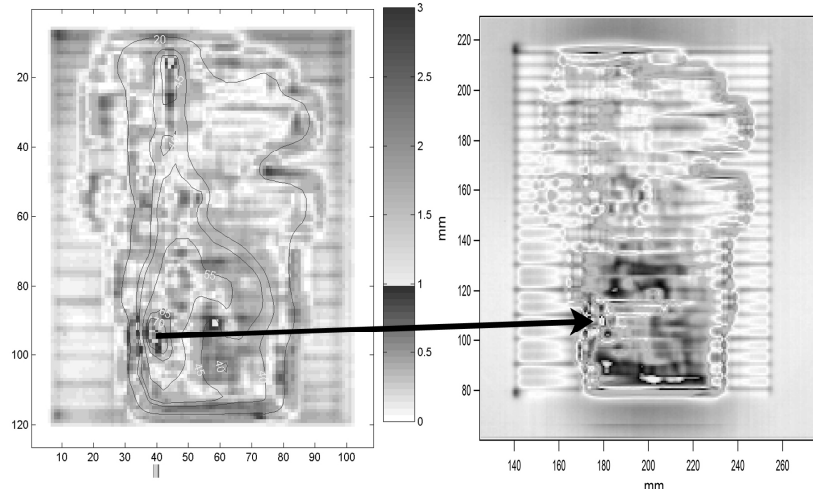


Fig. 1. Gamma evaluation of film dosimetry and TPS calculated dose (left image) and of dose image of the same field, acquired by Portal Image aSi-500 system and Portal Dose Prediction (right image). In both cases gamma evaluation criteria 3%/3mm was chosen. This picture is showing in general good agreement between measurement and calculation in total, except region linked by arrow on both images, which was detected as by Portal Dosimetry system, as by film dosimetry. High gamma regions on evaluated portal dose to be attributed to not corrected properly cassette positioning deviation on this particular gantry angle.

Images of a field heavily affected by tongue and groove effect, demonstrating proper detection by portal dosimetry system of all tongue and groove areas seen on the film are shown at the figure 2. Like in the first case gamma evaluation criteria of 3%/3mm was chosen. Film dosimetry results are at the left, and portal dosimetry results on the right side of the figure. This figure is illustrating good detection of the tongue and groove effect by portal dosimetry system, which is particularly important for heavy modulated fields used for treatment of Head and Neck cancers.

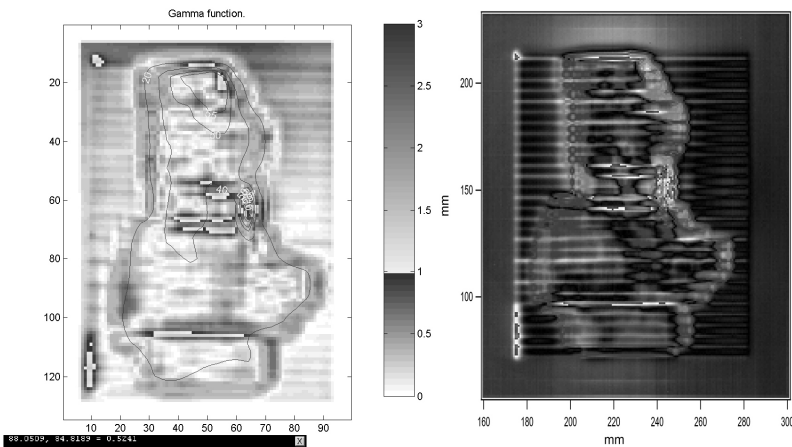


Fig. 2. Images of a field heavy affected by tongue and groove effect, demonstrating proper detection by portal dosimetry system of all tongue and groove areas seen on film dosimetry. Gamma evaluation of film dosimetry and TPS calculated dose (left image) and of dose image of the same field, acquired by Portal Image aSi-500 system and Portal Dose Prediction (right image). In both cases gamma evaluation criteria 3%/3mm was chosen.

Local relative difference between film dosimetry and TPS calculated dose (left image) and between portal dose image of the same field and Portal Dose Prediction (right image) is demonstrated on the Figure 3. One can see that coincidence of the sign and magnitude of these deviations is present in regions with relatively high local dose differences ($>3\%$). This fact can be attributed to limitations of the current Portal Dose Prediction Algorithm, which is shown not to take into account all physical properties of the Portal Imaging system to predict absolute dose, or its surrogate correctly.

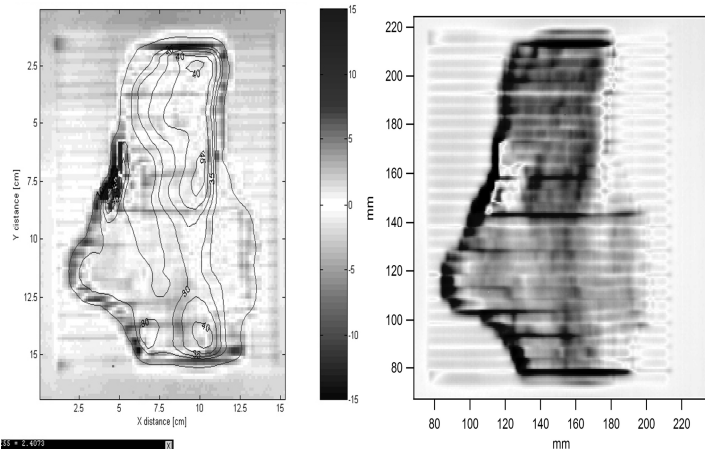


Fig. 3. Local relative difference between film dosimetry and TPS calculated dose (left image) and of dose image of the same field, acquired by Portal Image aSi-500 system and Portal Dose Prediction (right image).

Conclusion

It was demonstrated that Portal Dosimetry system is valuable tool for fluence verification of IM fields, and it can show all clinically relevant deviations between actually delivered fluence and TPS calculated fluence.

It is not possible to use Portal Dosimetry system with currently implemented dose prediction algorithm for comparison of absolute dose distributions due to limitations of the current dose prediction algorithms.

References

1. Van Esch A, Depuydt T, Huyskens DP. The use of an aSi-based EPID for routine absolute dosimetric pre-treatment verification of dynamic IMRT fields. Radiother Oncol. 2004 May;71(2):223-34.
2. Childress NL, Dong L, Rosen II. Rapid radiographic film calibration for IMRT verification using automated MLC fields. Med Phys. 2002 Oct;29(10):2384-90.
3. <http://www.doselab.org>
4. Low DA, Harms WB, Mutic S, Purdy JA. A technique for the quantitative evaluation of dose distributions. Med Phys. 1998 May;25(5):656-61.
5. <http://www.wavemetrics.com>

PRACTICAL ASPECTS OF LINEAR ACCELERATOR X-RAY BEAM COMMISSIONING

Sergey Popov², Albert Miller¹, Darius Norkus¹, Ieva Simutyte¹ and Romas Griskevicius¹

¹Vilnius University Oncology Institute, Vilnius, Lithuania
²Riga Eastern Hospital, Latvian Oncology Center, Riga, Latvia

Abstract

Collection of the linear accelerator X-ray beams dosimetric data, is the critical point in the process of preparation of the machine for clinical use. These data is the basis for radiation dose calculation by planning algorithm within any commercial treatment planning system (TPS). The commissioning process requires qualified and experienced medical physicist with complex knowledge of mathematical algorithm used, treatment techniques intended for use and way of collection accurate, not corrupted, complete and self consistent set of dosimetric data. The examples of commissioning errors and their consequences for clinical dose calculation are presented and discussed here.

Key words: *treatment planning, commissioning*

Introduction

There are several new high energy linear accelerators already installed in the Baltic States Oncology institutions up to date and there are more to come in the near future. Compliance of different technical parameters of linear accelerator with vendor specification is essential. This verification is normally done right after unit installation, during the acceptance testing by local medical physicist and manufacturer representative according the procedure described in vendor documentation. After the acceptance of the new machine and before the clinical use, the number of mechanical and what is most important, dosimetric measurements should be performed to ensure safe and proper use of accelerator. These measurements are main part of commissioning procedure and are used as input data for configuration of treatment planning system dose calculation algorithm. In the user documentation the vendor of TPS also specifies the dosimetric parameters and its format necessary for the input to the TPS. However, it is sole responsibility of the user to ensure comprehensive and accurate collection of dosimetric data and proper configuration of calculation algorithm. Here, full and detailed understanding of calculation algorithm by medical physicist as well as his sufficient experience in absolute and relative dosimetric measurements becomes critical for providing good functionality and accuracy of whole radiotherapy treatment planning process. The errors at this stage can lead to systematic and hardly discoverable by QA activity miscalculations within TPS and consequently can influence clinical outcome. Here is presented and discussed some of possible errors noticed by physicists from Latvian Oncology Center and Vilnius University Oncology Institute in the reports from others Baltic oncology institutions.

Materials and Methods

The number of national and international reports describes the system for QA of treatment planning systems (AAPM TG53 (1), 1998; ESTRO booklet No7, 2003 (2); IAEA TRS430, 2004 (3), etc.). The QA tests described in these recommendations are designed to accuracy of TPS and treatment planning process in general, see pp. 4 through 10 in Fig.1.

Fig. 1. Radiotherapy process.

1. **Diagnosis – staging**
2. **Decision to treat - prescription (treatment protocols)**
3. **Patient Positioning and Immobilization**
 - Establish patient reference marks/patient coordinate system.
4. **Image Acquisition and Input (protocol)**
 - Acquire and input CT, MR, and other imaging information into the planning system.
5. **Anatomy Definition**
 - Define and display contours and surfaces for normal and critical structures.
 - Geometrically register all input data ~CT, MR! including registration with initial simulation contours, films, patient position, etc.
 - Define target contours, generate 3-D target surface using surface expansion, import target information from multiple imaging modalities.
 - Generate electron density representation from CT or from assigned bulk density information.
6. **Beam/Source Technique**
 - Determine beam or source arrangements.
 - Generate beam's-eye-view displays.
 - Design field shape ~blocks, MLC!
 - Determine beam modifiers ~compensators, wedges!
 - Determine beam or source weighting.

7. **Dose Calculations**
- Select dose calculation algorithm and methodology, calculation grid and window, etc.
 - Perform dose calculations.
 - Set relative and absolute dose normalizations.
 - Input the dose prescription.
8. **Plan Evaluation**
- Generate 2-D and 3-D dose displays.
 - Perform visual comparisons.
 - Use DVH analysis.
 - Calculate NTCP/TCP values, and analyze.
 - Use automated optimization tools.
9. **Plan Implementation**
- Align ~register! The real patient with the plan ~often performed at a plan verification simulation!
 - Calculate Monitor Units or implant duration.
 - Generate hardcopy output.
 - Transfer plan into record and verify system.
 - Transfer plan to treatment machine.
10. **Plan Review**
- Perform overall review of all aspects of plan before implementation.
11. **Treatment verification**
- EPID
 - In vivo dosimetry
12. **Treatment delivery**

Most of the tests described in these reports either can not detect errors in input dosimetry data, because designed for verification of calculation and raw dosimetry data agreement, calculations are base upon or reveal combined errors, which is very difficult to trace. The AAPM report does stress attention on the importance of commissioning dosimetry data and appeal for dosimetry data set “self-consistency”. This means, for example, that all of the depth dose curves, axial and sagittal plane profiles, coronal plane profiles and/or 2D dose distributions and any other data, for a particular experiment, are all consistent with each other, and can be combined into one self-consistent dose distribution for that experiment. This can typically be achieved by acquiring a set of relative measurements which are then interrelated by a small subset of either relative or absolute measurements. Recommendations for methods to assure dataset self-consistency are listed in Table 1.

Table 1. Methods for Obtaining a Self-Consistent Dataset

- | |
|----------------------------------------------------------------------------------------------------------------------------------------------------------------------------------------------------------------------------------------------------------------------------------------------------------------------------------------------------------------------------------------------------------------------------------------------------------------------------------------------------------------------------------------------------------------------------------------------------------------------------------------------------------------------------------------------------------------------------------------------------------------------------------------------------------------------------------------------------------------------------------------------------------------------------------------------------------------------------------------------------------------------------------------------------------------------------------------|
| <ul style="list-style-type: none"> • Design the measurements so that the data required to tie all the various separate measurements together are obtained during the same measurement session. • Make measurements over the shortest time span possible consistent with obtaining representative dose measurements. • Use the same equipment and procedures for all similar measurements. • Relate measurements made with different measurement methods to each other. Ideally, some of the measurements should be repeated with an independent, preferably different type, dosimeter. • Use a reference chamber to account for output fluctuations when making measurements with a scanning ionization chamber. • Periodically repeat base measurements, such as the dose at 10 cm depth for a 10x10 cm² field, to monitor the consistency of the machine output and the measuring system. Note that this may involve use of temperature equilibrated water and/or monitoring pressure, in certain situations. |
|----------------------------------------------------------------------------------------------------------------------------------------------------------------------------------------------------------------------------------------------------------------------------------------------------------------------------------------------------------------------------------------------------------------------------------------------------------------------------------------------------------------------------------------------------------------------------------------------------------------------------------------------------------------------------------------------------------------------------------------------------------------------------------------------------------------------------------------------------------------------------------------------------------------------------------------------------------------------------------------------------------------------------------------------------------------------------------------|

In the same AAPM report are also presented the recommended accuracy requirements for dosimetric commissioning data set which are in essence can be summarized as follows: a) absolute dose measurements used for relative measurements normalization – under 1%; b) central axis measurements – below 2%; c) any place inside the useful beam and in the penumbra region measurements – below 3% and d) build up region dose measurements – 20-40% accuracy. These requirements are applied, strictly speaking to TPS based on deterministic or analytic X-rays dose calculation algorithms. Medical physicist should also realize that most likely these numbers will be modified if one considers model algorithms. In these algorithms, to the large extend the beam is mathematically modeled by the physics of X-ray interactions in media and is not “fitted” to the large number of dosimetric measurements like it is in case of deterministic algorithms. The model algorithms do not simulate all physics like first principle algorithm – MC, therefore need “calibration” to the measurement data. Therefore, accuracy requirements to the commissioning data in this case should be tighter. If all measurements are performed according to the rules of self-consistent data set, than there is some assurance in accurate data collection, however authors encourage physicists to verify collected data against data of other institutions, golden beam data and request independent dosimetry audit after commissioning data measurements completion.

Our own experience shows that physicist should expect for the machine of the same model all basic measured beam parameters agreement no more than within 1% with the other institution data or “golden beam” data.

Results and discussion

Case 1: Dynamic wedge commissioning error (based on the original article in a national scientific journal).

The dynamic wedge is realized by continuous movement of one or both collimator jaws, gradually reducing the field size until the collimator is almost completely closed, while the beam is on. The overall wedge field size is defined by the initial collimator setting.

The authors have performed measurements with films in the slab phantom and water phantom with linear array of liquid filled ion chambers to verify calculations of two treatment planning systems – Eclipse (deterministic photon pencil beam algorithm) and TMS/Helax (model convolution-superposition algorithm). The authors observed large discrepancies and therefore requested manufacturers of TPSs to adjust calculations so, the calculation would fit the measurements. As a matter of fact, the TMS vendor was able to do so, Eclipse vendor was not.

The calculation of dose distributions for dynamic wedge fields (Enhanced Dynamic Wedge – EDW), as performed by Eclipse treatment planning systems, is based on measured dosimetry data for open fields, and on Segmented Treatment Tables (STT), provided by Varian. From the manufacturer’s point of view it is not necessary to carry out the complicated measurements necessary to configure EDW fields in treatment planning systems. Before questioning this vendor statement the authors in our opinion should have had the really good reason. First, STT algorithm is very simple and relays on open field data, therefore, if large differences are observed for the wedge between measurement and calculations, than one can expect similar magnitude differences for the open field penumbra region as well, which in essence would mean for deterministic algorithm that the general beam configuration task was not performed right. Basically, this was the reason that vendor could not fit calculations to the wedge data measured at this institution. Second, this algorithm has been tested by manufacturer and than by large number of users worldwide.

The situation with convolution-superposition model algorithm (TMS/Helax) is more complex. The modified field fluence for EDW fields is calculated directly and can be tuned/normalized to the measured data independently from open field data. Authors of the misleading measurements would have had to consider the fact that both TPS with different algorithms and different datasets used for input, give the same calculated profiles for EDW.

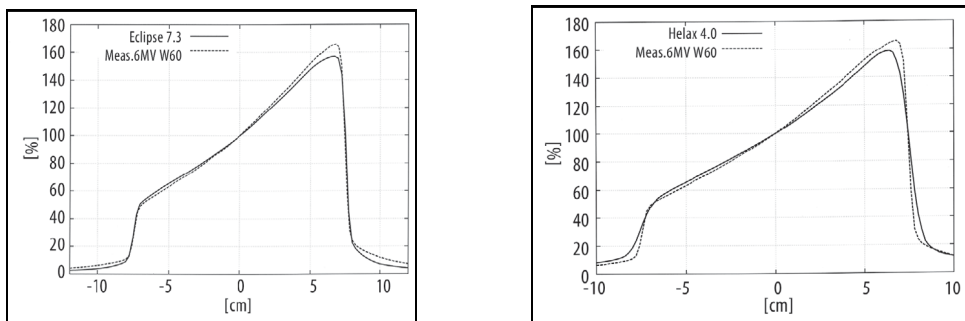


Fig. 2. A measured off -axis dose profile against a calculated one using Eclipse 7.3 and Helax 4.0 TPS for EDW60 and X-6MV beam for a field size of 15×15cm at a depth of 10cm

Reading description of measurements with ionization chambers array and with films performed by authors as well as looking at these graphs is impossible to point out the source of discrepancies. Authors did not present the details of film calibration, correction and comparison of the result of two types of measurements. The films measurements are very tricky, because non linear dose and dose rate dependencies. Delivering EDW60 the dose rate at thin edge of wedge is 600 MU/min, dose gradient at this area is very steep; at thick edge of wedge the collimator moves slowly, dose rate goes down to 100 MU/min and dose gradient is not that large in this area. Therefore, response of either X-Omat V or EDR2 films is complex and is difficult to make accurate conversion to dose. The measurements with LA-48, especially in the penumbra or high dose gradient regions are also problematic because of poor spatial resolution and dose rate dependence of liquid filled chambers. In addition, apparently the measurement normalization was based on reading of 0.6 cc Farmer ionization chamber positioned at the beam central axis. Even for the large wedged fields the dose gradient across the large chamber volume if measuring EDW60 is sufficient to introduce additional error. Whole measurement data set presented by authors is in error, which is clearly seen from the shape of dose profile measured for 5x5 field and 10 degree EDW (Fig.3)

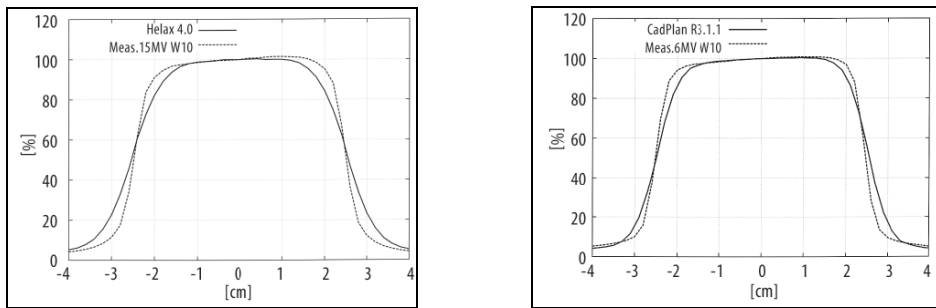


Fig. 3. A measured off -axis dose profile against a calculated one using Eclipse 7.3 and Helax 4.0 TPS for EDW10 and X-6MV beam for a field size of $15 \times 15\text{cm}$ at a depth of 10cm

A physicist at least should visually compare this profile with open field of similar size profile measured by small volume ionization chamber.

Consequences of this error can be noticed clinically. The smaller wedge can be chosen for treatment instead of right one.

Case 2: Measurement of percent depth dose (PDD) for medium small photon fields by compensated photon diode with improper manufacturing quality.

At one point during commissioning of a dual high energy linear accelerator was decided to measure PDDs of small fields for both photon energies with energy compensated photon diode. Diode was verified for both photon energies against ionization chamber according to manufacturer procedures in field $10 \times 10\text{ cm}^2$. During subsequent verification of data it appeared that diode response for fields 3×3 and $4 \times 4\text{ cm}^2$ was not adequate for 15 MV photon beam.

In the figure 4 are shown PDDs for field $4 \times 4\text{ cm}^2$ for photon energies 6 and 15 MV. One can see large energy dependence of diode for 15 MV, which almost not detectable for 6 MV beam.

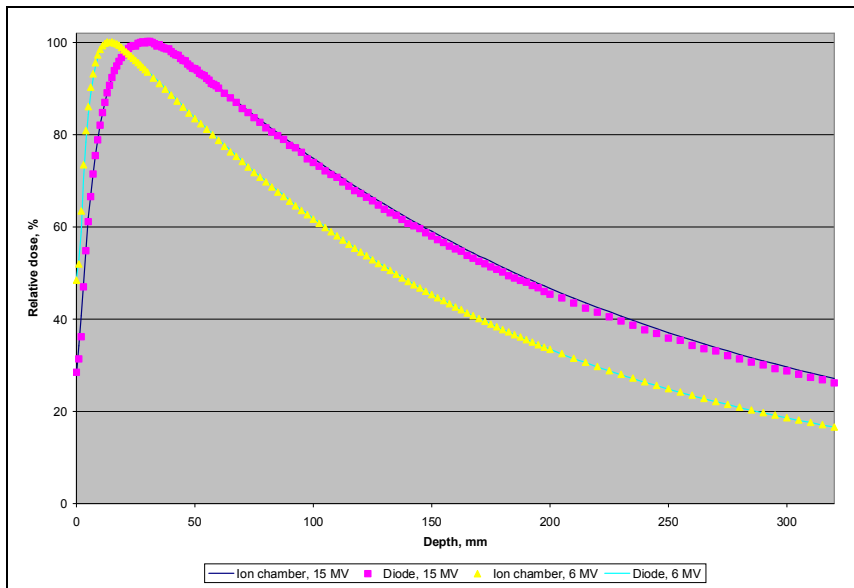


Figure 4. PDDs for field $4 \times 4\text{ cm}^2$ for photon energies 6 and 15 MV.

Measurements were repeated, and ionization chamber measurements where taken as input data for TPS. Later it was found that this particular diode without corrections can be used only for profile measurements. This is typical example of misleading instructions, provided by manufacturer of the equipment, demonstrating role of experience of medical physicist in commissioning process.

Conclusion

Dosimetry part of commissioning procedure is very complex and requires sufficient knowledge and experience in all aspects of medical dosimetry and treatment planning algorithms configuration. The TPS manufacturer is responsible for the adequate calculation algorithm performance, but has no responsibility and no impact on the beam data self-consistency and accuracy used by algorithm. Some errors in the dosimetric data set

collection will have serious influence on clinical outcome, but can be overlooked even within good routine QA program. Authors of this paper recommend for the dosimetric commissioning and consequent configuration of TPS some or all of the following:

1. Invite a qualified expert in high energy X-ray commissioning for consultations and participation in data collection process;
2. Follow the rules of obtaining self-consistent data set;
3. Verify results of measurements against data collected at other institutions and/or “golden beam” data.

References

1. B. Fraass, et.al; American Association of Physicists in Medicine. Radiation Therapy Committee Task Group 53: Quality assurance for clinical radiotherapy treatment planning. Med. Phys. 25 .10., October 1998
2. Ben Mijnheer, et al; Quality Assurance of treatment planning systems. Practical examples for non-IMRT photon beams ESTRO 2004.
3. Commissioning and Quality Assurance of computerized planning systems for radiation treatment of cancer; IAEA, TRS430, 2004

NUMERICAL MODELING OF IONIZING RADIATION INTERACTION PROCESSES IN SEPARATE CELL

R. Plukienė, A. Plukis, Š. Vaitekonis

Institute of Physics, Savanoriu 231, Vilnius, LT-02300, Lithuania
rita@ar.fi.lt

Abstract

The single cell irradiation using tandem ion accelerator is previewed for microdosimetry purposes in the yeast cells. Also individual cells can be targeted within a population to obtain the new *in vivo* data concerning bystander effect. The detail modeling shows that 2.5 MeV proton beam energy deposition is distributed in ~200 μm cell monolayer region and that additional focusing system is needed for single cell irradiation. The method for calculation of the microbeam proton doses deposited in the separate cells is prepared for dose rate prediction in 1-2.5 MeV proton and 3.5-3.7 MeV He²⁺ ion energy range.

Key words: proton/ion irradiation, Monte Carlo modeling, Bystander effect.

In recent years the observation of bystander responses has provoked much debate worldwide. The fact they are observed at low dose has suggested that they may be important in carcinogenesis and radiation risk and may call into question the linear non-threshold model currently used for extrapolating risk from high dose to low dose [1]. Further research is required to confirm/deny whether this may be the case. Recently bystander effects were detected in the unicellular eukaryote, the fission yeast *Schizosaccharomyces pombe* [2].

One of the applicability of tandem ion accelerator “Tandetron 4110A” is the mutant *Saccharomyces cerevisiae* yeast strains cells irradiation [3] for microdosimetry and bystander effect in yeast population experiments. The yeast cells immobilized on self-assembled monolayer further can be exposed to charged particles targeted to regions (patterned arrays) of individual cells to look for mechanisms of response.

In the tandem ion accelerator depending on the initial ion type the maximal achievable energy for H⁺ – 2.5 MeV, He²⁺ – 3.75 MeV, and for heavy ions (C, Fe, Sn or etc.) Z⁺³ – 5 MeV, Z⁺⁴ – 6.25 MeV. It is possible to focus the ion beam into 1 mm diameter spot of 10 pA -100 nA beam intensity. The modeling of 2.5 MeV energy proton beam optimization for selective cell irradiation is performed. The method for calculation of the microbeam proton doses deposited in the separate cells is prepared for dose rate prediction in 1-2.5 MeV protons and 3.5-3.7 MeV He²⁺ ion energy range. All calculations of proton energy distribution and radiation dose are modeled using Monte Carlo code MCNPX.

Proton beam optimization for cell layer irradiation

The simplified scheme of yeast cell monolayer irradiation with 1-2.5MeV proton and 3.5-3.7MeV He²⁺ ion beam is presented in Fig.1. The proton/ion beam reaches biological target through the iron window, which thickness is 4 μm and 4 μm of diameter. The air gap between the iron window and cells is 2 mm. The proton beam spread and intensity reduction in the air gap in front of yeast cell monolayer is presented in Fig. 2a. 2.5 MeV proton flux intensity is reduced by three orders of magnitude starting from the backward surface of the iron window. Resulting proton energy distribution in the cell monolayer is shown in Fig. 2b. The largest part of the protons are in the 2 - 2.2 MeV energy interval.

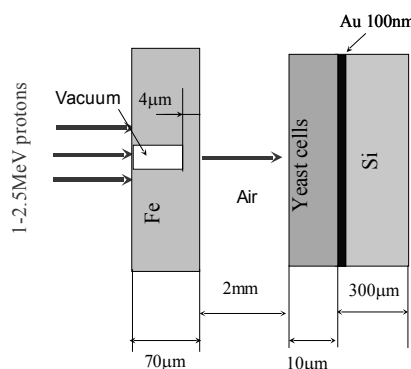


Fig. 1. Simplified scheme of yeast cell monolayer irradiation with proton beam.

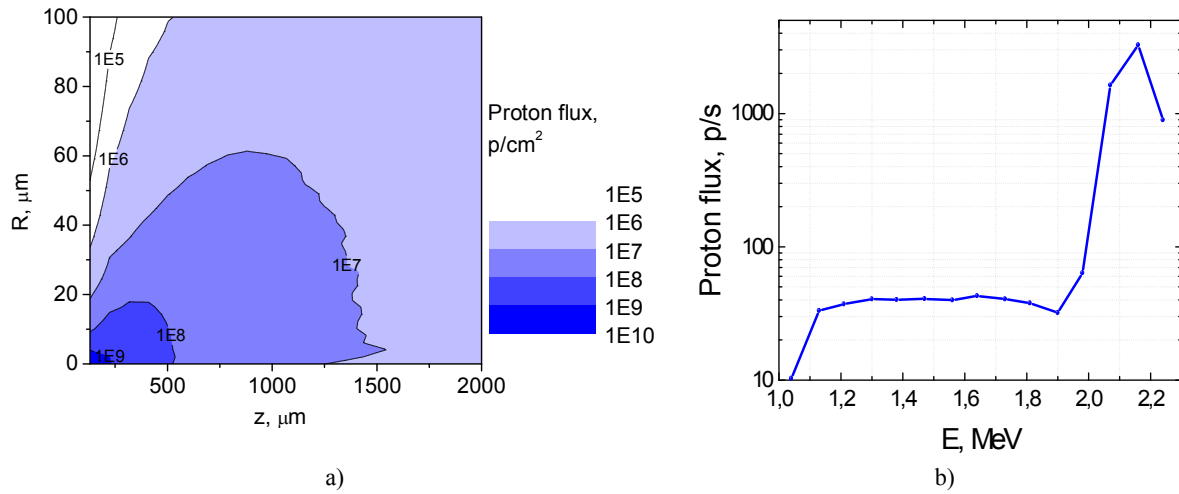


Fig. 2. a) The proton beam spread and intensity reduction in the air gap in front of yeast cell monolayer without collimation; b) proton energy distribution in the cell monolayer.

The 2.5 MeV proton energy deposition in the 10 μm cell monolayer is presented in Fig. 3a-b. Modeling shows that maximal proton beam energy deposition is distributed in $\sim 200\mu\text{m}$ cell monolayer region and that additional focusing system is needed for single cell and selective cell parts irradiation.

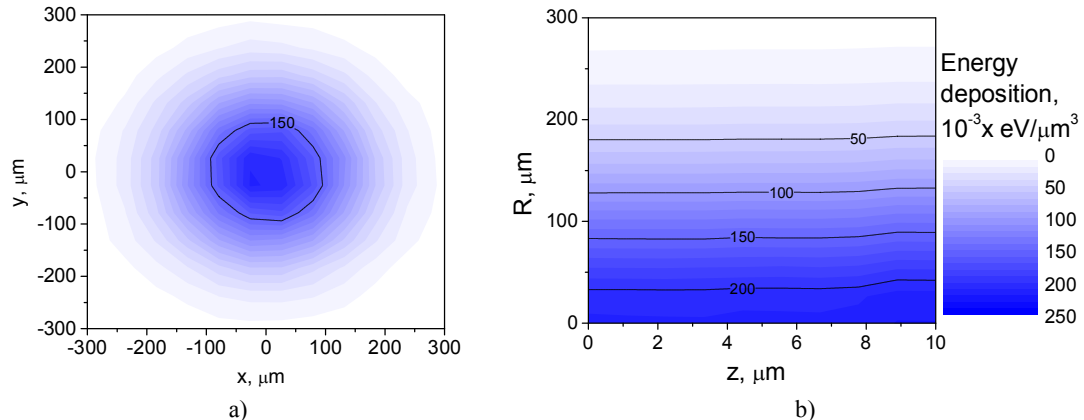


Fig. 3. Modeling of the 2.5 MeV proton energy deposition on the cell monolayer without collimation: a) energy deposition on the cell monolayer surface perpendicular to the proton beam; b) energy deposition along the 10 μm cell monolayer.

As an additional collimator the Ta disc of 100 μm thicknesses and 2 μm pinhole was modeled in front of Fe window. 1-2.5 MeV proton and 3.5-3.7 MeV He^{2+} ion beam irradiation of cells monolayer was evaluated with micrometer precision. The cross sectional view of energy deposition in cell monolayer irradiated with 2.5 MeV protons and 3.7 MeV He^{2+} ion beam is presented in Fig. 4. One can observe that in case of proton irradiation the maximal deposited energy is distributed in 10 μm region, which corresponds to yeast cell dimensions. He^{2+} ion irradiation is more dispersed compared with protons. Unlike in the proton irradiation case the 3.7 MeV He^{2+} ions Bragg peak is at the 6th μm of cell monolayer (yeast cell nucleus region) and therefore the possibility of different cell parts irradiation appears by changing ion energy and collimator pinhole position.

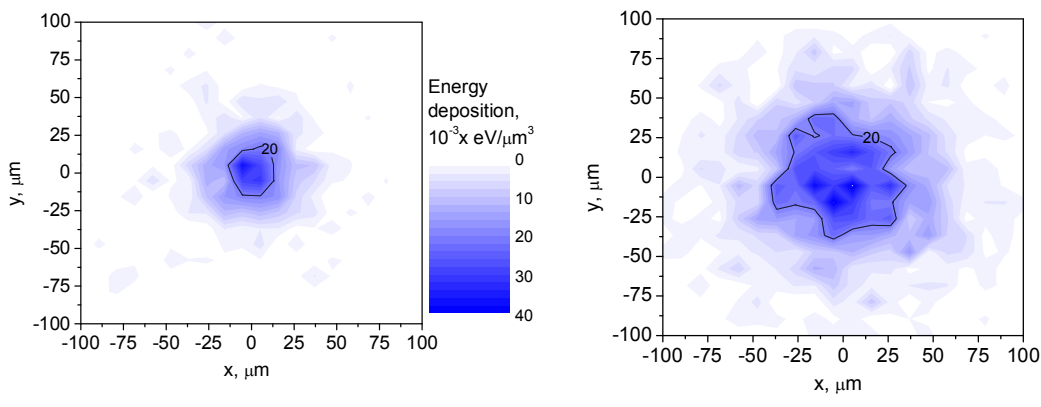


Fig. 4. Modeling of a) 2.5MeV proton and b) 3.7MeV He^{2+} ion beam energy deposition on the cell monolayer surface using collimator.

Microbeam proton/ion doses prediction for yeast cells

Single cell irradiation with exact number of charged particles down to one particle per cell can be achieved using accelerator-based microbeam technique. The calculation of the microbeam proton doses deposited in the yeast cells is performed for dose rate prediction in 1-2.5 MeV proton and 3.5-3.7 MeV He^{2+} ion energy range. The calculation results are shown in Table 1.

Table 1. The proton/ion microbeam parameters and calculation results of dose deposition in the yeast cell.

Proton energy, MeV	I, pA (particle/cell)	Energy deposition, MeV/g/s	Dose rate, mGy/s
2.5	65	2.44E+08	39.1
2	116	2.88E+08	46.2
1	888	4.23E+08	67.8
He ²⁺ ion energy, MeV			
3.7	531	1.48E+09	236.6
3.5	656	1.20E+09	192.5

In the second column of Tab.1 the proton/ion microbeam parameters are defined in order to obtain one particle per yeast cell. Deposited dose rate was recalculated from proton/ion energy deposition in MeV/g (units used in MCNPX code) for corresponding beam current. We should note that the obtained beam current (hundreds of pA) is exactly in the optimal current range for tandem ion accelerator “Tandetron 4110A”.

Acknowledgements

This research was supported by the Lithuanian State Science and Studies Foundation (No. V-58/V-06077) within frame of European Concerted Research Action COSTP9.

References

1. K.M. Prise, M. Folkard, et. al. (2006) What role for DNA damage and repair in the bystander response? Mutation Research/Fundamental and Molecular Mechanisms of Mutagenesis, Vol. 597, Issues 1-2, pp. 1-4.
2. L.C. DeVeaux, L.S. Durtschi, J.G. Case and D.P. Wells (2006) Bystander effects in unicellular organisms, Mutation Research/Fundamental and Molecular Mechanisms of Mutagenesis, Vol. 597, Issues 1-2, pp. 78-86.
3. Remeikyte B., Plukiene R. et al. (2004) Yeast *Saccharomyces cerevisiae* response to UV and Gamma Irradiation, Environmental and Chemical Physics, Vol. 26, No 4, pp. 148-156.

RELATIONSHIP BETWEEN INTENSITY OF CONTINUOUS-SPECTRUM SOFT X-RAY RADIATION AND MEASURED DOSE

R. Purlys¹, Z. Norgėla¹, A. Poškus¹, R. Rinkūnas¹,
A. Baltušnikas², V. Atkočius³,

B. Gricienė⁴, A. Urbonienė⁴, V. Leščiauskas⁴, Žiliukas⁴

¹Faculty of Physics, Vilnius University, Saulėtekio 9, LT-10222 Vilnius, Lithuania

e-mail: Romaldas.Purlys@ff.vu.lt

²Lithuanian Energy Institute, Breslaujos 3, LT-44403 Kaunas

³Institute of Oncology, Vilnius University, Santoriškių 1, LT-08660 Vilnius

⁴Radiation Protection Centre, Kalvarijų 153, LT-09221 Vilnius

It is shown that continuous-spectrum intensity of an X-ray tube with W anode and the square root of corresponding dose are linearly dependent on anode voltage in the range 10 ÷ 30 kV. In the absence of this linear relationship, applicability of a device for measuring X-ray and γ radiation is questionable. Hence, the results obtained with such a device are not reliable. With increasing excitation voltage, a significant decrease of measured X-ray radiation dose can be observed, causing a deviation from the mentioned linear dependence. Thus, it is necessary to evaluate reliability of a device based on correspondence between measurement results and the known laws of physics.

X-ray radiation is harmful for living matter. During exposure of a material, X-ray radiation can cause various physical processes, creating mobile particles in the crystal (electrons, vacancies, ions) and causing local structure changes (interstitial atoms, structure phase changes) and other defects. In order to predict biological effects of exposure and while planning action of X-ray radiation on a sample material in the bulk or on the surface, it is important to be able to estimate it without lengthy dosimetric measurements requiring additional equipment. Applications of ionizing radiation in medicine, scientific research and industry require reliable estimates of absorbed dose in various objects. The range of applicability of those estimates may be determined on the basis of the shape of the dependence of the square root of the dose ($D^{1/2}$) on anode voltage (U_a): $D^{1/2} = f(U_a)$. Since dose estimation methods are complicated, it is worthwhile to use the known physical regularities for calibrating operation mode of an X-ray tube with a particular anode material and thus make it possible to select exposure time, anode voltage and anode current (I_a) needed for attaining a particular dose rate.

It is known that intensity of continuous-spectrum radiation is proportional to squared anode voltage [1]:

$$I = \text{const } I_a Z U_a^2, \quad (1)$$

where I is the measured intensity and Z is the atomic number of the anode element. It is also known that dependence of X-ray photon emission flux on photon energy in the region of soft X-ray radiation (up to 30 kV) is insignificant or weak [2]. Therefore, in this region dependence of the square root of dose rate of radiation emitted from the X-ray tube window on U_a should be also linear up to the voltage corresponding to excitation of K_α doublet lines of characteristic radiation spectrum:

$$D \sim I = \text{const } I_a Z U_a^2. \quad (2)$$

As we showed earlier [3], the linear dependence $D^{1/2} = f(U_a)$ holds in the continuous-spectrum region of soft X-ray radiation for tubes with W, Ag and Mo anodes. Dependence of characteristic radiation intensity on U_a is the following:

$$I \sim (U_a - U_k)^n, \quad (3)$$

where U_k is the excitation potential of the K line of the spectrum [3], and $n < 2$. Therefore, after exciting the K-electrons, the shape of total intensity dependence changes. The voltage needed for exciting the K_α spectral line becomes larger than the ratio of photon energy and elementary charge, due to the work function of the K-electron. This work function increases with atomic number [1]. This causes an increase of the deviation of K_α photon energy from the continuous-spectrum photon energy at the same anode voltage. When $U_a > U_k$, an increase of contribution of K_α photons to the total intensity of radiation emitted by the X-ray tube causes an increase of the fraction of low-energy photons in the total photon flux, hence the dose has to decrease at some values of anode voltage, i.e., the deviation from the linear dependence (1) has to grow. Therefore, evaluation of dosimeter reliability based on testing the dependence $(D^{1/2}) = f(U_a)$ is most conveniently done using X-ray tubes with W anode.

We investigated dependence of dose rate on U_a in the range 10 ÷ 30 kV for an X-ray tube with W anode. The doses were measured with _____ and LiF dosimeters by putting them next to an opening with diameter 10^{-3} m

in the lead shield near the X-ray tube window in the X-ray diffractometers DPON-3M and ADP-2. Measurements were done 3 to 5 times, measurement duration was varied from 200 s at $U_a=10\text{ kV}$ to 10s at $U_a=30\text{ kV}$, with anode current always equal to 5 mA. The result of each measurement was the mean dose.

The linear voltage dependence of the square root of dose rate, measured with personal LiF dosimeters, was observed in almost entire investigated range of anode voltage (Fig. 1). It must be noted that a 10⁻³ m-thick LiF crystal pellet absorbs 99% of 10 keV photons, but it absorbs only 23% of 26 keV photons. Thus, as U_a increases, the fraction of weakly absorbed high-energy quanta in the radiation flux increases, their absorption in the LiF crystal pellet weakens, and dependence $D^{1/2}=f(U_a)$ becomes nonlinear. In the case of the investigated dosimeter, the linearity region is 10-14 kV (Fig. 2). It should be noted that operation of this type of dosimeter is based on measuring the current caused by charge carriers created due to ionizing effect in the air between the electrodes. Absorption of X-ray radiation in the air is weaker than in LiF pellets. Therefore, at smaller U_a values, a larger fraction of X-ray radiation passes without absorption, and deviation from the linear dependence $D^{1/2}=f(U_a)$ appears earlier. Therefore, the fact that dose values measured with a dosimeter do not conform to this linear dependence means that results of the measurements are not reliable. Evidently, a significant increase of thickness of LiF tablets used in dosimeters would be desirable, in order to extend the linear part of the dependence $D^{1/2}=f(U_a)$ into the region of larger anode voltages. In the case of dosimeters based on dependence of air ionization on ionizing radiation intensity, it seems worthwhile to introduce an additional factor, which depends on radiation quantum energy.

In the case of X-ray tubes with W, Ag and Mo anodes, which are characterized by linearity of the dependence $D^{1/2}=f(U_a)$, and in the absence of characteristic radiation, it is possible to use measurement results obtained with one tube for predicting dependence of square root of X-ray radiation dose rate on anode voltage for other X-ray tubes of the same type, but with other anode materials.

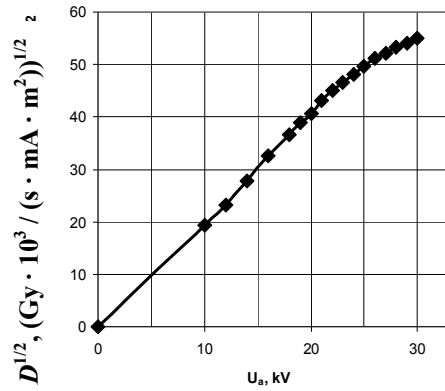


Fig. 1. Dependence of the square root of dose rate on anode voltage for an X-ray tube with W anode, measured with LiF dosimeters.

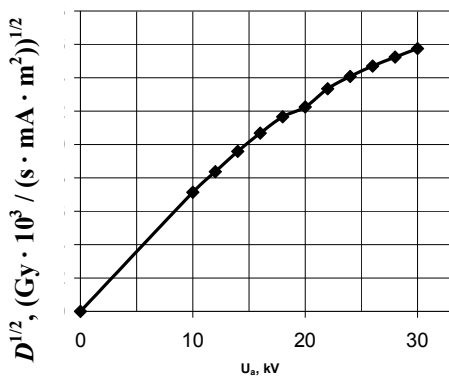


Fig. 2. Dependence of the square root of dose rate on anode voltage for an X-ray tube with W anode, measured with the electrometer EXCALIBUR CDX-200A.

References

1. Kovba L.M., Trunov V. K. Rentgenofazovii analiz. M., 1976, 232p.
2. Krongauz A.N., Liapidevskii V.K., Frolova A.V. Fizičeskie osnovi kliničeskoi dozimetrii. M., 1969, 160p.
3. Purlys R., Norgėla Ž., Baltušnikas A., Atkočius A., Gricienė B., Urbonavičienė A., Leščiauskas V., Žiliukas. Influence of characteristic part of K_α spectrum on the soft X-ray radiation dose. Pr. and mat. Int. Conf. "Radiation interaction with material and Its use in technologies 2006", Kaunas, 28-30 september, 2006, p. 82-84.
4. Vasilev V.N., Lebedev L.A., Sidorin V. P., Stavickii R.V. Spektri izlucheniya rentgenovskikh ustavovok. M., 1990, 143p.

PATIENT'S DOSE ASSESSMENT IN COMPUTED TOMOGRAPHY

Skirmantė Mockevičienė, Diana Adlienė

*Physics Department of Kaunas University of Technology, Studentų g.50, LT-51368 Kaunas, Lithuania
e-mail: skirmante.vardauskaitė@stud.ktu.lt*

Abstract

Dosimetry methods used for the calculation patient's doses during computed tomography (CT) examinations are discussed in this paper with the aim to define the uncertainties caused by these methods. According to the results of the performed dose calculations for the patients undergoing head CT examinations it is shown that the estimated dose values are not optimal and need corrections. Possibility to optimize the procedure based on dose recalculation for the actually exposed volume is discussed.

Key words: *computed tomography, effective dose, dosimetry.*

Introduction

Computed tomography becomes the major source of population exposure to diagnostic X-rays. Patient dose in CT is usually expressed of organ dose and effective dose, which is used as a measure of the stochastic risk. Finding of the reasonable compromise between the acceptable medical image and low dose to the patient is the main problem which has to be solved during X-ray examinations of the patients. Due to this reason the aim of this work was to overview commonly used methods for the assessment of patient doses during CT examinations, to recalculate the doses derived from the calculations, proposed by the application of these methods and taking into account the actually exposed volume and to investigate the possibility of dose optimization based on exposed volume corrections.

Overview of common dose assessment methods

There are at least three commonly used methods for the dose assessment in computed tomography:

- CTDI method using QA phantoms, also known as the standard method (FDA);
- Monte Carlo approach using mathematical and tomographic phantoms;
- Direct approach using anthropomorphic physical phantom.

The first approach is the standard method based on FDA definition of computed tomography dose index (CTDI). This method is normally used for quality assurance (QA) measurements and does not provide a direct assessment of the risk to the patient resulting from CT examinations. The effective dose is estimated from the values of dose-length product (DLP) for an examination, using appropriately normalized coefficients [3]:

$$E = E_{DLP} \cdot DLP, \quad (1)$$

where E_{DLP} is region specific normalized effective dose and DLP is defined in the equation:

$$DLP \sum_i^n CTDI_w \cdot T \cdot I \cdot t, \quad (2)$$

where T is the nominal irradiated slice thickness, I is the tube current, t is the total acquisition time for the sequence and $_nCTDI_w$ is normalized weighted computed tomography dose index.

In the second approach, Monte Carlo computer technique combined with the measurements of free in air values of CTDI is used. Monte Carlo computer techniques are used to simulate the absorption and scattering of X-ray photons within a mathematical anthropomorphic phantom. This gives organ doses normalized to the free in air dose on the axis of rotation of the scanner, from which effective dose could be derived. Radiation transport is calculated using Monte Carlo codes following individual photon histories. The parameters influencing in actual course the radiation transport are selected randomly from their probability distributions for each single particle history [2, 6].

Organ doses are evaluated by summing in each organ and tissue all energy depositions from primary and scattered photons and dividing by the organ mass. This results in the average absorbed dose in the organ regardless of irradiated fraction. Calculated organ equivalent dose values are rather in the form of conversion coefficients, i.e., normalized to another physical quantity. Normalization quantities are easy to measure (i.e. air kerma, entrance surface dose or dose area product.). To derive actual organ equivalent doses, conversion coefficients have to be multiplied by the measured values of normalization quantity for the situation under consideration [8]:

$$D_{organ} = C_{calc} \cdot D_{measured}, \quad (3)$$

where D_{organ} is the organ equivalent dose, C_{calc} - is the calculated organ dose conversion coefficient and $D_{measured}$ is the measured value of the normalization quantity.

Calculated organ doses are only valid for exposure situations similar to those simulated with respect to irradiation geometry, patient size and radiation quality. Small deviation in field size and location may introduce deviations in organ dose, especially in small organs located at the edge of the field. Human anatomy deviates from patient to patient. The mathematical models, with their schematic organ representation, cannot describe any real patient in detail but rather to represent whole populations. Tomographic models are constructed from CT data of the real persons which might deviate significantly from reference data. The shape of each organ is more realistic than for the mathematical models in this case, although, being reconstructed from a specific individual, it might not be representative large populations [8, 9].

Finally, in the direct approach an anthropomorphic physical phantom is used. Doses are measured in the location of organs or tissue of interest by using thermoluminescent dosimeters (TLD) or photodiode system. The measurements of organ doses are carried out by TLD's implanted in tissue and organ positions within an anthropomorphic phantom consisting of tissue equivalent materials. In recent years a metal-oxide-semiconductor field effect transistor (MOFSET) dosimeter was devised as an alternative to TLD [7]. Evaluation formula for the effective dose of the patient is given by ICRP Publication 60 [11] in the expression:

$$E = \sum_T w_T \cdot H_T, \quad (4)$$

w_T is the tissue weighting factor recommended by ICRP Publication 60 and H_T is the equivalent dose of each organ dose multiplied by the radiation weighting factor of these organ.

All discussed dose assessment methods have their own limits, however are applicable for the general evaluation of effective dose to the patient undergoing CT examination. To overcome the existing shortness of the discussed methods the optimization procedure should be initiated.

Instruments and methods

CTDI dose assessment method was chosen for the optimization of the evaluated effective doses to patients during head and neck CT examinations of patients. Dose measurements were performed using pencil shaped ionization chamber and dosimeter (UNFORS Mult-O-Meter 603) during exposure of the cylindrical PMMA head phantom (Cardinal Health Model 76-414-4150) from CT scanner Asteion VF (Toshiba, Japan. 2000) according the standard procedure for the evaluation of CTDI.

Effective dose to patients undergoing the head CT scanning is usually calculated using equation [1, 4, 5, 10]:

$$E = \frac{n CTDI_{w,H,ref}}{P_H} \cdot k_{OB} \cdot \left(\frac{U}{U_{ref}} \right)^{2.5} \cdot C \cdot \frac{1}{p} \cdot L \cdot f_{mean,st} \cdot k_{CT}, \quad (5)$$

where $n CTDI_{w,H,ref}$ is normalized weighted CTDI reference value, k_{OB} is factor, correcting for differences in slice collimation and responsible for overbeam effects, P_H is a quantity determined for the standard head CT dosimetry phantom, U , U_{ref} are scan and reference voltage values, respectively, C is the exposure, p is pitch, L is a scan length, $f_{mean,st}$ is the standard conversion factor, k_{CT} is a correction factor taking into account differences in scanner geometry, beam filtration and the effect of beam-shaping filters. Estimated dose values were recalculated with the reference to the actually exposed volume of the patients head using the effective diameter of the patient's skull and calculated from the real anterior - posterior and lateral CT images.

Results and discussions

The main results of calculations are presented in Table 1. V_{ph} and E_{ph} values correspond to the volume and effective dose calculated using a standard CTDI method (phantom measurements) respectively. V and E values correspond to the actually exposed volume and recalculated effective dose to the patient during CT examination of the patient.

1 Table. Comparison of the doses obtained from the different calculation methods

V _{ph} , cm ³	V, cm ³	V/V _{ph}	E _{ph} , mSv	E, mSv	E/E _{ph}
Brain examination					
2752,5	2197,1	0,80	2,18±0,12	2,73±0,16	1,25
2958,4	2366,6	0,80	2,06±0,12	2,58±0,15	1,25
2689,6	2669,3	0,99	2,00±0,12	2,02±0,12	1,01
2813,4	3005,1	1,07	1,30±0,08	1,22±0,07	0,94
2251,3	2601,2	1,16	0,96±0,06	0,83±0,05	0,86
2967,6	2539,7	0,86	2,15±0,13	2,51±0,15	1,17
Face and neck examination					
2532,1	2350,2	0,93	1,71±0,10	1,84±0,11	1,08
3416,3	3553,9	1,04	2,31±0,14	2,22±0,13	0,96
2954,1	2478,1	0,84	1,65±0,10	1,97±0,12	1,19
3094,7	3859,6	1,25	1,73±0,10	1,39±0,08	0,80
2532,1	2466,3	0,97	1,42±0,08	1,46±0,09	1,03
2914,0	3172,2	1,09	1,63±0,09	1,50±0,09	0,92
1989,5	2348,4	1,18	1,29±0,07	1,09±0,06	0,84
2954,1	2391,9	0,81	1,65±0,10	2,04±0,12	1,24
3657,4	4211,5	1,15	2,05±0,12	1,78±0,11	0,87
2712,9	2995,1	1,10	1,52±0,09	1,38±0,08	0,91
2532,1	2516,6	0,99	1,71±0,10	1,72±0,10	1,01
2954,1	2919,2	0,99	1,99±0,12	2,01±0,12	1,01
2813,4	3093,1	1,10	1,57±0,09	1,43±0,08	0,91
2532,1	2173,4	0,86	1,80±0,11	2,10±0,13	1,17
2110,1	1801,2	0,85	1,18±0,07	1,38±0,08	1,17
3516,8	3038,3	0,86	2,75±0,16	3,18±0,19	1,16
3094,7	3584,7	1,16	1,42±0,08	1,23±0,07	0,87
2712,9	2646,8	0,98	1,47±0,09	1,51±0,09	1,03
2954,1	2616,7	0,89	1,65±0,10	1,86±0,11	1,13
2532,1	3044,4	1,20	1,42±0,08	1,18±0,07	0,83
2532,0	2743,2	1,08	1,42±0,08	1,31±0,08	0,92
2250,7	2114,6	0,94	1,26±0,07	1,34±0,08	1,06
2009,6	2051,1	1,02	1,12±0,07	1,10±0,06	0,98
1543,4	1136,3	0,74	1,04±0,06	1,41±0,08	1,36
1647,8	1657,7	1,01	1,55±0,09	1,54±0,09	0,99
Sinus examination					
1145,50	1753,10	1,53	0,62±0,04	0,41±0,02	0,66
1828,70	2533,20	1,39	0,78±0,05	0,56±0,03	0,72
2672,76	3216,00	1,20	1,13±0,06	0,94±0,06	0,83

The results presented in the Table1 show that the effective doses to patients during head CT examinations depend on the head size of the patient and on the actually exposed volume. It is evident that patients with the smaller head size (mostly women) received higher because of the reduced actually exposed volume. In some cases the doses were even 25% higher than it was necessary. Optimization of the exposure parameters in acquisition with the individual parameters of the patients would be of benefit for the CT patients.

References

1. Brix G. Assessment of a theoretical formalism for dose estimation in CT: an anthropomorphic phantom study/ G. Brix, U. Lechel, R. Veit et al // European Radiology, 2004 liep., T.14 Nr.7, p.1275-84
2. DeMarco J.J. A Monte Carlo based method to estimate radiation dose from multidetector CT (MDCT): cylindrical and anthropomorphic phantoms / J.J. DeMarco, C. Cagnon, D. Cody, D. Stevens et al.// Physics in Medicine and Biology, - 2005, september, T.50, Nr.17, p.3989-4004
3. EUR 16262 EN “European guidelines on quality criteria for computed tomography”
4. Hamberg L. Multi-detector row CT: radiation dose characteristics / L. Hamberg, J. Rhea, G. Hunter, J. Thrall // Radiology. – 2003, march., T.226, Nr.3, p. 762-772
5. Hidajat N. Relationships between physical dose quantities and patient dose in CT / N. Hidajat, J. Maurer, R. Schroder, A. Nunnemann et al. // The British Journal of Radiology. - 1999, Nr.72, p. 556-561
6. Jarry G. A Monte Carlo-based method to estimate radiation dose from spiral CT: from phantom testing to patient-specific models / G. Jarry, J. DeMarco, U. Beifuss, C. Cagnon et al.// Physics in Medicine and Biology. – 2003, august., T.48, Nr.16. p. 2645-63
7. Kawaura C. Organ and effective dose evaluation in diagnostic radiology based on in-phantom dose measurements with novel photodiode-dosemeters / C. Kawaura, T. Aoyama, S. Koyama, M. Achiwa et al. // Radiation Protection Dosimetry. – 2006, january, Nr. 26
8. M. Zankl Methods for Assessing Organ Doses using Computational Models // Radiation Protection Dosimetry. – 1998, T. 80, p. 207-212
9. Salvado M. Monte Carlo calculation of radiation dose in CT examinations using phantom and patient tomographic models // M. Salvado, M. Lopez, J. Morant, A. Calzado // Radiation Protection Dosimetry. – 2005, T.114, Nr.1-3, p. 364-368
10. Starck G. A method to obtain the same levels of CT image noise for patients of various sizes, to minimize radiation dose / G. Starck, L. Lönn, Å. Cederblad, E. Forssell-Aronsson et al. // British Journal of Radiology. – 2002, Nr.75, p.140-150
11. 1990 Recommendations of the International Commission on Radiological Protection. ICRP Publication 60. Annals of the ICRP 21, 1-3.

APPLICATION OF X-RAY APPARATUS FOR BIOMEDICAL INVESTIGATIONS

Virgilijus Minialga

*Kaunas University of Technology, Department of Physics
e-mail: virmin@ktu.lt*

Abstract

The X-ray apparatus primarily designed for teaching purposes can be used for demonstration and investigation of limited volume technological and biological objects. The simple experiments using luminous screen for internal structure investigations, measurement of ionization current for ion dose rate calculation, measurements for X-rays attenuation in materials can be carried out. Errors of measurements appear because of limited intensity of radiation and accuracy of experimental equipment designed for teaching experiments.

Key words: *X-rays; luminous screen, X-rays attenuation, expose dose.*

The X-ray apparatus is designed for carrying out a wide variety of experiments in physics first of all. It can be applied for investigations in related disciplines too. Between experiments in medicine are the transillumination of objects and observing them on a fluorescent screen or on an X-ray film, and experiments on ionization and dosimetry. Measurement of material-dependent and thickness-dependent attenuation of X-rays is also important for understanding the safety requirements working with X-ray equipment.

The apparatus consists of two main chambers: the X-ray tube chamber and experiment chamber. It is possible to set all parameters of X-ray apparatus manually and read them from the digital display. They use for angular dependencies of scattered rays two arms goniometer. Usually, the sensor is Geiger – Mueller counter tube. Microprocessor controlled this apparatus can be used as a stand-alone device, in conjunction with a computer via the built-in RS-232 interface or with an XY recorder connected.

Investigation of fluorescence of a luminous screen due to X-rays should be carried out in darkened room. The transillumination object, e.g. pocket calculator or prepared biological sample, should be placed in the experimental chamber as close as possible in front of the luminous screen and the lead glass sliding doors should be closed. Then the high voltage for X-ray tube can be set at 35kV. The brightness of the luminous screen can be changed by changing emission current and applied voltage of the x-ray tube.

The visible X-ray tube with molybdenum anode emits wide spectrum of x-rays at low anode voltages (till 15kV). Several lines in the spectrum appear when the anode voltage increases from 20kV to 35kV. The energy of photons and wavelengths in these lines are $K_{\alpha} = 17,4$ keV, i.e. $\lambda_{\alpha} = 71,1$ pm, and $K_{\beta} = 19,6$ keV, i.e. $\lambda_{\beta} = 63,1$ pm.

The luminous screen show image of the internal structure of the illuminated object. These experiments explain the great importance of x-rays in non-destructive testing of materials and in diagnostic medicine. Fig.1 shows an image of pocket calculator obtained by transillumination. Sharpness of the image depends on X-rays source dimensions and on the distance of object or its parts from the luminous screen. The image of biological object, i.e. dead mouse is on Fig. 2. Small details cannot be resolved without additional means for improved resolution.

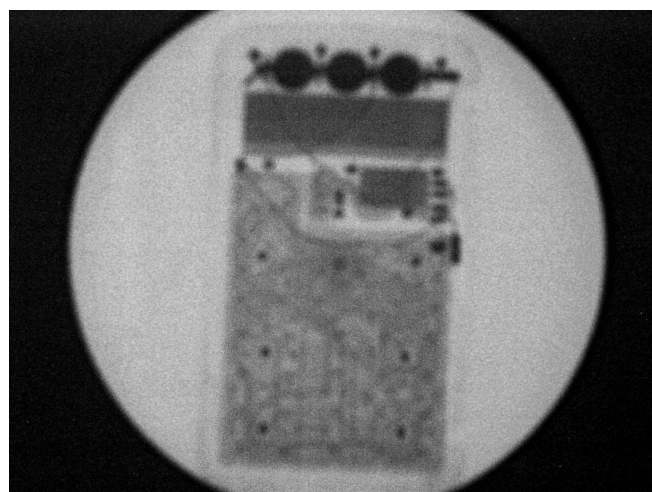


Fig. 1. Image on the luminous screen of pocket calculator obtained by transillumination by X-rays

For determination of the ion dose rate of the X-ray tube the experiment chamber should be equipped with ionization chamber. It consist of two parallel one to other metal plates with different electrical potentials. The saturation ionization current should be measured. The charge quantity dQ obtained from this current measurement is used for ion dose (or expose dose) calculation:

$$J = \frac{dQ}{dm} \quad (1)$$

where dm is the mass of irradiated volume element.



Fig. 2. Image of dead mouse on the luminous screen obtained by transillumination by X-rays

The absorbed dose can be calculated as quotient:

$$K = \frac{dW}{dm} \quad (2)$$

where dW is the energy absorbed by irradiated material.

The rates of these values are:

$$j = \frac{dJ}{dt} \quad \text{and} \quad k = \frac{dK}{dt} \quad \text{accordingly.} \quad (3)$$

In this way the simple experiments and more fundamental investigations can be carried out using the X-ray apparatus. The errors of measurements are caused by relatively small intensity of X-rays and accuracy of modeled experimental equipment in experiment chamber.

Reference

1. Instruction sheet 554811; X-ray apparatus: Lehr- und Didaktiksysteme, LD Didactic GmbH, 2005

SAFE USE OF IONISING RADIATION IN MEDICINE

ICRP'S CURRENT RECOMMENDATIONS AND ONGOING WORK

Sören Mattsson

Department of Medical Radiation Physics

Malmö University Hospital, SE-205 02 Malmö, Sweden and ICRP Committee 3,

soren.mattsson@med.lu.se

Abstract

The presentation will give an overview of the current ICRP recommendations and the ongoing work within the ICRP and its Committee 3 with respect to the safe use of ionising radiation in medicine. The new main recommendations will include a section, which in part will update the ICRP Publication 73: Radiological Protection and Safety in Medicine (1996). The Commission has in its last two terms (1997-2001; 2001-2005) published a number of documents prepared by Committee 3 that provide detailed advice related to radiological protection and safety in the medical applications of ionising radiation. Each of these publications addresses a specific topic defined by the type of radiation source and the medical discipline in which the source is applied, and was written with the intent of communicating directly with the relevant medical staff.

Key words: ICRP, ionising radiation, protection, medicine

Introduction

Medical procedures represent the largest source of human-made radiation exposures. In countries with advanced health care systems, the annual number of diagnostic procedures approaches or exceeds one for every member of the population. Furthermore, the doses to patients for the same type of examination differ widely from place to place, suggesting that there is considerable scope for management of patient dose. The aim of this paper is to summarise the current ICRP recommendations with respect to the safe use of ionising radiation in medicine.

Magnitude of the problem

Radiation exposures in medicine are predominantly to the individuals undergoing diagnosis, screening, or therapy. Staff and other individuals helping to support and comfort patients are also open to exposure. These individuals include parents holding children during diagnostic procedures, and others, normally family or close friends, who may come close to patients following the administration of radiopharmaceuticals or during brachytherapy. Exposure to members of the general public also occurs, but it is almost always very small. Radiological protection in medicine refers to all these exposures.

The use of radiation for medical diagnostic examinations contributes over 95 percent of man-made radiation exposure and is only exceeded by natural background as a source of exposure (1). In the next few years particularly as a result of the rapidly spreading use of computed tomography (CT) in developed countries, radiation uses of medicine may exceed natural background as a source of population exposure.

UNSCEAR (1) compared estimates of the 1985-1990 and 1991-1996 periods and concluded that the worldwide annual per caput effective dose increased by 35 percent and the collective dose by 50 percent, while the population increased by only 10 percent. In 2000, there were about 2 000 million medical x-ray investigations and 300 million dental x-ray investigations made each year in the world using about 2 million x-ray units. Most of the investigations (3/4 and 9/10 respectively) are carried out on 1/4 of the world's population (for which the medical investigations give an effective dose per capita of 1.2 mSv/year). On top of that there are 32 million investigations in diagnostic nuclear medicine and 5.5 million patients treated per year in radiation therapy (1, 2). These numbers are expected to increase in future years.

In our part of the world, there has been a dramatic change of CT-investigations (more procedures, more scans per procedure). Today the contribution from CT investigations dominates the collective dose from diagnostic radiology in many countries. Interventional procedures, increasingly being used to replace surgery, can lead to very high local skin doses, in some cases exceeding the threshold for deterministic effects (6). For most x-ray examinations, there are still too large inter-hospital variations in doses for the same type of examination. Digital radiology, which has the potential to lower the doses, for most investigations still sometimes shows higher doses than earlier conventional film-screen technique.

While it is difficult to estimate the number of occupationally exposed medical workers, UNSCEAR (1) estimated that monitored medical-radiation workers exceed 2.3 million, thus being the largest group of radiation workers.

ICRP publications

Publication 73 'Radiological Protection and Safety in Medicine' (4) was published in 1996 to expand on the application in medicine of the 1990 recommendations of the Commission (Publication 60) (3). The Commission

is currently preparing an updated set of recommendations, and Committee 3 has produced a “Building Block Document” summarizing the key issues in relation to the use of radiation in medicine and a potential approach to address them. This is done in the light of the fact that recommendations take years to be implemented in terms of guidance and regulations and that many regulators are very cautious in advising the medical community and the patients due to the requirement to balance benefits and risks. Moreover changes in medicine and health care are driven by a number of other factors than radiation protection of the patient. There are a number of professional, technological, social and economic factors. The Building Block Document will describe the rationale and approach to radiation in medicine that has evolved over the last two terms of Committee 3, particularly with regard to patients undergoing medical procedures. In its last two terms (1997-2001; 2001-2005), the commission has published a number of documents prepared by Committee 3 that provide detailed advice related to radiological protection and safety in the medical applications of ionising radiation. Each of these publications addresses a specific topic defined by the type of radiation source and the medical discipline in which the source is applied, and was written with the intent of communicating directly with the relevant medical practitioners and supporting medical staff. These publications (in chronological order) are:

- Pregnancy and Medical Radiation (Publication 84) (5)
- Avoidance of Radiation Injuries from Medical Intervention Procedures (Publication 85) (6)
- Prevention of Accidental Exposures to Patients Undergoing Radiation Therapy (Publication 86) (7)
- Managing X-ray Dose in Computed Tomography (Publication 87) (8)
- *Radiation and Your Patient: A Guide for Medical Practitioners (Supporting Guidance 2)* (9)
- *Diagnostic Reference Levels in Medical Imaging - Review and Additional Advice (Supporting Guidance 2)* (10)
- Managing Patient Dose in Digital Radiology (Publication 93) (11)
- Release of Patients after Therapy with Unsealed Radionuclides (Publication 94) (12)
- Prevention of High-Dose-Rate Brachytherapy Accidents (Publication 97) (13)
- Radiation Safety Aspects of Brachytherapy for Prostate Cancer using Permanently Implanted Sources (Publication 98) (14)

Also, in 1998, the Commission published “Radiation Dose to Patients from Radiopharmaceuticals” (Publication 80) (15), a joint effort of Committees 2 and 3, that presented biokinetic and dosimetric data on ten new radiopharmaceuticals not previously published and updated the similar data presented in the series of earlier ICRP publications on this subject. For some of the publications there is educational material freely available on www.icrp.org (go to publications, free educational downloads). For the moment there is material, which summarises:

- ICRP Publication 84, Pregnancy and medical radiation
- ICRP Publication 85, Interventional radiology
- ICRP Publication 86, Accidents in radiotherapy
- ICRP Publication 87, CT dose management
- ICRP Publication 93, Digital radiology (English and Spanish)

ICRP current activities

Currently, Committee 3 has a number of documents in preparation addressing the following topics:

- Radiation protection for cardiologists performing fluoroscopically guided procedures (Task Group)
- Radiation protection issues of modern radiotherapy techniques (Joint Task Group with ICRU)
- Radiation dose to patients from radiopharmaceuticals (Joint Task Group with Committee 2).
- Protecting children: Diagnostic techniques involving ionising radiation (Working Party)
- Doses to the hands of radiopharmacists (Working Party)
- Radiation protection training for diagnostic and interventional procedures (Working Party)
- Justification of intended individual (non-occupational and non-security) exposures to ionising radiation without sole medical benefit (often referred to as medico-legal exposures) (Task Group)
- Medical examinations and follow-up of persons accidentally or occupationally exposed to ionising radiation (Working Party)
- Medical screening of asymptomatic persons using ionising radiation (Working Party)
- Managing patient dose in multi-detector computed tomography (Task Group)

Additional advice from Committee 3 concerning radiation protection in medicine will be forthcoming as these documents are completed.

References

1. UNSCEAR. Sources and effects of ionizing radiation. 2000 Report to the General Assembly, with scientific annexes. Volume I: Sources, United Nations, New York, USA, 2000
2. Shrimpton P. C. The current use of radiation in medicine In: Radiological protection of patients in diagnostic and interventional radiology, nuclear medicine and radiotherapy. IAEA Vienna, 2001, 109-118 p
3. ICRP. 1990 Recommendations of the International Commission on Radiological Protection (Publication 60). – Ann. ICRP, 21, N1-3, 1992

OPTIMISATION OF PATIENT DOSES IN DIGITAL RADIOLOGY AND THE SENTINEL PROJECT

Kalle Kepler¹, Anatoli Vladimirov¹

¹Training Centre of Medical Physics and Biomedical Engineering,
University of Tartu, Tähe 4, Tartu, Estonia, kalle.kepler@ut.ee

Abstract

In recent years conventional film-screen radiography has been very rapidly replaced by digital (computed radiography) techniques in Estonia. Quality assurance in hospitals has been supported by the quality control provided by the Testing Centre of the University of Tartu. New strategies for optimisation and quality assurance for digital radiography have been introduced by the SENTINEL partners recently. It includes consideration to diagnostic requirements of a given clinical situation, but also objectivation and standardisation of image quality, and constancy testing. The aim of this work was to evaluate the performance of the CR systems in order to optimally calibrate the AEC devices.

Keywords: patient dose optimisation, computed radiography, SENTINEL

In recent years conventional film-screen radiography has been very rapidly replaced by digital (computed radiography, CR) techniques in Estonia. Quality assurance in hospitals has been supported by the quality control provided by the Training Centre of Medical Physics and Biomedical Engineering (TÜ BMTK). The Centre has started its activities in the field of quality assurance and quality control of radiological equipment in 1998. The Testing Centre (in cooperation with TÜ BMTK) was accredited by the international testing laboratory standards ISO/IEC 17025 in 2003 and it covers most of the diagnostic x-ray QC tests all over the country [1, 2].

Now (autumn 2006) there are 27 CR systems (incl. 2 scanners in mammography) from different manufacturers (Agfa, Fujifilm, Philips, Kodak, Konica) installed in Estonia. Two digital radiography systems (Fujifilm FCR Velocity U, Imix THX-2000) are based on CCD detectors. The first direct Radiography system (flat panel detectors) for conventional radiography will be implemented in Tallinn Diagnostic Centre this year.

Estonian Radiation Act (renewed in 2004) includes provisions delegating authority to the Ministry of Social Affairs for harmonising 97/43/Euratom requirements. Unfortunately any special regulation on the usage of medical exposures and patient dose management has not been set into force yet in Estonia. The former Regulation (1998) is not in force any more, but in practice as a requirement in the Radiation Practice Licence the QC tests of x-ray equipment have to be done in every 2 years. These tests have to be done by hospital medical physicists or to be ordered from TÜ BMTK.

TÜ BMTK test methods have been adapted from IEC standards for acceptance tests (IEC 61223-3-1, IEC 60601-1-3) and constancy tests (IEC 61223-2-1, IEC 61223-2-11). For digital radiography the same tests for generator/collimator part and dose optimisation with PMMA phantom and line pair resolution test pattern were used. Noise level was determined on DICOM image.

Using a method introduced in Malmö conference 2004 by Doyle et al [3] for optimising automatic exposure control in computed radiography the optimisation was performed in several hospitals with newly installed CR systems. Initially the AEC was adjusted by Agfa or GE engineers. MAS was recorded for 15 cm PMMA on bucky table.

AEC was adjusted for optimal dose by noise level and taking into account that for Kodak system exposure index EI should be at least 1500. For enough image quality it is not recommended to use less doses than 2,5 µGy for the phosphor plate [3]. Dose in image plate was calculated by Kodak formula

$$E_{\text{Kodak}} = 8,7 \times 10^n ,$$

where $n = \frac{EI - 2000}{1000} .$

The results of optimisation for CR system compared with film-screen radiography are given in Table 1.

Table 1. Dose optimisation parameters for CR compared with film-screen system.

AEC adjust-ment	kV	mAs	Exp. index	Dose in image plate (μGy)	ESD on phantom (μGy)	Pixel number	Noise (stand. dev.)	Relat. noise
Film-screen	80	4,26	N/A	N/A	366	N/A	N/A	N/A
CR1	80	8,04	1650	3,89	692	2503	98	3,9
CR2	80	6,87	1610	3,54	591	2587	65	2,5
CR3	80	5,59	1530	2,95	481	2571	69	2,7

After the optimisation procedure entrance surface dose (ESD) was measured and compared with and compared with ESD of non-optimised CR systems. Radiation measurements were done by Keithley Triad QA ionisation chamber or RTI Barracuda dosimeters. The results of the comparison are presented in Figure 1.

It is seen from the figures that the optimisation is most critical at low kilovoltages (e.g. at 60 kVp), where the difference in AEC adjustment curves is highest for CR and film-screen systems.

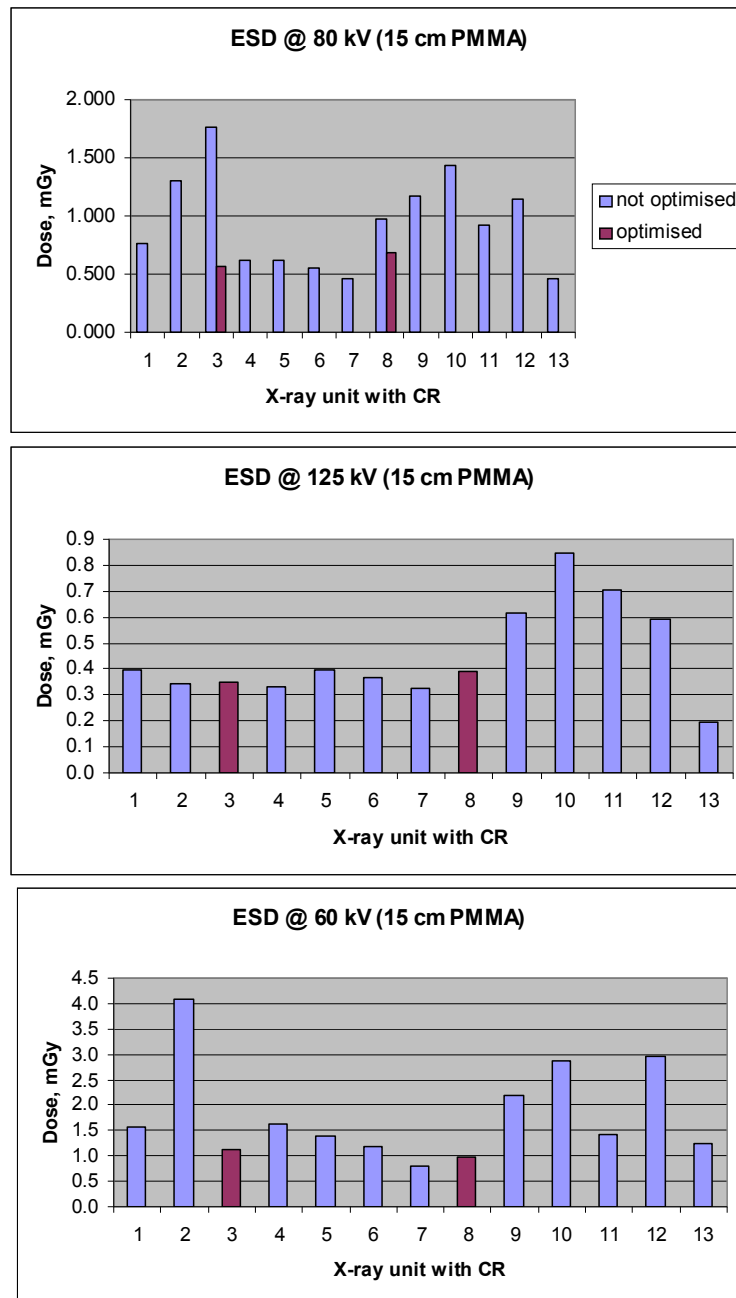


Fig. 1. Entrance surface dose in optimized and non-optimized CR systems.

New strategies for optimisation and quality assurance for digital radiography have been introduced by the EU SENTINEL Project (Safety and Efficacy for New Techniques and Imaging Using New Equipment to Support European Legislation: Supporting Digital Medicine) [4]. It includes consideration to diagnostic requirements of a given clinical situation, but also objectivation and standardisation of image quality, e.g. using CDRAD test phantom, and constancy testing [5].

SENTINEL is a Europe-wide project, which consists of 23 partners from 17 EU Member States and 3 Candidate States, who are looking at effectiveness, safety and ethical issues around the use of imaging equipment and systems in healthcare, including those used for X-rays, scans and breast screening but excluding CT.

SENTINEL work plan includes activities in the following work packages: functional performance and standards, efficacy and safety in digital radiology, in dentistry and in nuclear medicine, in cardiology, in interventional radiology and in population screening/ sensitive groups, justification, ethics and efficacy issues and good practice guidance and training in this field.

Special questions concerning optimization of dose and image quality in digital radiology were raised in the second work package:

- optimisation studies of image post processing algorithms;
- optimisation studies of AEC curves for digital applications;
- choice of standard phantoms for image quality evaluation;
- development of test protocols for new detectors.

More materials and details about SENTINEL activities are available in the Project webpage [6].

References

1. Kepler K., Vladimirov A. and Servomaa A. Interlaboratory comparison and accreditation in quality control testing of diagnostic X-ray equipment"- Rad. Prot. Dosimetry, 114, No. 1-3, 2005, 198 - 200 p.
2. Rodima A. et al. ISO 17025 quality system in a university environment - Accreditation and Quality Assurance, 10, 2005, 369 - 372 p.
3. Doyle P., Gentle D. and Martin C. J.. Optimising automatic exposure control in computed radiography and the impact on patient dose - Rad. Prot. Dosimetry, 114, 2005, 236 - 239 p.
4. Busch H. P. and Faulkner K. Image quality and dose management in digital radiography: a new paradigm for optimization - Rad. Prot. Dosimetry, 117, No. 1-3, 2005, 143 - 147 p.
5. Busch H.P. Image quality and dose management for digital radiography. DIMOND III. Final Report. Trier, 2004.
6. <http://www.dimond3.org/>

PATIENT'S DOSE MEASUREMENTS IN THREE LITHUANIAN HOSPITALS

J.Žiliukas

Radiation Protection Centre, Kalvarijų st. 153, LT-08221 Vilnius, j.ziliukas@rsc.lt

Abstract

One of the most important sources of human exposure is medicine. The largest collective doses are received in medical X-ray diagnostic. Dose limits for medical exposure do not exist like it is established in occupational and public exposure. In Lithuania there are established diagnostic reference levels (DRL) for radiographic examinations. European Guidelines for image quality and examples of good practice are prepared and published by European Commission. The measurements of patient's doses in Lithuanian hospitals were made. The entrance surface doses (ESD) were measured using termoluminescent dosimeters (TLD). The measurement results and information from three Lithuanian hospitals shows that the X-ray exposure parameters are very different in different hospitals and average entrance surface doses in some cases exceed the Lithuanian diagnostic reference levels. This survey of patient doses shows that measurements of patient doses during X-ray examinations is a very powerful tool for optimization of patient doses and image quality.

Key words: entrance surface dose (ESD), diagnostic reference level (DRL), termoluminescence dosimeter (TLD)

Introduction

One of the most important sources of human exposure is medicine. The largest collective doses are received in medical X-ray diagnostic. Dose limits for medical exposure do not exist like it is established in occupational and public exposure. In Lithuania there are established diagnostic reference levels (DRL) for radiographic examinations [1] and hospitals should keep it. European Guidelines for image quality and examples of good practice are prepared and published by European Commission [2]. But very often there are problems with implementation of these guidelines in practice and hospitals use their own experience to do examinations. It is very important to achieve balance between image quality and patient dose. The measurements of patient's doses help to optimize the X-ray diagnostic examinations.

Method

The hospitals for measurements were selected randomly and equipment used for X-ray diagnostic examinations was comparably new. Results received in three Lithuanian hospitals were selected for this paper. Four different types of X-ray radiography examinations were selected in hospitals for investigations. Entrance surface dose (ESD) was measured. Selected patients were patients of standard weight. According to the description of International Radiation Protection Commission the typical adult patient is a man of 70 kg weight and 170 cm height and a woman of 58 kg weight and 160 cm height. In Lithuania the standard patient is (70 ± 10) kg, not sorting by height and sex [1]. The termoluminescent dosimeters (TLD) were used for measurements.

The TLDs are prepared and placed into labeled, plastic, not light proof bags. The bags with TLD are fixed on the top of skin of the selected patient in the hospital, in the center of exposure area from side of primary beam direction [3]. The radiographer sets the X-ray exposure parameters of examination and makes exposure. Data about patient (age, height, weight and sex) and X-ray exposure parameters (kVp, mAs, focal skin distance (FSD), total filtration, cassette size) are recorded in the protocol. After exposure the TLD is removed from the patient. Exposed TLDs are returned to Radiation Protection Center and read out with RADOS system.

Later the ESD's were evaluated and in case of exceeding DRL the hospitals took corrective actions and measurements were repeated.

Results

The distribution of the patient by sex and weight are presented in Table 1.

X-ray examination	Number of patients	Sex		Weight, kg	
		Men %	Woman %	Range	Average and confidens of 95%
Chest PA	30	50	50	45-84	68±4
Skull LAT	20	35	65	46-98	71±5
Hip joint AP	18	33	66	60-86	77±3
Lumbar spine AP	20	35	65	56-80	73±3
Lumbar spine LAT	30	40	60	49-83	70±3

Table 1. Distribution of examined patients by sex and weight

From the Table 1 it is evident that examinations were carried out more for women except for chest PA examination. It is very difficult to collect the patients of appropriate weight, therefore in some cases measurements were made for patients over weighted. In spite of it the average weight of examined patients was in range of (70±10) kg. In hip joint AP examinations for two patients the TLD were fixed incorrectly and results were omitted. The X-ray equipment in all three hospitals was the same, Mercury 332, installed in 2002. Table 2 shows the average X-ray exposure parameters used for examinations.

X-ray examination	X-ray exposure parameter*	Hospital no. 1	Hospital no. 2	Hospital no. 3
Chest PA	kVp	82	48	127
	mAs	13	59	1
	AEC	Not used	Used	Used
	FFD	130	110	150
Skull LAT	kVp	64	62	-
	mAs	41	113	-
	AEC	Not used	Used	-
	FFD	100	110	-
Hip joint AP	kVp	-	70	56
	mAs	-	296	182
	AEC	-	Used	Used
	FFD	-	110	120
Lumbar spine AP	kVp	71	-	59
	mAs	133	-	160
	AEC	Used	-	Used
	FFD	100	-	120
Lumbar spine LAT	kVp	76	93	67
	mAs	281	210	200
	AEC	Used	Used	Used
	FFD	100	110	120

* AEC – automatic exposure control, FFD – focus film distance

Table 2. X-ray exposure parameters used for X-ray examinations in different hospitals

As seen in Table 2, different hospitals for the same type of X-ray examinations use different X-ray exposure parameters using the same type of X-ray machines. Patient dose and image quality depend on exposure parameters. The lower kVp requires higher mAs [4, 5]. With the lower kVp the image has higher contrast and increasing of kVp decreases contrast of images [4, 5]. For evaluation of bone structures (spine, skull, etc.) it is recommended image to have with higher contrast and for soft tissues (lungs, etc.) with lower contrast [4, 5]. The image quality should not be the best but optimum and enough to answer the clinical questions, i.e., make diagnosis. It is necessary for optimization of patient dose. European Guidelines [2] recommend the X-ray parameters for different types of examinations.

Table 3 shows average ESD in different hospitals average setting of X-ray parameters. The ESD compared with X-ray parameters recommended by European Guidelines [2] for separate X-ray examinations.

X-ray examination	Hospital no.	ESD and 95 % confidence	kVp	mAs	AEC	FFD, cm
Chest PA	1	0,75 ± 0,17	82	13	Not used	130
	2	2,08 ± 0,71	48	59	Used	110
	3	0,08 ± 0,03	127	1	Used	150
	DRL, and EGL*	0,6	125		Used	140-200
Skull LAT	1	3,8 ± 0,45	64	41	Not used	100
	2	5,3 ± 1,57	62	113	Used	110
	DRL, and EGL	3	70-85		Used	100-150
Hip joint AP	2	20,7 ± 9,1	70	296	Used	110
	3	9,8 ± 1,4	56	182	Used	120
	DRL, and EGL	10	75-96		Used	100-150
Lumbar spine AP	1	17,4 ± 5,3	71	133	Used	100
	3	10,4 ± 1,8	59	160	Used	120
	DRL, and EGL	12	75-90		Used	100-150
Lumbar spine LAT	1	50,7	76	281	Used	100
	2	19,2	93	210	Used	110
	3	19,1	67	200	Used	120
	DRL, and EGL	35	80-95		Used	100-150
DRL – diagnostic reference level, EGL – European Guidelines						

Table 3. Average results of patient dose measurements and comparison with Lithuanian DRL and European Guidelines

From Table 3 it is seen that the ESD of chest PA examinations were exceeding DRL in hospitals where kVp and focal film distance (FFD) was much smaller than recommended by [2]. Automatic exposure control (AEC) system in hospital 2 was not used. Average ESD for skull LAT examinations exceeded Lithuanian DRL in both hospitals. The kVp used was too low. Average ESD in hip joint AP, lumbar spine AP and LAT examinations were higher because kVp were lower than recommended and AEC system were not properly adjusted.

The maintenance staff of hospitals where doses exceeded DRL adjusted the X-ray machines. Exposure parameters were corrected according the European Guidelines and image quality. Measurements were repeated. Figure 2 shows the results of two hospitals the first measurements and after corrective actions in chest PA examinations.

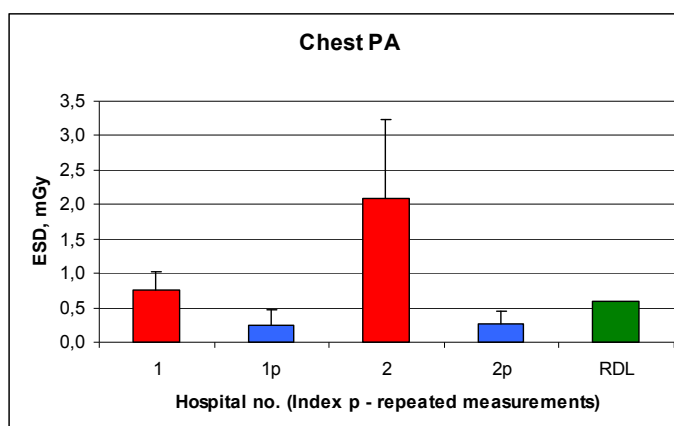


Fig. 2 Average entrance surface doses of first measurements and after corrective actions

The average ESD after adjusting of X-ray machines and correction of X-ray parameters was decreased more than twice in hospital 1 and about seven times in hospital 2. The ESD in both hospitals after repeated measurements were about 0,3 mGy.

Conclusions

Collected information shows that different hospitals use very different exposure parameters for the same type of examinations with the same type of X-ray equipment.

Results of dose measurements show that the average entrance surface doses for different examinations in some cases exceed the Lithuanian diagnostic reference levels for radiography.

Comparison of X-ray parameters with recommended in European Guidelines shows that in cases where these parameters do not comply by recommended ones the ESD in all cases exceed DRL.

After adjusting of X-ray machines and taking corrective actions the average ESD in hospitals was decreased and image quality was on the optimum level.

Measurements of patient doses during X-ray examinations are a very powerful tool for optimization of patient doses and image quality.

References

1. Radiation Protection Requirements in Medical X-rayDiagnostics HN 31:2002 (Žin., 2003, Nr. 9-308).
2. European Gudelines on Quality Criteria for Diagnostic Radiographic Images, European Commission, EUR 16260 EN, Luxembourg, 1996, 82 p.
3. D.Hart, D.G.Jones and B.F.Wall, Estimation of Effective Dose in Diagnostic Radiology from Entrance Surface Dose and Dose-Area Product Measurements. NRPB-R262, ISBN 0 85951 363 7, Chilton Didcot, Oxon OX11 0RQ, 1994;
4. Curry T.S., Dowdey J.E., Murry R.C. Christensen's Physics of Diagnostic Radiology - 4th ed, London, 1990, 522 p.
5. Statkiewicz Sherer M.A., Visconti P.J., Ritenour E.R., Radiation Protectio in Medical Radiography -4th ed, Mosby, 295 p.

DOSE EVALUATION USING *in vivo* TLD DOSIMETRY IN MAMMOGRAPHY

I. Cibulskaitė^{1,2}, R. Plaipaitė¹, E. Garnytė¹, E. Skripkaite¹, S. Mockevičienė¹, D. Adlienė¹
V. Burinskienė^{1,2}, A. Andrijaitienė³, G. Šetikienė⁴, A. Urbonienė⁵

¹Kaunas University of Technology,

²Kaunas Medical University Hospital,

³Klaipėda Hospital,

⁴Šiauliai hospital

⁵Radiation Protection Centre

Abstract

Thermoluminescence dosimetry method has been used for the evaluation of the average breast dose of the patients undergoing X-ray mammography examinations. The results of TLD *in vivo* measurements performed in four Lithuanian medical institutions are presented in this paper.

Key words: *thermoluminescence dosimeters, entrance surface dose, glandular dose.*

Introduction

According to the data of the cancer register [1], women morbidity because of the breast cancer in Lithuania becomes more often. The detection of early stage of the breast cancer is important, so screening programs are introduced in the hospitals. One type of the examinations preformed during the screening programs is mammography. Hospitals, participating in these programs, must fulfil strict requirements for quality that are stated in the local hygiene norms.

Table 1. Woman morbidity because the breast cancer 2003 – 2005 year

Year	Number of the cases	Morbidity for 100 000 habitants
2003	1312	71,3
2004	1308	71,4
2005	1321	72,1

The typical effective dose for mammogram is 50 µSv which gives a risk of a fatal cancer of 1 in 400 000 [2]. It seems that the risk from mammogram is small, but during screening programs a lot of women are examined and there is a risk that some will get cancer from X-ray. Breast tissue is sensitive to radiation, that's why justification and optimization of these examinations especially, when they are used for screening purposes, are important.

In order to investigate, what doses are received by woman during mammography examinations, TLD *in vivo* method was used. According papers [3] TLD's offer the best option for *in vivo* measurements in mammography. Because of their high sensitivity and small size it is convenient to place them anywhere on the skin, besides most of the thermoluminescence materials have good equivalence to tissue ($Z_{eff} \sim 8$, compared to about 7 for tissue). The application of the TLD's in vivo methods was limited due to their visibility in the mammograms. That's why it is important to inform radiologists, evaluating mammograms, about the possible visibility of the TLD in the mammogram. As TLD pellets have exact form on the image, they are clearly recognized by radiologist in the image.

The dose received by glandular tissue (AGD) during the mammography examinations could be calculated from the measured entrance surface dose (ESD) applying relative *in vivo* thermoluminescence dosimetry method. According to the recommendations of the European protocol on dosimetry in mammography [4], the entrance surface air kerma (ESAK) could be calculated dividing measured ESD value by appropriate backscatter factor, which depends upon HVL [4]. If there is no information about HVL of the X-ray mammography equipment, factor 1.09 could be used. It is recommended to measure radiation output and half-value layer (HVL) before the measurements on patients are undertaken. Usually it is done during the periodical quality control measurements of mammography unit. Variations of the half value layer of mammography unit with Mo anode and Mo are not significant as it is stated in [4], therefore ESAK value alone can be taken as an adequate indicator for the level of the AGD. The relationship of ESAK to AGD is different for other target/filter combinations (Mo/Rh), while in this case the large deviations in half value layer occur. The uncertainty of the measured half value layer in order of 0.05 mm Al corresponds to a difference in conversion factors of g of 10 %.

Table2. Backscatter factor as a function of HVL (Jensen et al. 1994) [4]

HVL (mm Al)	0.25	0.30	0.35	0.40	0.45	0.50	0.55	0.60	0.65
Backscatter factor	1.07	1.07	1.08	1.09	1.10	1.11	1.12	1.12	1.13

Multiplying measured value of ESAK by the appropriate conversion factors it is possible to evaluate the – average glandular dose:

$$AGD = ESAKgcs , \quad (1)$$

where g is the incident air kerma to mean glandular dose conversion factor; the factor c corrects the dose value for any difference in breast composition from 50 % glandularity and the factor s corrects the dose for any difference from the original tabulation by Dance (1990) due to the use of the different X-ray spectrum. [5]. The conversion factor g (Table 3) depends upon the breast thickness, the quality of the X-ray beam and the glandularity of the breast [5,6].

Table3 .g-factors (mGy/mGy) for breast thicknesses of 2-11 cm and the HVL range 0.30-0.60 mm Al.

The g-factors for breast thicknesses of 2-8 cm are taken from Dance (1990). [5].

Breast thickness (cm)	HVL (mm Al)						
	0.30	0.30	0.40	0.45	0.50	0.55	0.60
2	0.390	0.433	0.473	0.509	0.543	0.573	0.587
3	0.274	0.309	0.342	0.374	0.406	0.437	0.466
4	0.207	0.235	0.261	0.289	0.318	0.346	0.374
4.5	0.183	0.208	0.232	0.258	0.285	0.311	0.339
5	0.164	0.187	0.209	0.232	0.258	0.287	0.310
6	0.135	0.154	0.172	0.192	0.214	0.236	0.261
7	0.114	0.130	0.145	0.163	0.177	0.202	0.224
8	0.098	0.112	0.126	0.140	0.154	0.175	0.195
9	0.0859	0.0981	0.1106	0.1233	0.1357	0.1543	0.1723
10	0.0763	0.0873	0.0986	0.1096	0.1207	0.1375	0.1540
11	0.0687	0.0786	0.0887	0.0988	0.1088	0.1240	0.1385

In order to simplify the estimation of the mean glandular dose, tables of c-factors for typical breasts for the women in the age group of 50 to 64 years and of 40 to 49 years are tabulated [5]. The c-factors are obtained by using the estimates of the average glandularity for a range of HVL's and breast thicknesses. The spectral correlation factor so called s-factor is used in order to apply the old g-factor to clinically used spectra.

In vivo TLD measurements

TLD method was used to measure the entrance surface doses of the breast of the patient undergoing mammography screening procedure. LiF:Mn,Ti (TLD tablet with a diameter of ~ 5 mm) dosimeters were calibrated at the representative energy and beam quality at the Secondary Standard Laboratory in Latvia. The reading of the thermoluminescence dosimeters was performed by RADOS TLD system at Radiation Protection Centre, following standard procedures. Each was put into the transparent, low attention material (plastic) sachet.

The measurements were performed in four medical institutions of Lithuania, where screening programs are introduced. Mammography examinations of patients were carried out using ALFA RT or Mammomat 100 (Siemens) mammography units with grid, Mo/Mo anode and filter combination; Kodak Min-RD, Cawo Mammo R200 film cassettes and Kodak X-Omat, Konica Minolta films. Measurements of entrance surface dose (ESD) during mammography screening and in some cases diagnostic (tube potential 23 – 35 kVp) were performed for randomly selected groups of ~ 13 patients. The total number of examined patients was 53. The dosimeters were positioned on the breast surface of the patient and exposed during X – ray examination procedure. Evaluation of the ESAK for single exposure was performed.

Mammography screening examination consisted of four exposures: exposure of the right and left breast in CC (Cranio-Caudal) projection and in MLO (Medio-Lateral-Oblique) projection. Because of the TLD visibility on the radiographic image, it is recommended to position TLD in the upper inner quadrant of the patient's breast

surface, where the risk of obscuring clinically important detail is less. The necessary data was recorded: type of the view (cranio-caudal medio-lateral-oblique), age of patient, exposure field and for every single exposure the values of tube voltage, tube loading, anode/filter combination, thickness of the compressed breast and compression force.

Measurements were not performed for the patients with possible breast cancer indications.

Results and discussions:

The largest group of the patients was in the age of 45 – 68 years. In some cases measurements were done also during diagnostic examinations, so the age of the woman varied from 39 to 69 years. ESD values per exposure for all examined patients varied in a broad area: from 2.66 mGy to 11.97 mGy in the first institution (I1), from 6.65mGy to 27.72 mGy in the second institution (I2), from 2.39 mGy to 14.01 mGy in the fourth institution (I4) and was equal to 5.84 mGy in the third institution (I3). Variations of ESD for CC projection exposure for 5.5 cm compressed breast thickness in I1 are presented in Fig.2.

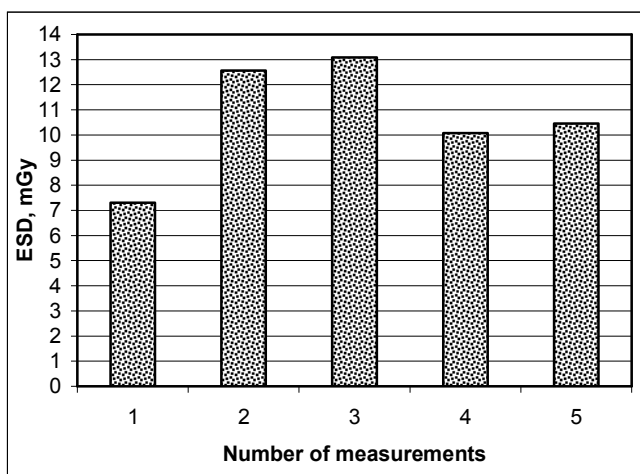


Fig.2. Variations of ESD for CC projection exposure for 5.5 cm compressed breast thickness

Averaged values of ESD and also AGD, calculated according the results of dose measurements for different compressed breast thicknesses at selected hospitals are presented in Table 4.

Table 4. Averaged values of ESD and AGD, calculated according the results of dose measurements for different breast thickness at medical institutions.

d, cm	First institution (I1)		Second institution (I2)		Third institution (I3)		Fourth institution (I4)	
	ESDa, mGy	AGDa, mGy	ESDa, mGy	AGDa, mGy	ESDa, mGy	AGDa, mGy	ESDa, mGy	AGDa, mGy
2,5	2,898	0,996	-	-	5,844	2,000	2,453	0,840
3	3,029	0,885	-	-	7,439	2,173	-	-
3,5	5,183	1,384	16,906	4,048	7,402	1,977	3,319	0,886
4	4,777	1,336	17,462	4,181	10,386	2,754	4,531	1,201
4,5	6,426	1,506	6,649	1,378	11,57	2,849	3,859	0,950
5	8,853	1,601	13,795	2,859	15,748	3,264	11,334	2,349
5,5	10,700	1,966	11,281	2,200	19,349	3,774	11,767	2,295
6	10,935	1,986	14,814	2,691	19,653	3,569	11,980	2,176
6,5	15,477	2,661	28,469	4,598	-	-	13,04	2,242
7	17,757	2,868	26,867	4,339	-	-	15,805	2,552
7,5	23,427	3,598	33,015	5,332	-	-	16,637	2,555
8,5	-	-	-	-	-	-	23,621	3,255
9	-	-	-	-	-	-	26,107	3,396

Calculations of AGD were performed assuming that the standard breast consists approximately of 50% adipose and 50% glandular tissue in central region. Since the breast composition is changing with the age, appropriate correction factors related to the compressed breast thickness for each age group of patients was applied.

The distribution of the calculated AGD for CC, and MLO projections for the group of patients are presented in the figures 3 and 4 respectively.

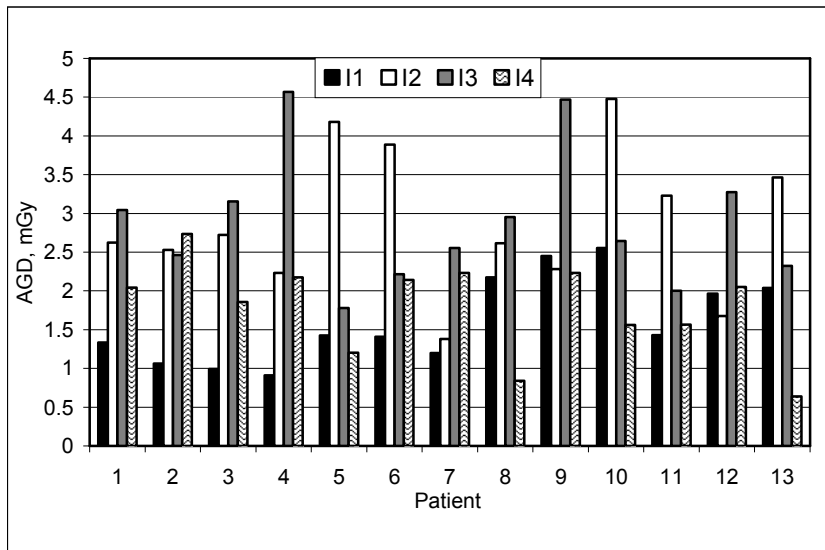


Fig.3. Distribution of the calculated AGD for CC projection among the group of patients

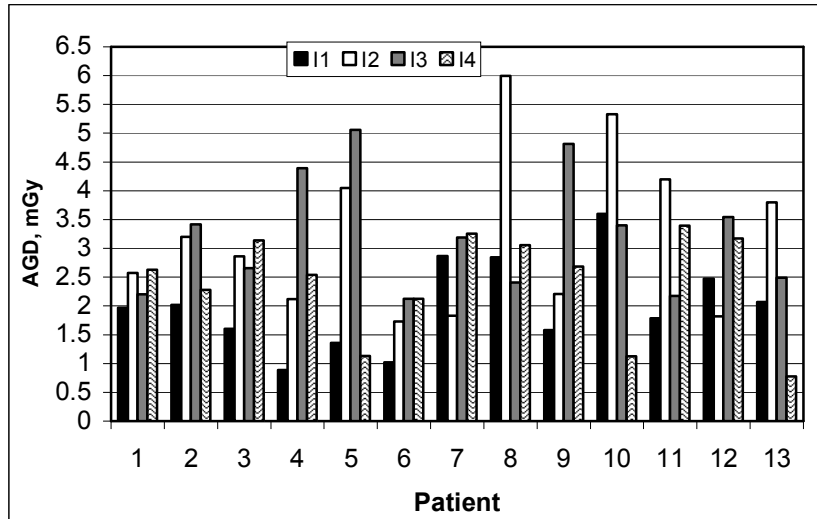


Fig.4. Distribution of the calculated AGD for MLO projection among the group of patients

AGD values evaluated from single measured entrance surface doses for different projections are in some cases higher than the reference dose level of 3.2 mGy per exposure, however the averaged AGD values vary with the breast thickness but are not exceed the dose limit. AGD values for the different compressed breast thickness for CC and MLO projections in one of the institutions are compared in the figure 5.

As it is stated in the different protocols, the standard breast consists on average of 50% of adipose and 50 % of glandular tissue [8]. Our previous investigation [9], based on the mammogram's evaluation, showed that 5.5 cm thick compressed breast mostly fit to the "standard breast" definition. In this investigation we have not made any consideration about the standard breast thickness, so the AGD values for the commonly used "standard breasts" are presented in the Table 5.

Table 5. The AGDa values for the "standard breasts"

d, cm	AGDa, mGy			
	First institution (I1)	Second institution (I2)	Third institution (I3)	Fourth institution (I4)
4,5	1,506	1,378	2,849	0,950
5	1,601	2,859	3,264	2,349
5,5	1,966	2,200	3,774	2,295

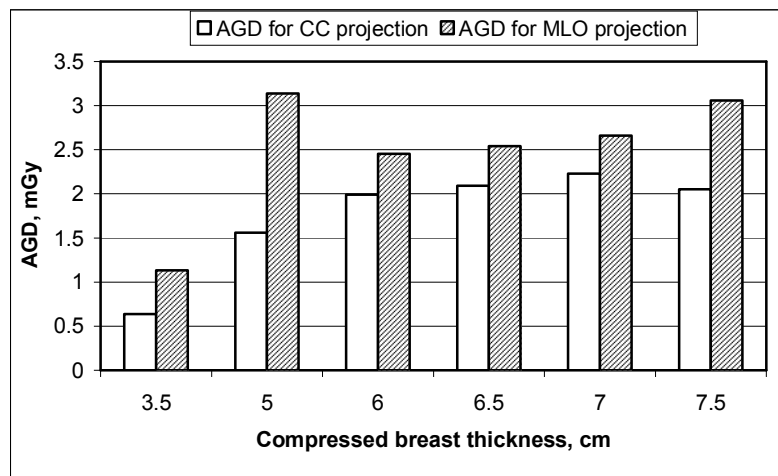


Fig.5. AGD values for two different exposure projections

Conclusions:

TLD *in vivo* method is of the value in applications directed to the patient's dose evaluation during mammography screening examinations. Estimated doses reflect the dependency on the breast composition and density. However this method can not be suggested for the routine mammography examinations because of the occurring problems which influence entrance surface dose. Since the TLDs are positioned on the breast surface before the examination and the breast is moved, it is very difficult to keep the same reference point for the dosimeter during different examinations, even if the person performing examination is the same.

The calculated average AGD in most cases did not exceed European reference level. In two institutions the average diagnostic dose reference level was higher than 3 mGy for the breast glandular tissue during single CC mammography exposure with grid. 3 mGy is a reference level for mammography in Lithuania according to the Lithuanian HN 31:2002 „Radiation protection and safety in medical X-ray diagnostic practice“. The tendency of increased doses is evident when thicker breasts are exposed. Different authors recommend to use Mo/Rh anode-filter combination for the dense and thick breasts but no one change of the filter was undertaken during this investigation. The constancy tests performed for mammography unit “Alpha RT” showed, that the usage of Rh filter instead Mo during the exposure of 6 cm thick PMMA phantom (the same kVp, the same optical density on the film as in the case with Mo filter), resulted mAs value decreased by factor of 1.5.

Acknowledgement

Authors would like to thank all colleagues in different hospitals, who helped us to perform these measurements.

References

1. http://www.is.lt/cancer_reg/moterys/MSL2005.html;
2. John Saunderson. Radiation protection for assistant practitioners in mammography.
3. M.C. Aznar. Real-time *in vivo* luminescence dosimetry in radiotherapy and mammography using Al₂O₃:C. Riso national Laboratory, Roskilde, Denmark. 2005.
4. European protocol on dosimetry in mammography. EUR 16263EN. ISBN 92-827-7289-6. Luxemburg.
5. D. Dance, C. Skinner, K. Young, J. Beckert, C. Kotre. Additional factors for the estimation of mean glandular breast dose using UK mammography dosimetry protocol. Phys.Med.Biol. 45, 3225-3240 (2000).
6. D.R. Dance, C.L. Skinner, G. Alm Carlsson. Breast dosimetry. Applied Radiation and isotopes 50 (1999) 185-203.
7. <http://rpop.iaea.org>.
8. Keith Faulkner. RC-4a Screening Mammography including quality assurance. International radiation protection association 11'th international congress, Madrid. 2004.
9. D. Adliene, G. Adly, R. Cerepaite, E. Jonaitiene, I. Cibulskaitė. Optimization of the X-ray examinations in Lithuania: start of the implementation in mammography. RadiationProtection Dosimetry (2005), V114, No1-3, p.399-402

The work is supported by Lithuanian State Science and Studies Foundation

TOWARDS OPTIMIZATION OF THE PATIENT'S DOSES IN MAMMOGRAPHY IN LITHUANIA

I. Cibulskaitė^{1,2}, J. Laurikaitienė^{1,2}, M. Šniurevičiūtė^{1,2}, E. Jonaitienė², B. Gricienė³,
G. Adlys¹, R. Kabaila¹, S. Raila¹, S. Mattsson⁴, D. Adlienė¹

¹Kaunas University of Technology,

²Kaunas Medical University Hospital,

³Radiation Protection centre,

⁵Malmö University Hospital

Abstract

Influence of physical, geometrical and technical parameters to the doses of patients during mammography screening examinations in Lithuania have been investigated. Some results of *in vivo* TLD measurements of the patient's breast entrance surface doses of are presented in this paper together with the results of *in vitro* measurements, performed using different phantoms and with the results of Monte Carlo modelling are presented in this paper. It is shown, that among the usual problems of the breast dosimetry, attention has to be paid for the investigation of the point skin doses on the breast surface during the whole mammography screening examination, which includes 4 exposures.

Key words: *thermoluminescence dosimeters, entrance surface dose, average glandular dose.*

Introduction

Mammography screening program in Lithuania has been started in September 2005. It is addressed to the women in the age of 50-69 years, the number of whose according the database of health care institutions is ~413200 in Lithuania. It is planned to apply breast screening procedure to 60% of all mentioned women during 5 years. 14 mammography screening centres were involved in this project (4 centres in Vilnius, 4 centres in Kaunas, 1 centre in each of hospitals in Klaipėda, Šiauliai, Panevėžys, Alytus, Marijampolė and Utena) in 2005. 11 of these centres are continuing this work in 2006.

4 mammography X-ray examinations (Cranio-Caudal (CC) projection, Medio-Lateral-Oblique (MLO) for each breast of the patient) are planned for the screening procedure. 2 independent radiologists-reviewers evaluate mammograms according the standard BI-RADS evaluation system.

The efficiency of the screening program was not that good as expected, because only ~31000 women were examined (91.3% of total number which was planned). The main factor influencing this figure is not a small number of screening equipment, but rather the minimal number of radiologists-evaluators. Due to the lack of high professionally skilled radiologists, it was not possible to continue the screening program in three institutions. Another problem of this project is that the screening examinations are carried out parallel to diagnostic examinations: such praxis limits the number of mammography screening examinations. Due to this reason the efficiency of mammography screening program is relative lower in the big medical centres: in Vilnius (47%) and in Kaunas (60%), as compared, for example, with "Salvija Medical Centre" in Klaipėda (119%), where in fact only screening examinations are undertaken.

The quality of mammography examinations is steadily checked and the quality assurance programs are installed in all working centres according to the requirements of Lithuanian HN-94-2004.

Parallel to the screening program the investigation of patient's doses during mammography examinations was started. The aim of this work is to present some results of this investigation, which have been obtained in different hospitals of Lithuania with the purpose to identify the problems in mammography screening examinations and implement patient's dose optimization measures on base of it.

Instruments and methods

The dose to the breast of an individual patient is determination of three main factors:

- The characteristics of the equipment being used;
- Technique factors selected for the examination;
- Size and density of the patient's breast.

Present investigation has been conducted with the respect to the breast dose influencing factors mentioned above. Investigation of patient's doses during mammography screening examinations has been carried out during 2005-2006 in 6 hospitals of Lithuania and the results compared with those obtained from the measurements in 2003-2004 [1].

Randomly selected groups consisting of 13-20 patients of different age and with different breast density and size were chosen for each investigation. Mammography units Instrumentarium ALFA RT and MAMMOMAT 100 (SIEMENS) with grid, Mo/Mo anode and filter combination; Kodak Min-RD, Cawo Mammo R200 film cassettes and Kodak X-Omat, Konica Minolta films were used for the screening procedure. Entrance surface

doses to patients breast were measured using LiF:Mn,Ti TLD dosimeters: pellets with a size of (3.2x3.2x0.9) mm³, calibrated and red out using a Harshaw TLD5500 (Harshaw Bicron Radiation measurement products, Ohio, US) at the Department of medical Radiation Physics at Malmö University Hospital and tablets of Ø5mm, which were calibrated at the SSL in Latvia and red out using Rados TLD system at Lithuanian Radiation Protection Centre. Depending on the type of the investigation 1 – 4 dosimeters were placed on the breast surface at the reference point (central position, upper quadrant of the breast/phantom, 5-6 cm distance from the “chest wall”).

Dose measurements *in vitro* were performed using TLDs and semiconductor (Si) devices together with different phantoms: RMI 256, PMMA phantom of different thickness and real sized and shaped silicon gel breast phantom (Elastosil 7616 with Elastosil W1,Wacker Chemie GmbH, produced by JSC “PLĒTRA”, Kaunas, Lithuania). Additionally, simulations of the X-ray spectrum for Mo/Mo target –filter combination and doses for different exposure conditions, geometry and experimental set up were made using computer codes IPEM 87 and EGSnrc respectively.

Results and discussions

Using mammography unit with an automatic exposure control (AEC) device, it automatically controls technical factors (selection of target material, focal spot, filter material, exposure time, X-ray tube voltage and tube output) in order to obtain a desired quantity of radiation at a pre-selected location.

The X-ray tube voltage is one of the most important parameters that provides the optimum balance between image formation and absorbed dose. It depends on the compressed size and the density of the breast. Entrance surface dose dependency upon the X-ray tube voltage for the constant breast thickness is presented in Fig.1

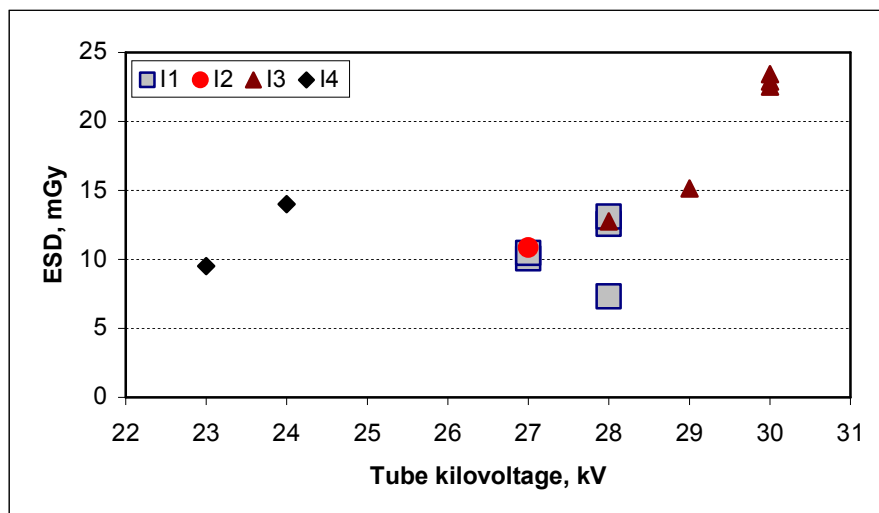


Fig.1. Entrance surface dose for the 5.5 mm thick compressed breast exposed in CC radiography projection, when AEC is used

Higher tube voltage usually means the reduced dose, nevertheless it is to assume, that even applying AEC, the tube voltage can vary within the whole range of mammography examinations, as it is shown in Fig.1. guidelines regarding the use of kV settings should also include an image quality checks. Modifying tube potential (kVp) an increase in kVp with increasing breast thickness can cause a net reduction in breast dose for constant film dose, but expense of degradation in image contrast owing to the diminishing differential tissue absorption.

An exposure technique of a constant kVp and variable mAs to maintain a fixed image receptor dose results in the breast dose increasing approximately exponentially with compressed breast thickness (Fig.2)

There is no optimal value known for the compression force, but attention to the applied compression and accuracy of the indication is required, because the compressed breast thickness is directly proportional to the compressing force. Variations of the entrance surface doses for the 5.5 mm compressed breast thickness during mammography examination (CC radiography projection) in different medical institutions are presented in the Fig. 3.

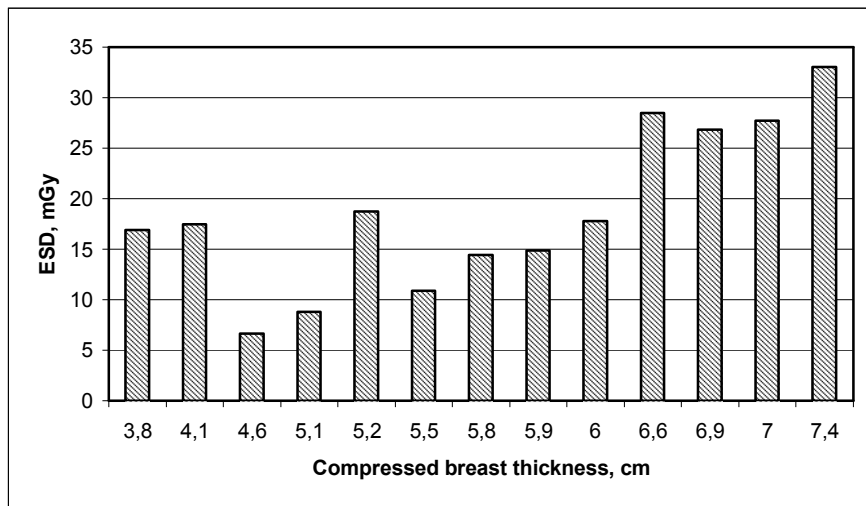


Fig.2. Dependence of ESD on the compressed breast thickness at 27 kVp.in the institution I2

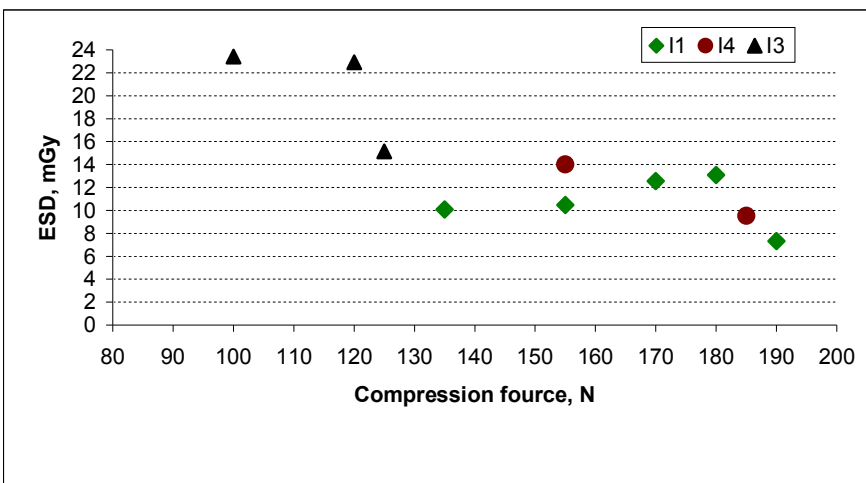


Fig. 3. Dependence of ESD on the compression force for the constant compressed breast thickness (CC radiographic projection)

Estimation of the influence of all possible parameters is necessary if a scenario for the dose optimization during X-ray mammography screening examinations of patients has to be prepared. However it is to point out, that only recommendations without follow up do not give expected result. Comparing the results of measurements carried out in 2003-2004 it is to point out, that there were no improvement towards optimization in some hospitals (Fig.4) during the last time.

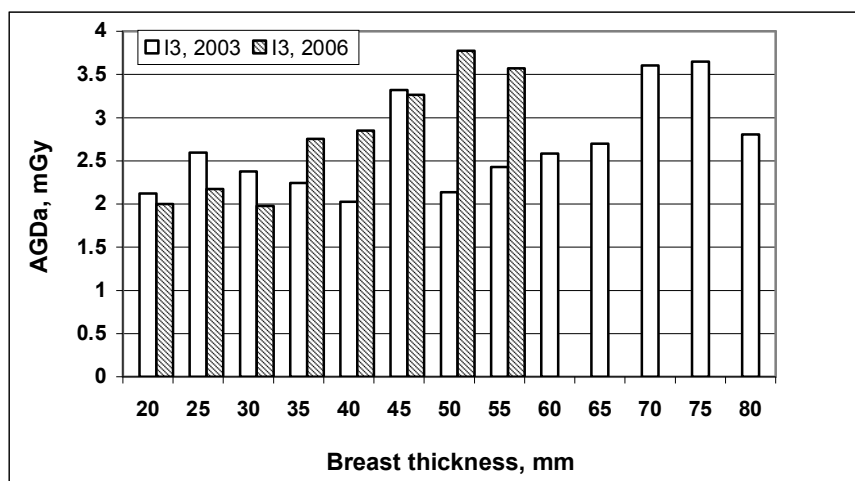


Fig. 4. Comparison of the measurement results, performed in the same institution in 2003 and 2006

Another very important problem in mammography screening of patients is the dose absorbed at the reference point during all exposures (CC and MLO projections for both breasts). Applying the multiple TLD dosimetry

method it was found, that the skin dose to the patients breast during single exposure is equals only to 47% of the total dose received during the whole examination and equals 51% of the dose, when only two exposures (CC and MLO for one breast) are performed (Fig.5.).

Installing TLD dose mapping technique and Monte Carlo simulations for the phantom measurements the breast areas of the highest doses were determined as it is indicated in Fig.6 and Fig.7.

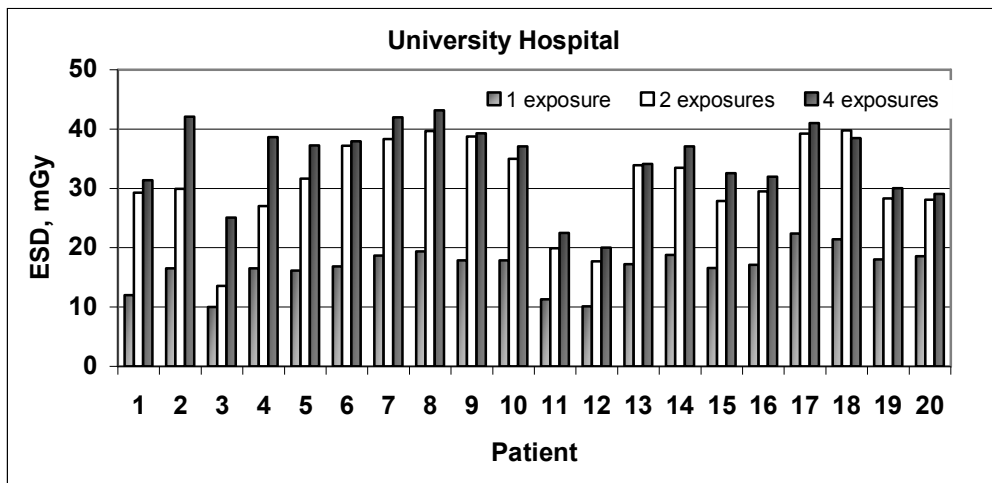


Fig.5. Entrance surface doses for single exposure, 2 and 4 exposures of the patient during mammography examinations.

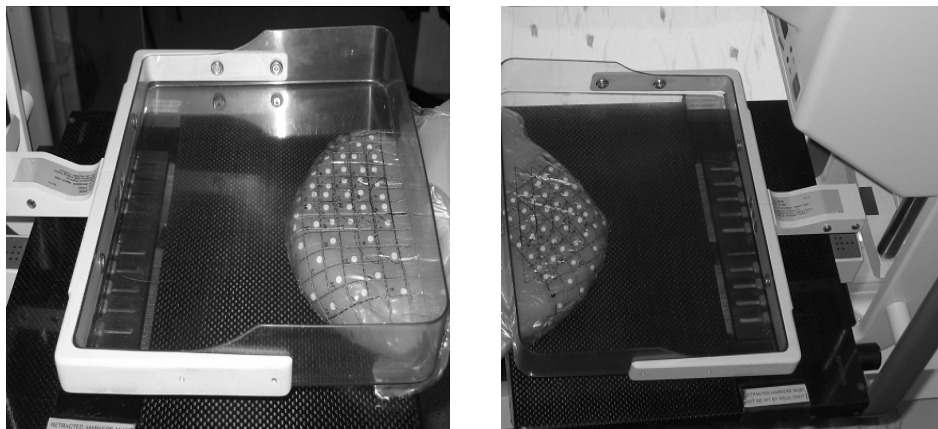


Fig. 6. Photographs of the compressed silicon gel phantom with TLDs on it during dose mapping experiment

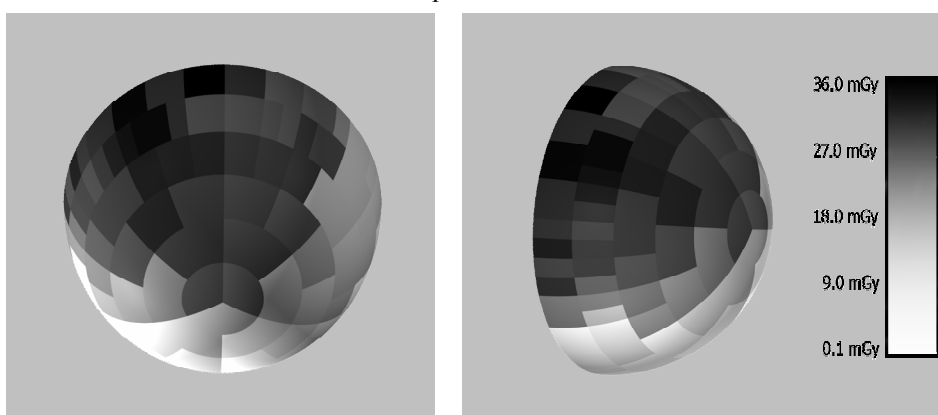


Fig.7. Modelled ESD dose distribution on the breast phantom (breast shape was approximated to the sphere)
References

1. D. Adliene, G. Adly, R. Cerapaitė, E. Jonaičiūtė, I. Cibulskaitė. Optimization of the X-ray examinations in Lithuania: start of the implementation in mammography.- Radiation Protection Dosimetry (2005), V114, No 1-3 , p.399-402

This work is supported by the Lithuanian State Science and Studies Foundation

ENTRANCE SURFACE DOSE MEASUREMENTS WITH THERMOLUMINESCENCE DOSIMETERS AND TRANSMISSION IONIZATION CHAMBER

Viktorija Burinskienė, Marius Laurikaitis, Diana Adlienė

Kaunas University of Technology, Physics Department, Studentų g. 50, LT – 51368 Kaunas, Lithuania
e-mail: viktorija.sapokaite@stud.ktu.lt

Abstract

Some differences in the evaluated dose values may occur when different techniques and methods are used for the dose measurements during X-ray examinations of patients. The results of the evaluated entrance surface doses (ESD) derived from the results of measurements using thermoluminescence dosimeters (TLD) and transmission ionization chamber – dose area product (DAP)-meter are presented in this paper. Uncertainties caused by the different dose registration methods are discussed on basis of comparative analysis.

Key words: dose area product (DAP), thermoluminescence dosimeter (TLD), entrance surface dose.

Introduction

Absorbed dose in radiology is the main parameter which is used for the assessment of radiation risk. However it is not possible to measure directly absorbed dose. It is calculated from measured entrance surface dose, which can be measured in different ways, using different registration technique. Entrance surface dose is the absorbed skin dose of the patient, which includes backscatter radiation from the patient. ESD is suitable and comparable parameter for the assessment of radiation impact on patient using different registration techniques during X-ray examinations; however measured dose values are slightly dependent on the method of investigation. The aim of this work was to compare entrance surface dose evaluated from TLD measurements and measurements, performed using DAP meter and to discuss the uncertainties caused by the choice of registration method.

Instruments and methods

Investigation of patient's doses during X-ray examination of pelvis, chest and lumbar spine was performed using TLD technique and DAP-meter.

Calibrated LiF:Mg,Ti dosimeters were placed on the patient's skin at the central position of the X-ray exposure field. Entrance surface dose (ESD_{TLD}), which includes backscattering factor from the patient, was measured. Reading of exposed TLD's was performed using Harshaw TLD 5500 system at Lithuanian Radiation Protection Centre.

DAP-meter "Diamenter 4" (PTW, Freiburg) was installed just beyond the X-ray tube collimators and was used for the measurements of the absorbed dose to air, during the same X-ray examinations. The reading of DAP-meter during the examination expressed as dose-exposed area - product revealed to the total amount of the X-ray energy delivered to the patient which was related to the absorbed dose. Entrance surface doses ESD_{DAP} were calculated by the formula using measured DAP values:

$$ESD_{DAP} = \frac{\lambda \cdot DAP_{read} \cdot d_{ff}^2 \cdot \sigma}{S \cdot d_{fs}^2}, \quad (1)$$

where λ is the calibration coefficient for DAP meter; DAP_{read} is the reading of DAP meter; d_{ff} is the focus-to-film distance used during the examination; σ is the backscatter factor; S is the exposure field size; d_{fs} is the focus-to-skin distance.

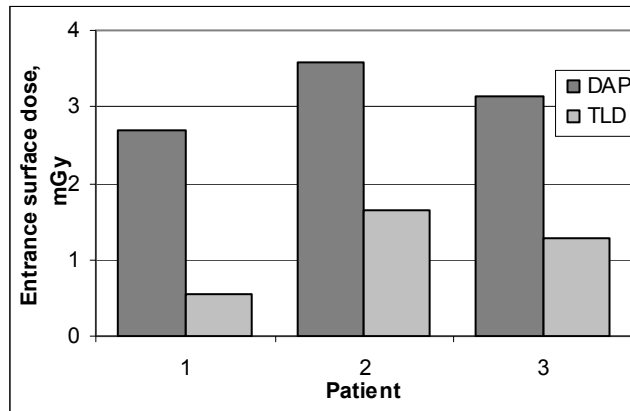
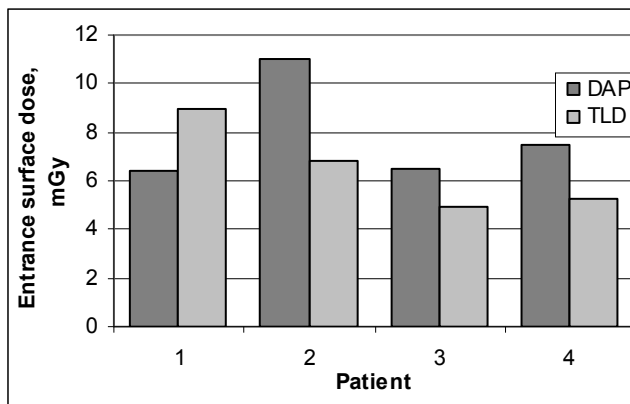
Results and discussion

Measured ESD_{TLD} and calculated ESD_{DAP} entrance surface doses of patients during different X-ray examinations are presented in the Table 1 together with the exposure and other relevant parameters.

Table 1. Measured and calculated entrance surface doses

TLD No	1.	2.	3.	4.	5.	6.	7.	8.
Gender M/F	M	M	M	F	M	F	M	M
d_{fs} , m	0,74	0,78	0,78	0,81	0,75	0,75	0,77	0,66
Cassette	35x35	35x35	35x35	35x40	35x40	18x43	30x40	35x40
kV	83	91	83	76	69	63	76	91
mA	250	250	250	250	250	250	250	250
s	0,16	0,16	0,16	0,40	0,40	0,4	0,32	0,5
mAs	40	40	40	100	100	100	80	125
DAP_{read} , μGym^2	132,5	195,88	170,35	431,94	634,96	206,27	387,03	594,63
ESD_{DAP} , mGy	2,70	3,59	3,13	6,43	11,03	6,48	7,44	13,34
ESD_{TLD} , mGy	0,7	1,65	1,29	9	6,8	4,9	5,3	13,4
Examination	Chest	Chest	Chest	Pelvis	Pelvis	Pelvis	Pelvis	Spine
Projection	AP	AP	AP	AP	AP	AP	AP	AP

Comparison of measured and calculated entrance surface doses during chest and pelvis examinations are shown in Fig. 1 and Fig. 2.

Fig. 1. Comparison of measured ESD_{TLD} and calculated ESD_{DAP} during X-ray examination of chestFig. 2. . Comparison of measured ESD_{TLD} and calculated ESD_{DAP} during X-ray examination of pelvis

Since the ESD values are dependent on X-ray tube voltage and current, filtration, focus to skin distance, exposure field size and patient's parameters, each of these parameters contribute to the uncertainty of the calculated dose.

Disagreement between ESD_{DAP} and ESD_{TLD} may occur due to the estimation uncertainty of backscatter factor and calibration factor for DAP-meter for different exposure conditions, which are used for the calculations of the dose, or position dependency of the TLD's during the X-ray examination, since they are reflecting the dose at the point of exposure field.

Keeping the tube current constant during all examinations it is possible to reduce the uncertainty from one parameter. However constancy of the X-ray tube current leads to the increased influence of tube voltage as it is shown in Fig. 3 and Fig. 4.

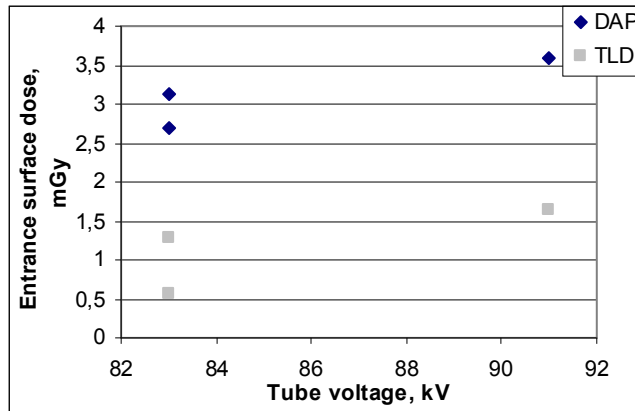


Fig. 3. Entrance surface doses versus X-ray tube voltage during chest examinations

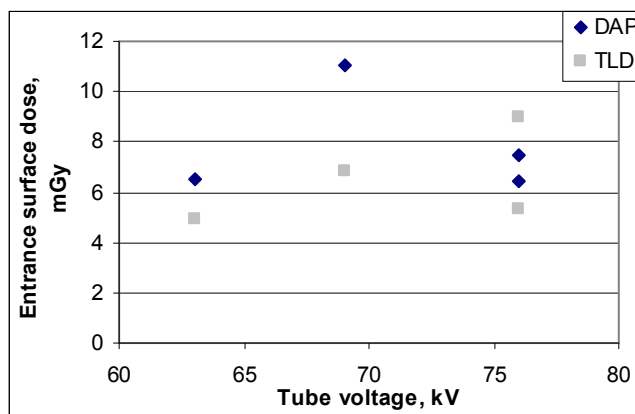


Fig. 4. Entrance surface doses versus X-ray tube voltage during pelvis examinations

Measured ESD_{TLD} and calculated ESD_{DAP} are spread over the interval of about 2 mGy for chest (Fig. 3) and about 4 mGy for pelvis (Fig. 4) examinations.

The best agreement between calculated and measured doses was achieved for the longer duration of exposure (spine examination).

References

- Kepler K., Lintrop M, Servomaa A., Filippova I., Parviaisen T. Dosimetry in radiation dose measurement of paediatric patients in Estonia, Training centre of medical physics and biomedical engineering, 2002. 4 p.
- A. Kettunen. Academic dissertation: Radiation dose and radiation risk to foetuses and newborns during X-ray examination, University of Oulu, 2004.
- E. Yakoumakis, I. A. Tsalavoutas, D. Nikolaou, I. Nazos, E. Koulestantinos, Ch. Proukakis. Differences in effective dose estimation from dose-area product and entrance surface dose measurements in intravenous urography, The British Journal of Radiology, 2001, 8 p.
- Robert A. Parry, Sharon A. Glaze, Benjamin R. Arher. Typical Patient Radiation Doses in Diagnostic Radiology, Imaging & Therapeutic Technology, 1999. 14 p.
- Mihkel Kerikmae. Some luminescent materials for dosimetric applications and physical research, Tartu, 2004. 56 p.

This work was supported by the Lithuanian State and Science Foundation

THE USE OF DIGITAL METHODS IN MEDICAL X-RAY DIAGNOSTICS

J. Siaurys, G. Adlys

Kaunas University of Technology, Studentų g. 50, LT - 51368 Kaunas, LITHUANIA
siauryz@gmail.com

Abstract

Films and film screen systems were only one method used in X-ray diagnostics for a long time. A numerous technological advancements have been achieved in the field of radiology with the introduction of the new methods and technologies, based on indirect and direct digital methods during the last few decades. Comparative analysis of photographic and digital methods in X-ray diagnostic is presented in this paper

Key words: *X-ray radiology, photographic method, digital methods*

Photographic and digital methods

Conventional radiology is based on plain films and long time has had practically no reliance on computer technologies.

The sensitivity of X-ray film to the direct X-ray exposure is low. Therefore it is desirable to use a more efficient imaging detector to prevent patient from unnecessary high doses. This is accomplished by converting the X-ray image into light by means of a scintillating screen (X-ray intensifying screen) and recording visible photons on film. The screen absorbs a large fraction of incident X-rays and also provides signal amplification.

The way to enhance the capability of the conventional radiology is to digitize the images and to create the possibility of image manipulating in electronic format. There are two ways to obtain digital images: computed radiography (CR) and digital radiography (DR).

Computed radiography (CR) is dependent on the use of phosphor-based plates. After exposure to X-rays, these plates are inserted into a CR reader and energized with a laser beam, causing light flashes that correspond to the energy imparted by the X-rays that struck the plate. Light flashes are recorded, turned into electrical impulses, and translated into electronic images.

In digital radiography a digital imaging detector forms the two-dimensional distribution of radiation field, transmitted through the part of the body in discrete special units (pixels) and discrete signal units (bits). In direct system the photons are directly converted into electrical charges inside the detector. In the case of the indirect system the photons are directly converted to the light and then the light is converted to the electrical charges. Silicon is an excellent sensor of visible light but it is a poor absorber so it is not suitable as a direct X-ray sensor. Coating amorphous silicon with a highly absorbing scintillating layer, for example CsI(Tl), activates it to X-ray sensing. Each X-ray photon, absorbed within the scintillating layer, generates a spark of visible light (scintillation) that is detected by the silicon sensor (Fig.1). The sensor converts the light into electric signal and transmits it to a computer.

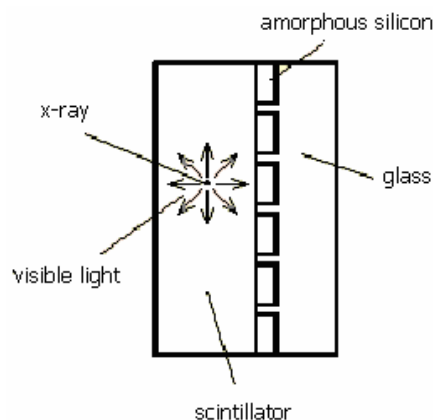


Fig. 1. X-ray imaging scintillation sensor [1]

The main task for the radiologist is to see the difference in image signal between a region of a suspected abnormality and a normal region. This difference is reflected by the radiographic contrast of the image.

Standard method to represent the response of the film to radiation is determination of the relationship between optical density D, equation (1), and X-ray exposure E – the characteristic curve of the film (Fig 2).

$$D = -\log \frac{I}{I_0} \quad (1)$$

where I_0 is incident light and I – transmitted light

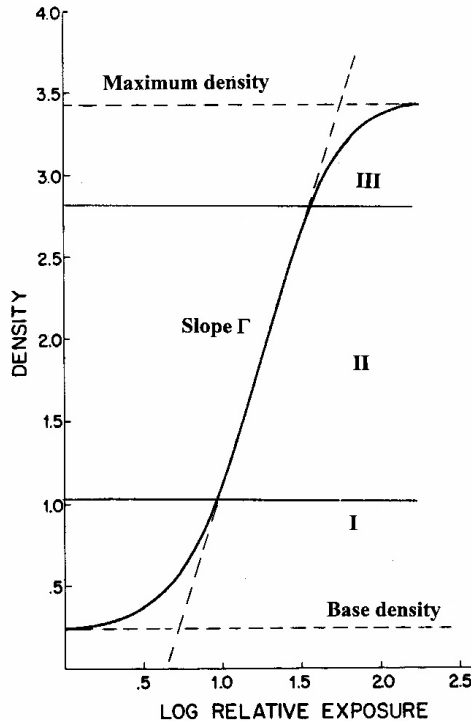


Fig. 2. Typical characteristic curve of the film

According to simple physical model [2]

$$D = D_{\max} \left(1 - e^{-kE}\right)$$

where k is a sensitivity.

The baseline ($D \approx 0.2$) accounts minimum density caused by the developed grains of an unexposed film. The straight-line part of the curve defines film latitude. The third part corresponds to the large exposures. It leads to a saturation of the D signal. Three images corresponding to I, II and III sectors of characteristic curve (unexposed, optimal and large exposed.) are shown in Figure 3 [3].

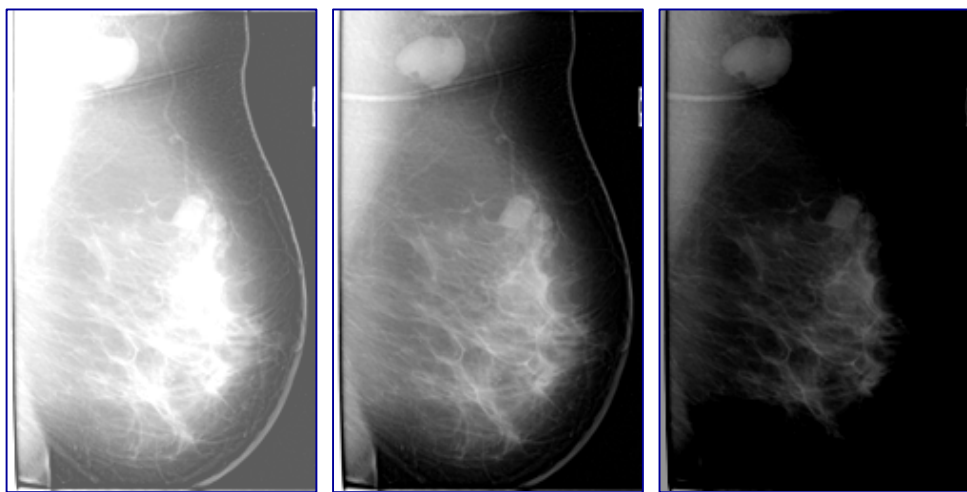


Fig. 3. Underexposed, correctly exposed and overexposed images [3]

The response curve of film is sigmoidal, but response curve of digital detector is straight line (Fig .4). The slope of the characteristic curve expresses the film contrast. Corresponding value on exposition axis is film latitude or dynamic range. The higher contrast film has narrower latitude. There is no way to get wide latitude with high-contrast film. This means, that contrast and latitude (dynamic range) of the film should be closely

matched to the application during radiological examination [2]. A screen-film system has a dynamic range approximately $10^{1.5}$ while detectors in digital radiography have a dynamic range of 10^4 (from 1 to 10.000).

The film constant Γ is defined as:

$$\Gamma = \frac{\Delta D}{\Delta \log(E/E_0)} \quad (2)$$

The gradient of the characteristic curve is not constant and the instantaneous slope, or "point gamma" is also defined as

$$\Gamma = \frac{dI/I}{dE/E} \quad (3)$$

dE/E is the exposure contrast, corresponding to subject contrast (the contrast between two areas of the radiological image; dI/I is the brightness contrast, corresponding the radiographic contrast (the contrast between two areas on a processed film). The point gamma is a contrast gain factor. Film contrast represents the ability of the film to translate subject contrast into radiographic contrast [2].

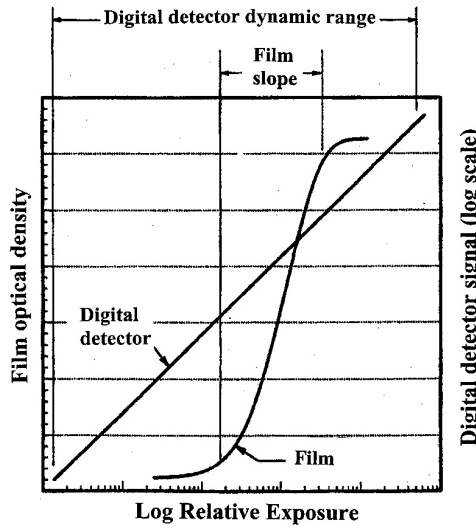


Fig. 4. The response curve of the film and a digital detector

The fundamental limitation to the image information content is statistical noise. Objects are perceived on the basis of their size, shape, and contrast relative to their surroundings. The noise decreases possibility to perceive detail and contrast in an image. It is especially important for cases, when number of gamma or X-ray photons is limited with the aim to minimize radiation dose to the patient. The detectability of small or subtle structures in a radiological image is ultimately dependent on the recorded X-ray quanta. The basic theory of image signal detection is known as the „Rose model“. A. Rose was first who introduced a statistical analysis in the calculation of the minimum detectable contrast. According to Rose model, the contrast C is defined by normalizing the signal to the background counts with the following formula [4]:

$$C = (T - B)/B = S/B \quad (4)$$

The signal S is equal to the difference between the counts T in the target area and the counts B in the background area:

$$S = T - B = C \cdot B \quad (5)$$

According to (5) the signal could alternatively be defined in terms of contrast. The noise N in the image follows Poisson statistics: $N = \sqrt{B}$.

In the case of low contrast, the difference between T and B is low and the square root of B is approximately the same as the square root of T . Then the signal-to-noise ratio K for imaging system:

$$K = C \cdot B / \sqrt{B} = C \cdot \sqrt{B} \quad (6)$$

If Φ is the number of gamma ray photons per unit area (the photon fluence) and A is the area of the region of interest, than $\sqrt{B} = \sqrt{\Phi \cdot A}$ and signal-to-noise ratio K is

$$K = C \cdot \sqrt{\Phi \cdot A} \quad (7)$$

Φ represents the number of counts per unit area and is the definition of an information density. Equation (7) describes the Rose model. It states that the signal-to-noise ratio depends on image contrast, object size, and

information density. The information density is dependent on the matrix size, and a doubling of matrix size reduces the information density by a factor of four if other image acquisition parameters are held constant [4].

The range $K = 5 \div 7$ represents some minimum signal-to-noise ratio that is required to distinguish between a low-contrast object and a noisy background. If K is fixed to set some minimum detectable object contrast, the factors C , Φ , and A are all responsible for an object being perceived. If contrast C is low, the object must be large (a large A) or the number of photons used to evaluate the object must be large for the object to be perceived. Hence, there is a trade-off between contrast C , noise Φ , and resolution A . To improve any one of these factors, others must be negatively affected for minimum object detectability to be retained.

The goodness of the digital radiographic technique used is characterized by exposure level index which expresses the dose level received at the digital detector [5]. The relation between dose and exposure level is usually logarithmic: doubling the dose to the detector, will increase the exposure level to a factor of $0.3 = \log(2)$

Digital radiographic system DRS Universal

X-rays are a form of energy which do not fall within the visible light spectrum, and must first be converted to the light in order to be recorded in either digital or analog form. Common used materials used as the scintillators are: NaI(Tl), CsI(Tl), CsI(Na), CsI(pure). Digital radiographic system DRS Universal has a highly sensitive linear array of semiconductor scintillation detectors of CsI(Tl).

The main features of the digital radiographic system DRS Universal are:

- scanning the patient with very narrow (less than 2 mm) X-ray beam formed by the a proprietary slot collimator;
- utilization of a highly sensitive, patented linear array of semiconductor scintillation detectors;
- x-ray image acquisition by precise step-by-step scanning by means of a linear detector, the motion of which is synchronized with the scanning x-ray beam;
- formation of a two-dimensional digital image, one of the coordinates of which is completely determined by the number of elements in the detector of the number of scanning steps (number of readings) [6].

The most important advantage of DSR Universal is the high contrast resolution of the digital scanning receivers. The determining contribution to the contrast resolution (up to 25 % and higher) is made by the scattered radiation from the patient as well as the interference between the adjacent x-ray-sensitive elements [6].

Because cesium-iodide is an excellent absorber of x-rays, and converts them to visible light photons at energies that amorphous silicon is best able to convert to charge carriers, the combination of these two materials has the highest-rated Detective Quantum Efficiency (DQE) in use today. A high DQE rating means that superior images can be obtained with low dosages of X rays [7].

The linear array X-ray detector consists of separate folding matrices which can be replaced in case of failure of even a single element. The contrast resolution is one of the most important characteristics of digital X-ray image receivers.

Advantages and limitations of the system:

- The wider dynamic range of the digital detectors and the capabilities of post processing allow obtain more information from the radiographic images;
- Easy improvement of image quality,
but
- Conventional films allow detect mistakes if a wrong radiographic technique is used: images are too white or too black;
- Overexposure yields good images with unnecessary high dose to the patient. Over range of digitiser may result in uniformly black area with potential loss of information. Underexposure results in a “noisy” image;
- There is a direct link between diagnostic information (number of images and quality of the images) and patient dose

Digital technique allows producing very easily a great number of images (since there is no need to introduce cassettes or film changers as in the analogical systems). As a consequence of that: dose to the patient is likely to increase without any benefit

References

1. Uri Lachish. The role of semiconductors in digital x-ray medical imaging. 1999 <http://urila.tripod.com/xray.htm>
2. A. Del Guerra. Ionizing Radiation Detectors for Medical Imaging. Singapore. World Scientific Publishing Company. 2004. p.493.
3. IAEA Standard syllabus course on Radiation Protection in diagnostic and interventional radiology. Rpop.iae.org.
4. M. Rzeszotarski. The AAPM/RSNA Physics Tutorial for Residents. Radiographics, September 1, 1999, 19
5. F. Milano. Dosimetry and detectors in radiodiagnosis. Workshop Radiation Protection in medicine. Riga. 2006.
6. V. N. Linev. Role of modern scanning techniques in digital radiodiagnosis. 2004
7. Varian medical systems 2002 annual report. Digital x-ray imaging..

MEDICAL IMAGE QUALITY IMPROVEMENT USING MATLAB ITP SOFTWARE

Leonidas Kryne, Gediminas Dosinas

Kauno technologijos universitetas Studentų g. 50, LT - 51368 Kaunas
gellios@gmail.com

Abstract

Image enhancement techniques and the main parameters influencing digital image quality are overviewed in this paper. The problems of digital X-ray image improvement are indicated and their possible solutions using program package MatLab ITP are discussed.

Key words: *image enhancement, image improvement, program package Matlab.*

Introduction

Medical imaging— production of visual representations of body parts, tissues, or organs, for use in clinical diagnosis; encompasses x-ray methods, magnetic resonance imaging, single-photon-emission and positron-emission tomography, and ultrasound. The quality of medical image plays an important role in medical diagnostic process. Image enhancement processes consist of a collection of techniques that seek to improve the visual appearance of an image or to convert the image to a form better suited for analysis by a human or a machine. There is no general unifying theory of image enhancement at present time, because there is no general standard of image quality that can serve as a design criteria for an image enhancement processor. Consideration is given here to a variety of techniques that have proved themselves as useful for human observation improvement and image analysis.

Methods

Image enhancement techniques can be divided into two broad categories:

- spatial domain methods, which operate directly on pixels;
- frequency domain methods, which operate on the Fourier transform of an image.

Spatial domain methods are procedures that operate directly on pixels composing an image. Spatial domain processes will be denoted by the expression

$$g(x, y) = T[f(x, y)], \quad (1)$$

where $f(x, y)$ is the input image, $g(x, y)$ is the processed image, and T is an operator on f , defined over some neighborhood of (x, y) .

The principal approach in defining a neighborhood about a point (x, y) is to use a square or rectangular subimage area centered at (x, y) . The center of the subimage is moved from pixel to pixel. The operator T is applied at each location (x, y) to yield the output, g , at that location. The process utilizes only the pixels in the area of the image spanned by the neighborhood. Although other neighborhood shapes, such as approximations to a circle, sometimes are used, square and rectangular arrays are by far the most predominant because of their ease of implementation. The simplest form of T is when the neighborhood is of size 1×1 (that is, a single pixel). In this case, g depends only on the value of f at (x, y) , and T becomes a grey-level (also called an intensity or mapping) transformation function that maps a pixel value r into a pixel value s . Intensity transformation functions frequently are written in simplified form as

$$s = T(r), \quad (2)$$

where r denotes the intensity of (x, y) and s the intensity of g , both at any corresponding point in the images.

Grey-level transformation functions are among the simplest of the all image enhancement techniques. These values are related by an expression (2). As an introduction to grey-level transformations, consider Fig.1, which shows three basic types of functions used frequently for image enhancement: linear (negative and identity transformations), logarithmic (log and inverse-log transformations), and power-law (n th power and n th root transformations). The identity function is the trivial case in which the output intensities are identical to the input intensities.

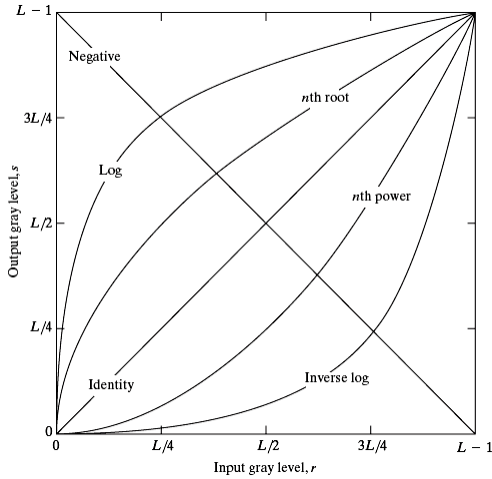


Figure 1. Some basic gray-level transformation functions used for image enhancement.

The negative of an image with gray levels is obtained by using the negative transformation shown in Fig. 1. Reversing the intensity levels of an image using negative transformation produces the equivalent of a photographic negative. This type of processing is particularly suited for enhancing white or gray detail embedded in dark regions of an image, especially when the black areas are dominant in size.

The shape of the *log* curve in Fig.1 shows that this transformation maps a narrow range of low gray-level values in the input image into a wider range of output levels. The opposite is true of higher values of input levels.

$$s = c \cdot \log(1 + r) . \quad (3)$$

This type of transformation could be used to expand the values of dark pixels in an image while compressing the higher-level values. The opposite is true of the inverse log transformation. Any curve having the general shape of the log functions would accomplish this spreading/compressing of gray levels in an image. In fact, the power-law transformations are much more versatile for this purpose than the log transformation. However, the log function has the important characteristic that it compresses the dynamic range of images with large variations in pixel values. A classic illustration of an application in which pixel values have a large dynamic range is the Fourier spectrum with values in the range 0 to 1.5×10^6 .

The general form of the power-law transformations has the basic form;

$$s = c \cdot r^\gamma , \quad (4)$$

where c and γ are positive constants. As in the case of the log transformation, power-law curves with fractional values of γ map a narrow range of dark input values into a wider range of output values, with the opposite being true for higher values of input levels. Unlike the log function, however, here a family of possible transformation curves obtained simply by varying γ could be noticed. As expected, curves generated with values of $\gamma > 1$ have exactly the opposite effect as those generated with values of $\gamma < 1$. A variety of devices used for image capture, printing, and display respond according to a power law. By convention, the exponent in the power-law equation is referred to as gamma. The process used to correct this power-law response phenomena is called gamma correction.

Histograms processing are the basis for numerous spatial domain processing techniques. The histogram of a digital image with gray levels in the range $[0; L-1]$ is a discrete function $h(r_k) = n_k$, where r_k is the k th gray level and n_k is the number of pixels in the image having gray level r_k . Images of different gray level characteristic have different histograms. In the dark image the components of the histogram are concentrated on the low (dark) side of the gray scale. Similarly, the components of the histogram of the bright image are biased toward the high side of the gray scale. An image with low contrast has a histogram that will be narrow and will be centered toward the middle of the gray scale. For a monochrome image this implies a dull, washed-out gray look. Finally the components of the histogram in the high-contrast image cover a broad range of the gray scale and, further, that the distribution of pixels is not too far from uniform, with very few vertical lines being much higher than the others. Intuitively, it is reasonable to conclude that an image, whose pixels tend to occupy the entire range of possible gray levels and, in addition, tend to be distributed uniformly, will have an appearance of high contrast and will exhibit a large variety of gray tones. It is possible to develop a transformation function that can automatically achieve this effect, based only on information available in the histogram of the input image.

The frequency domain is simply the coordinate system spanned by $F(u, v)$ with u and v as frequency variables. This is analogous to the spatial domain, which is the coordinate system spanned by $f(x, y)$, with x and y spatial variables. Using Fourier transformation it is possible to represent each point of image in spatial domain to frequency domain. Frequency domain is used in a wide range of applications, such as image analysis, image filtering, image reconstruction and image compression. Such a filtering is used as lowpass filtering, highpass filtering and high frequency emphasise filtering. It is possible to use spatial and frequency domain in combination to yield result that are superior.

Digital image quality could be improved implementing the results of software simulations and testing of a large set of sample images using suitable program packages. Program package MatLab ITP seems to be promising for solving the problem of medical digital imaging: good image quality and the requirement to keep reasonable low patient's doses during X-ray examination.

References

1. William K. Digital image processing (3rd edition), PixelSoft Inc.,2001, 243-297 p.
2. Rafael C. Gonzalez, Richard E. Woods, Digital Image Processing (2nd edition), Prentice Hall, 2002, 75-215 p.
3. Rafael C. Gonzalez, Richard E. Woods, Steven L. Eddins, Digital image processing using Matlab, Prentice Hall, 2004, 65-140 p.
4. И.С.Грузман, В.С. Киричук, В.П. Косых, Г.И. Перетягин, А.А.Спектор, Цифровая обработка изображений в информационных системах, Учебное пособие, 2000, 22-69 с.

DOES HIGH-PRESSURE CASTOR OIL PHASE TRANSITION CHANGE ITS MEDICAL PROPERTIES

Roland Wiśniewski, Teresa Wilczyńska

Institute of Atomic Energy
05-400 Otwock-Swierk, Poland
roland.wisniewski@gmail.com

Abstract

Properties of the new high-pressure castor oil phase are briefly discussed. Post pressure effects like the anomalous increase of transparency is presented. The possible change of medical properties of castor oil after its pressure treatment is discussed too. The photo of high-pressure castor oil phase, in normal conditions, first time is presented.

Keywords: *castor oil, rapeseed oil, high-pressure, medical problem, light transparency.*

Introduction

Castor oil in medicine. The castor oil plant (*Palma Christi*, *Mexico Seed*, *Mole Beam*, scientific name - *ricinus communis*) is native to India, Africa and Central America and grows wild in most of the tropical and subtropical areas of the world. It was cultivated 6000 years ago by the Egyptians, who used the oil as fuel to burn in their lamps.

It was known to Herodotus [IV-V age BC], who calls it "Kiki" and states that it furnishes an oil much used by Egyptians, in whose ancient tombs, seeds of *Ricinus* were found. Around the 4th century BC, it had already been introduced into Greece where it is cultivated even today under the same ancient name. It was employed medically in Europe during early Middle Age and used externally in skin diseases. In the 18th century, its cultivation in Europe as a medicinal plant had ceased and small supplies of the seeds and oil required for European medicine were obtained from Jamaica. The name "castor" was originally applied to the plant in Jamaica where it is called "Agnus castus".

Castor oil is used in conventional medicine as purgative and laxative (when swallowed) and is used as an eye drop to treat some eye irritation. It is also an ingredient in hair conditioners and skin products.

Many naturopathic practitioners and some others claim that castor oil boosts the immune system by increasing white blood cells (which help the body fight infection) and other immune cells. They also claim that castor oil help dissolve cysts, warts, and tumors as well as soften bunions and corns.

The castor oil has many good external uses. In China it is used as a rub for deformed face and joints. Warm castor oil is used as a rub for arthritis and rheumatism and as a bath oil in relieves many skin problem. In Jamaica is used to cure constipation and bodily pain. The oil applied to wounds will stop bleeding. Hot castor oil massaged into the hair will strengthen it and eliminate dandruff, lice, fleas and other scalp problem. Some time it is used in female problems by making a castor oil pack and placing it over the "troubled area". After some hours the troubles area should be wash with worm water and baking soda to alkalinize the area where toxins have been released.

But we have to say that there have been no scientific studies to support above practices.



Fig. 1. The beauty of *ricinus communis* (internet).

Castor oil in science and technology. Castor oil is widely used in technological problems as liquid of very good lubricant properties, of high but slowly change with pressure viscosity, good pressure transmitting medium and so on. Some years ago the high-pressure castor oil new phase was discovered [1].

About generating and properties of high-pressure castor oil phase (H-PCOP) there have appeared some papers in specialised literature. It concern to discovery of this phase [1], volume changes during phase

transition[2], kinetics properties [3], phase diagram of the normal state castor oil and where is the place on this diagram determining possibility for its obtaining [4], dielectric properties [5], optical properties [6], non Newtonian character of viscosity [7,8,9] and properties of its mixture with methyl alcohol [3].

H-PCOP under normal condition is not stable and therefore was not investigated using common techniques which permit to define, for examples, its mechanical properties, colour, structure and others properties.

New experimental data

Observation H-PCOP at normal condition. Using quick-operated high-pressure apparatus constructed by authors, it was possible to generate high-pressure castor oil phase under controlled process at relative small pressure (400MPa). After rapid demounting of apparatus, by some seconds castor specimen was put out from pressure chamber into small, perfectly cleaned, china tray. Next, by 20-30 seconds at temperatures 22 °C, H-PCOP can be directly observed. Process of its disappearing takes place on free surface of high-pressure phase what is illustrated in photo, see Fig.2.

The colour of H-PCOP like opalescent light-yellow and its mechanical similarity to the beam wax was observed.

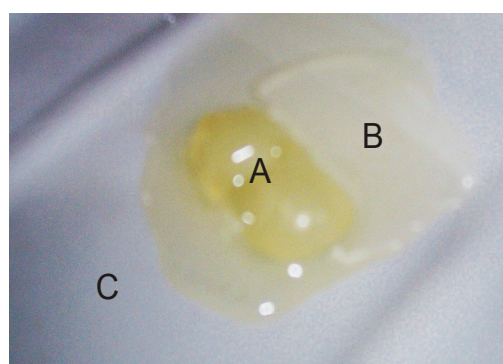


Fig. 2. The photograph of H-PCOP just after it taking out from high pressure apparatus (A), liquid castor oil when high pressure phase is disappeared (B), background china tray (C).

Transparency properties. Liquid state of castor oil after high pressure phase decomposition seemed to be more transparently than those before high-pressure experiment. In that situation an investigation of spectral transparency of castor oil before and after phase transition were curried out. For comparison similar investigation was curried out also with rapeseed oil. The effect of the large increase of spectral transparency of castor oil was observed.

For this investigation the spectrophotometer HP 8453 and program HP UV-Visible Chem. Station Rev.A.02.04a were used.

In Fig. 3 there is shown dependence of spectral transparency in the wave length diapason 300-1100nm. It appears to be by about 30 % higher in wide investigated range of light for castor oil, after phase transition. The decrease of transparency at the beginning of our investigation was expected. Similar phenomenon was observed in the case on rapeseed oil, see Fig. 3. But in this case the increase of transparency was only by about 10% higher, having lower transparency at whole. Also at waves diapason 900-1100nm (under red region) practically no changes in transparency is observed.

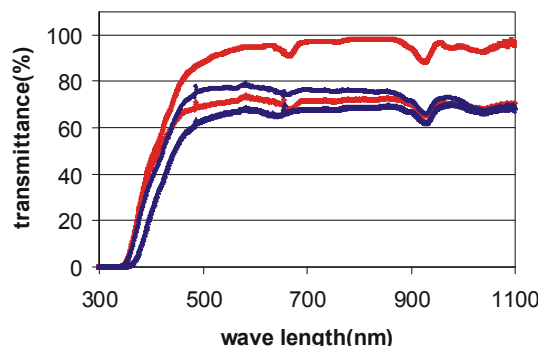


Fig.3. Spectral transparency for castor oil (red curves) and rapeseed oil(blue curves) after (upper curves) and before (lower curves) phase transition at normal conditions.

Chemical changes of castor oil after phase transition. The influence of hydrostatic pressure, so high as 1GPa, on chemical properties of the castor oil should be small or even non. But the question if high-pressure phase transformation have the influence or not on biological properties of castor oil is not trivial one. Since now, except transparency effect, and the small increase of density of $0.6 \pm 0.2\%$ the observed phase transition was to be almost reversible. But authors undertaken the problem if castor oil after phase transition has better or worse the medical properties. So some comparisons of different characteristic depends on structure of castor oil before ad after pressure treatment have bee done. Investigation of castor oil using chromatography methods (GLC, HPLC-RP and HPSEC) gave following results: 1) the are the same fatty acid component before and after phase transition but 2) small changes of it quantitative content was noted. The content of ricinoleic acid degreases by 1% and the rest components slightly increases. Of course we can speak only about tendency. That presents Table 1. The Raman spectral analyses also had shown that all observed molecular constants was practically the same before and after high-pressure phase transition, what was expected. The Nicolet Almega Raman Spectrograph with LD 532 and 780nm was used. Similar behavior we observed in the rapeseed oil Besides this Raman spectral data are almost identical with castor oil spectra.

Table 1 A composition of the castor oil before and after high-pressure phase transition, in weight %.

Castor oil	C16:0	C18:0	C18:1	C18:2
Before	1.63	1.73	4.98	5.94
After	1.70	1.79	5.63	6.10

C18:3	C20:0	C20:1	Ricino-leic acid	Others
0.59	0.07	0.48	83.63	0.95
0.64	0.08	0.52	82.61	0.93

Some about structures. The diagram of fundamental (most probably) structure of castor oil molecules as triglycerides of ricinoleic acid (main component of castor oil) is shown below

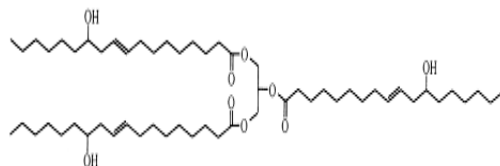


Fig. 4. The basic castor oil molecule.

Ricinoleic acid are replaced in real oil statistically in 4.2% by linoleic acid, in 3.0% by oleic acid (C18:1); in 1.0% by stearic acid (C18:0), in 1.0% by palminic acid (C16:0), in 0.7 % by dihydroxystearic acid, in 0.3% by linolenic (C18:3) acid and in 0.3% by eicosanoic acid.

The molecule of castor oil is rod-type molecule with some bending in double bond places. Structure of castor oil is disordered and random. During high-pressure phase transition a scattering centres of light appears. In fig.5 those scattering centres are shown as yellow elliptical spheres with anti parallel ordering of molecular dipoles (because of decreasing dielectric constant) being in the rest and under high-pressure some space structure takes place, phase became solid. This tixotropic phenomena, in the case of castor oil, was reported first in [7]. Under shear stress H-PCOP became to be a liquid. The authors imagination of described here situation is presenting in Fig.5

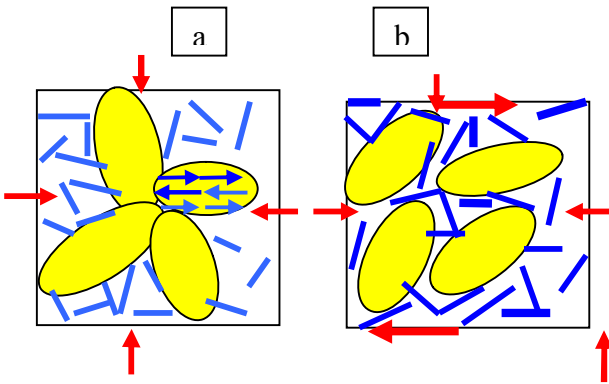


Fig. 5. Proposal for H-PCOP structure. Yellow elements scattering centres with anti parallel ordering of molecular dipoles. Situation after long time stabilization of H-PCOP - a). during shear stress action, - b). in viscous flow for example

Some private medical experiment

For main application of castor for adult the allowed doses of castor oil is teaspoon followed by a glass of fresh squeezed orange juice. The changes of medical properties of castor oil taking under consideration information as above should be not dangerous for personal investigations. The female part of the author staff of this paper who needed such treatment, said after use of castor oil, being previously pressure treatment, that biological action of castor oil was almost the pleasure. Seriously speaking, it is well known that there are some possible problems even complications when castor oil is used. The side effects can include abdominal pain, colic, nausea, vomiting and others. Women, who are pregnant, or breast - feeding should not use castor oil.

Castor beans are extremely poisonous and can kill people or animals if chewed or swallowed.

It is also known super poison, called ricine, which is obtained also from castor seeds and is under secrets service.

Closing remarks

Authors of this paper are in opinion that high-pressure procedure with castor oil can leads to new properties of it. Investigation of any medicine is very serious, dangerous and difficult problem. It have to be performed under proper medical institution, not by us. Chemical and physical analyses has shown that, practically, no changes are observed. The exception is the un normal high increase of spectral transparency what informs us about some serious changes in molecular structure of castor oil, disappearance of scattering centres or so.

Acknowledgement

Authors thanks to prof. K. Wieteska, prof. S. Chwaszczewski for their support. To dr R. Pawłowicz, Gdańsk Politechnika, for chromatography analyses, to prof. W. Fabianowski, Warsaw University of Technology, for Raman spectra and to MS G. Karasiński, Warsaw University, for optics spectra.

By decision of prof. R. Bacewicz, actual dean of Physic Faculty of WUT, supported by Rector - prof. Wł. Kurnik - High Pressure Laboratory directed by one of us by 50 years was closed for us. So in this reason it is only last perhaps our paper devoted to this themes. Sorry.

References

1. R. M. Siegoczyński, J. Jędrzejewski and R. Wiśniewski, High Pressure Res., 1989, **1**, 225-301 p.
2. R. Wiśniewski et.al. High Pressure Res., 1994, **13**, 385-391 p.
3. R. Wiśniewski et al., Bulletin of American Institute of Physics, 229, 1994.
4. R. Wiśniewski et. al., High Pressure in Material Science and Geoscience, Technical University of Brno, 1994, 105-108 p, Brno, Czech Republic.
5. R. Wiśniewski, J. Jędrzejewski and R. M. Siegoczyński, High Pressure Res., 1994, **13**, 41-45 p.
6. R. M. Siegoczyński, R. Wiśniewski and W. Ejchart, Physica B, 265, 1999, 272-276 p.
7. R. Wisniewski, High Temperatures-High Pressures, forecoming papers.
8. R. Wiśniewski and R. M. Siegoczyński, High Pressure Res., **23**, 2003, 211-215 p.
9. R. Wiśniewski R. M. Siegoczyński and A. Rostocki, High Presure Res., **25**, 2005, 63-70p.

AUTHOR INDEX

- Abul-Kasim K. 19
Adlienė D. 61,76,81,85
Adlyš G. 81,88
Andrijaitienė V. 76
Atkočius V. 59
Bäck S. Å. J. 45
Bagdonas S. 16
Baltušnikas A. 59
Boka G. 48
Burinskienė V. 76,85
Burkanas J. M. 12
Christensson J. 45
Cibulskaitė I. 76,81
Dekhtyar Yu. 48
Didžiapetrienė J. 8,12
Dosinas G. 92
Eremenko A. 35
Garnytė E. 76
GnatyukYu, 35
Graželienė G. 8,12
Gricienė B. 59,81
Griškevičius R. 51
Guobienė A. 39
Gustavsson H. 45
Hall H. 19
Jonaitienė E. 81
Juraitis A. 39
Kabaila R. 81
Karlsson A.45
Kepler K. 69
KrylovaG. 35
Krynke L. 92
Lapienis J. 8,12
Laurikaitienė J. 81
Laurikaitis M. 85
Leščiauskas V.59
Lundborg G. 19
Maly P. 19
Månnsson S.45
Mattsson S. 42,67,81
Miller A. 48,51
Minialga V. 65
Mockevičienė S. 61,76
Nilsson M. 23
Nilsson P. 42
Norgėla Z. 59
Norkus D. 51
Plaipaitė R. 76
Plukienė R. 56
Plukis A. 56
Popov S. 48,51
Poškus A. 59
Prosyčevas I. 39
Puišo J. 39
Purlys R. 59
Raila.S. 81
Rinkūnas R. 59
Rotomskis R. 5,8,16
Rudik D. 35
Smirnova N. 35
Šetikienė G.76
Siaurys J.88
Šileikaitė A. 39
Simutytė I. 51
Skripkaitė E. 76
Šniurevičiūtė M. 81
Streckytė G. 16
Sukackaitė A. 8,12
Svensson J. 19
Tamulevičius S. 39
Tuchin V. 35
Tuchina E. 35
Urbanienė A. 59,76
Vaitiekonis Š. 56
Valančiūnaitė J. 16
Venius J. 5
Vladimirov A. 69
Warda M. 23
Weibull A. 19
Wilczynska T. 95
Wiśniewski R. 95
Zakarevičius E. 8
Žalgevičienė V. 8,12
Žerebcova J. 16
Žiliukas J. 59,72
Žukienė J. 12
Žurauskas E. 8

Information for Authors

Manuscripts on general and special questions pertaining to medical physics will be published in **Medical physics in the Baltic States**. Major areas of interest are as follows:

- radiotherapy physics;
- X-ray diagnostics and imaging;
- nuclear medicine;
- radiation protection;
- dosimetry;
- applications of ionizing and non ionizing radiation in medicine;
- general radiation physics and education.

The journal also includes book reviews, information on upcoming and past events, and discussions of topics on application of radiation physics in health care man-made and natural problems of the environment.

The manuscripts are printed in English with Lithuanian abstracts.

The Editorial Board gives preference to manuscripts of high scientific level, that have not been published, and are written clearly not only for specialists but also for the general public interested in the questions of medical physics.

Recommendations from competent authorities stating that the article deals with relevant medical physics questions, meets scientific requirements and is recommended to be published in the journal must be submitted by the authors to the Editorial Board. All manuscripts will be refereed by anonymous reviewers. The submitted manuscripts must be corrected according the reviewers remarks or contain an explanation why the remarks were ignored.

Original manuscripts should be submitted in two copies printed on one side of white A4 paper. The corrected manuscript must be sent to the Editorial Board by e-mail medphys@ktu.lt. The length of the manuscripts is not strictly limited, but the suggested length is 6-8 pages.

The article should be prepared using Microsoft Word 97 or Word 2000. The type for the text should be Times New Roman and in Baltic Rim code for the Lithuanian abstract. All the paper names must be written in the original language (e.g. Šušvė, Šiauliai). The main text (expect the abstract) is prepared one column in single spacing.

The margins of the manuscript should be: on the left and right 25 mm, top and bottom – 20 mm. The title of the article must be of 16 pt (Bold), names of the authors – 14 pt (Bold), name of the institution – 10 pt (Italic), names of the paragraphs – 10 pt (Bold), key words 10 pt (Italic), the main text and abstract – 10 pt, the names of tables and figures – 9 pt (Italic), comments and references – 9 pt, equations and their numbering – 10 pt, superscripts and subscripts – 8 pt.

The article should be organized in the following manner:

- title,
- names of the authors,
- name of the institution,
- abstract,
- key words (up to five),

- preface,
- the main article text (it is recommended to subdivide the main text into smaller sections),
- conclusions,
- acknowledgements,
- references.

The manuscript should be supplemented with the information about the authors: name, position, main research areas, address, and the telephone and fax numbers.

Authors are requested to ensure that abstracts give concise factual information about the objectives of the work, the methods used, the results obtained and the conclusions reached. A recommended length for the abstracts is 12 – 15 lines.

References should be listed at the end of the paper following the order of citation. Reference numbers should be given in the main text in square brackets. The list of references must be in English, e.g. 1. R. Jasiulionis. Registration of aerosol-borne radionuclides from distant sources in the air in the Ignalina NPP vicinity and their radiation doses. – Health Sciences (2003), 3(26) p.p. 5-10 (in Lithuanian).